Title

Microwave Assisted Colloidal Synthesis of Ge-based Nanomaterials

Author

Qi, Xiao

Publication Date

2022

Microwave Assisted Colloidal Synthesis of Ge-based Nanomaterials

By

XIAO QI
DISSERTATION

Submitted in partial satisfaction of the requirements for the degree of

DOCTOR OF PHILOSOPHY

in

Chemistry

in the

OFFICE OF GRADUATE STUDIES

of the

UNIVERSITY OF CALIFORNIA

DAVIS

Approved:

Susan M. Kauzlarich, Chair

Frank Osterloh

Klaus van Benthem

Committee in Charge

2021

Microwave Assisted Colloidal Synthesis of Ge-based Nanomaterials

To my Mom, my Dad, my Wife and my Children, for their encouragement, love, and support.

Acknowledgements

I would like to thank Professor Susan M. Kauzlarich for the support and mentorship she has provided me throughout my PhD career. Under her meticulous guidance, I learned how to become a better chemist. She taught me how to think systematically, creatively, and scientifically. More importantly, her constant encouragement and tolerance for failure were vital in keeping me exploring new science, trying various new methods, and learning new things. I feel so lucky to have her as my graduate advisor.

I would like to thank Prof. Klaus van Benthem for not only teaching me the fundamental science of the TEM in my first year of PhD, but also willing to serve as my dissertation committee member and help me revise my research proposal to the Molecular Foundry which served as a key part of my PhD research. I thank Dr. Andrew Thron for training me on how to use the TEM and his valuable discussion and guidance to help me critically analyze my data and results. I would like to specially thank Dr. Karen Bustillo who was my primary staff scientist at the Molecular Foundry throughout the past five years for her help and support on my work at NCEM. I thank Dr. Rohan Dhall, Dr. Emory Chan, Dr Tracy Mattox and all other Molecular Foundry staff for providing me with the guidance I need to succeed in the PhD program.

I greatly appreciate my group members in UC Davis for the wonderful time we spent together during the past several years. I would like to thank Dr. Bradley M. Nolan for friendship and training in my first year. I would also like to thank Dr. Christopher Perez and Dr. Zheng Ju as my collaborators and co-authors. I will miss the time we spent together.

Last but not the least, I would like to thank my wife and parents for their love and support during these years. Without your wholehearted support, encouragement and inspiration, the completion of this thesis would not have been possible.

This work was supported by the National Science Foundation CHE-1710110, and UC Davis Materials Chemistry Research Support. Electron microscopy at the Molecular Foundry at Lawrence Berkeley National Lab was supported by the Office of Science, Office of Basic Energy Sciences, of the U.S. Department of Energy under Contract No. DE-AC02-05CH11231.

Abstract

Microwave Assisted Colloidal Synthesis of Ge-based Nanomaterials

The rapidly increasing interest in Ge-based nanostructures is motivated by important advantages of this material compared to other semiconductors commonly investigated in the broad field of nanotechnology. Ge nanoparticles are promising materials for many applications such as photovoltaics, transistors, light emitting devices, bioimaging, and energy storage devices.

Due to the strong covalent bonding nature, synthesis of high-quality Ge nanoparticles with uniform size, well-defined morphology, composition, and surface chemistry is a main scientific challenge in the colloidal chemistry community and finding a reliable, scalable, cost-effective, and environmentally friendly synthetic route is of key importance for their further applications. Besides technical interest, access to defined nanoscale structures and compositions is also essential for uncovering their intrinsic properties and expanding the chemistry of group 14 nanomaterials.

In this dissertation, both direct synthetic methods and post transformation approaches are explored for rational synthesis of germanium-based nanomaterials with great control of the size, shape, and composition. The detailed reaction mechanisms are revealed through a systematic study on the reaction conditions such as temperature, precursor concentrations, reaction time, etc. Amorphous solid Ge nanoparticles and hollow Ge nanoparticles are synthesized via galvanic replacement reaction with Ag NPs serving as a sacrificial template. Ag@Ge core-shell nanoparticles with controlled shell thickness are also successfully synthesized as an intermediate. Their structural, optical, and electrical properties have been investigated in detail by high-angle annular dark-field scanning transmission electron microscopy (HAADF-STEM) and transmission electron microscopy (TEM), and supported by UV-Vis, Powder X-ray Diffraction (XRD), Energy-dispersive X-ray spectroscopy (EDS), etc. In addition, we provide an in situ method to observe the phase transition process of amorphous nano-germanium through a combination of both joule heating and high-energy electron beams at atomic resolution. The dynamic process of thermally induced structural evolution of the Ag@Ge binary system is also studied by TEM in real-time. The insights developed here can be extended to other metal semiconductor systems of interest and are crucial to developing the materials necessary for rigorous mechanistic studies of the effect of ligands and precursors on reactivity and selectivity. The two different synthetic approaches represent a way for achieving nanoparticles with strong covalent bonds as well as complex morphology, which would in turn increase the reproducibility of colloidal synthesis and prepare for scale-up and future practical applications.

Table of Contents

Acknowledgements iii

Abstract v

Chapter 1 Introduction 1

1.1 Motivation for the Colloidal Synthesis of Germanium Nanoparticles 1

1.2 Colloidal Nanoparticle Synthesis: Conventional Heating vs. Microwave 3

1.3 An Unconventional Way to Synthesise Ge NPs – Galvanic Replacement Reaction 5

1.4 Dissertation Outline 11

1.5 References 12

Chapter 2 Synthesis and Characterization Techniques 21

2.1 Overview 21

2.2 Synthesis Technique 21

2.2.1 Schlenk Line 21

2.2.2 Microwave Synthesis 22

2.3 Characterization 26

2.3.1 UV-Vis Spectrophotometry 26

2.3.2 X-ray Diffraction (XRD) 28

2.3.3 Transmission Electron Microscopy (TEM) 29

2.4 References 38

Chapter 3 Ge Nanocages and Nanoparticles via Microwave-Assisted Galvanic Replacement for Energy Storage Applications 43

3.1 Abstract 43

3.2 Introduction 44

3.3 Results and Discussion 47

3.3.1 Synthesis of Ag NPs 47

3.3.2 Synthesis of Ge NPs 48

3.3.3 Role of TOP 49

3.3.4 Role of DDT 52

3.3.5 Ge/Ag Ratio Influence 55

3.3.6 Temperature Influence 64

3.4 Conclusions 67

3.5 Materials and Methods 69

3.5.1 Chemicals and Materials 69

3.5.2 Synthesis of Silver NPs 70

3.5.3 Controlled Synthesis of Ge NPs 71

3.5.4 Characterization 71

3.6 References 72

Chapter 4 Atomic-Scale *in situ* Observation of Electron Beam and Heat Induced Crystallization of Ge Nanoparticles and Transformation of Ag@Ge Core-Shell Nanocrystals 77

4.1 Abstract...77

4.2 Introduction 78

4.3 Results and Discussion 81

4.3.1 Synthesis of Amorphous Ge NPs and Ag@Ge Core-shell NPs...........81

4.3.2 Structural and Compositional Characterizations of Ag@Ge Core-shell Nanoparticles..83

4.3.3 In situ Observation of the Crystallization of Amorphous Solid Ge NPs 85

4.3.4 In situ Observation of the Crystallization of Amorphous Hollow Ge NPs 88

4.3.5 In Situ Observation of the Structural Transformation of Ag@Ge Core−Shell Nanocrystals 90

4.4 Conclusion 94

4.5 Materials and Methods 95

4.5.1 Chemicals and Materials. 95

4.5.2 Synthesis of Silver Nanoparticles. 96

4.5.3 Synthesis of Ge NPs 96

4.5.4 Synthesis of Ag@Ge Core-shell NPs...97

4.5.5 Characterization – In situ Heating Experiment 97

4.6 References 98

Chapter 5 Summary and Outlook 104

Chapter 1

Introduction

1.1 Motivation for the Colloidal Synthesis of Germanium Nanoparticles

Germanium (Ge) is a hard-brittle, grayish-white metalloid with an attractive metallic luster. In 1886, Clemens Winkler found the new element from argyrodite, and subsequently named it germanium in honor of his country, Germany. Germanium ranks near fiftieth in relative abundance of the elements in the Earth's crust and it mostly exists in a mineral form of various types at low concentration. As a result, the industrial applications of germanium were limited for years until the development of the germanium transistor in 1948.[1] Since then, germanium has been used for countless applications. The global end uses for germanium are fiber-optic systems, infrared optics, electronics and solar applications, polymerization catalysts, and other uses (such as phosphors, metallurgy, and chemotherapy).[2]

As a group IV semiconductor nanomaterial, Ge has attracted much attention in recent years because of its inherent properties: Bulk Ge has a small bandgap of 0.67 eV (300 K) and a large Bohr exciton radius (24 nm), which shows a strong quantum confinement effect at relatively large particle sizes and allows tuning of light absorption and emission over a broad range of wavelengths.[3-5] These unique properties of nanoscale Ge make it promising for many optoelectronic devices such as plasmonic,[6] photodetectors,[7-9] and solar cells.[10-13] On the other hand, due to its high theoretical lithium storage capacity, high lithium-ion diffusivity, and conductivity,[14-16] Ge becomes one of the most promising candidates for the next generation anode materials for lithium-ion battery (LIB) applications.[17-23]

Despite its great promise, there are still several scientific challenges that need to be addressed. One key issue is finding a reliable, scalable, cost-effective and environmentally friendly synthetic route for the production of high-quality Ge nanoparticles. Compare to other processing methods such as molecular beam epitaxy, plasma-enhanced chemical vapor deposition, colloidal routes hold great promise for the synthesis of nanomaterials due to the low cost and flexibility associated with other solution-based processing techniques such as spin-coating, spray-coating, inkjet and screen printing. Solid progress was being made over the last decade for developing colloidal synthetic methods for the preparation of Ge nanoparticles (NPs),[24] however, less success was reported on the size and morphology control of such colloidal Ge NPs. Compared to the ubiquitous II-VI, III-V, IV-VI semiconductor and noble metal nanocrystals, well-defined shapes are much more difficult to achieve for Ge synthesis due to its high crystallization temperatures that originates from strong covalent bonding.[25] Nevertheless, common strategies such as thermal decomposition or reduction of organogermane precursors usually lead to amorphous products that are often unstable relative to dissolution and oxidation.[26, 27] To overcome this, strong reducing agents (e.g., Na, $LiAlH_4$, n-BuLi) and harsh reaction conditions (e.g., high temperature, high pressure) are usually applied to increase the crystallinity.[28-30] However, these methods are less favorable in terms of the high-energy cost and the possible toxic byproducts. Therefore, there is a strong need for the development of a simple and mild approach for the synthesis of high-quality Ge NPs with tunable sizes and shapes which would further help the application of these materials.

1.2 Colloidal Nanoparticle Synthesis: Conventional Heating vs. Microwave

Stemming largely from colloidal chemistry and organometallic chemistry, the rapid growth of solution-based synthesis of NPs over the last two decades has had a major impact on modern nanoscience and technology. Size control has a pivotal importance in the NP synthesis, and a great deal of research effort has been focused to find reliable and productive protocols to prepare highly uniform NPs with precisely controlled sizes.[31] For semiconductor NPs, size control is necessary for bandgap tuning of quantum dots (QDs), wherein quantum confinement of the charge carriers leads to bandgap broadening.[32] Noble metal NPs with their sizes far smaller than the wavelength of visible light (from about 390 to 700 nm) show unique plasmonic resonance band in their absorption.[33] The uniform size of the nanocrystals enables them to assembly into organized patterns provide valuable routes to the design of functional materials and to a variety of applications.

Colloidal nanoparticle synthesis is typically performed in a round-bottom flask at elevated temperature. The conventional heating method usually involves the use of a heating mantle or oil bath to heat the walls of the reactor which acts as the intermediary to transfer thermal energy from the external heat source to the solvent, and ultimately to the reactants. Such a pathway typically leads to thermal gradients throughout the bulk media, which means the inner sample can take much longer to achieve the target temperature, and this is the primary issue in the scale-up production.

As an alternative, the microwave heating can heat target materials without heating the entire flask or oil bath, which leads to a rapid and uniform reaction. Difference in the temperature profile of conventional and microwave heating is shown in Figure 1.1.[34] Over the past two decades, microwave dielectric heating technology has been receiving increasing attention as a promising fast heating method for chemistry synthesis and rapidly developed to a well-established synthetic technique used in many academic and industrial laboratories.

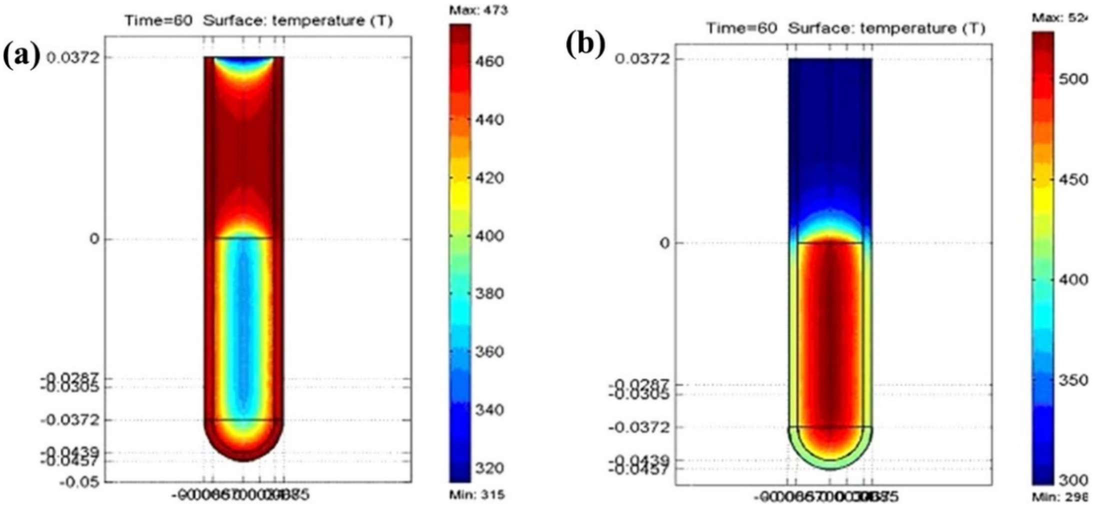

Figure 1.1. Difference in the temperature profile of (a) conventional and (b) microwave heating. The image shows a slice through a tube showing temperature gradients after 60 s of heating in (a) an oil-bath and (b) an CEM Discover microwave system.[34] In the oil heated tube (left), the reaction mixture in contact with the vessel wall is heated first whereas microwave irradiation raises the temperature of the whole reaction volume simultaneously (right). Temperature scale in Kelvin. Copyright 2003. Reprinted from ref (34) with permission.

Due to the difference in the solvent and reactant dielectric constants, microwave dielectric heating can provide significant enhancement in reaction rates. The rapid transfer of energy directly to the reactants causes an instantaneous internal temperature rise. By using metal precursors that have large microwave absorption cross-sections relative to the solvent, very high effective reaction temperatures can be achieved. This allows the rapid decomposition of the precursors thus creating highly supersaturated solutions where nucleation and growth can take place to produce the desired nanocrystalline products. In addition, the rapid heating and quenching ability of microwaves makes it possible to perform ultra-fast reactions (< 1 min) to synthesize very small nuclei at the early stage of the reaction and provides a detailed reaction mechanism which is not accessible by conventional heating methods. By varying the reaction time and the relative concentrations of ligands with variable binding strengths to the initial precursors and nuclei. Microwave heating have been demonstrated to successfully synthesize a variety of high-quality nanomaterials with controlled size, complicated shapes, and compositions in both aqueous solution[35-37] and organic solvents.[38-40]

With the constant improvement of the microwave reactor, coupled with modern technology such as wireless control, automatic sampler, built-in camera and sensors, the future microwave reactor has the potential to become a powerful, energy efficient and universal tool to replace the conventional wet chemistry synthesis.

1.3 An Unconventional Way to Synthesise Ge NPs – Galvanic Replacement Reaction

As discussed above, solution-based colloidal syntheses with microwave technology can offer several advantages relative to other methods. Ge, however, has proven challenging to synthesize in the solution phase, which has been largely attributed to its redox potential ($Ge^{2+} + 2e^{-} \rightarrow Ge^{0}$ $E^{0} = +0.245$ V, $Ge^{4+} + 4e^{-} \rightarrow Ge^{0}$ $E^{0} = +0.12$ V).[41] Such a redox potential makes the utilization of either high temperatures or strong reducing agents to form Ge^{0}.[29, 42-49] On the other hand, among the four tetrahalides known, only GeI_4 is a solid. GeF_4 is a gas, and the others ($GeCl_4$ and $GeBr_4$) are volatile liquids under normal conditions. The high temperature requirement for the colloidal synthesis of Ge NPs limits the choice of suitable precursors of Ge. Although much work has been done to explore a suitable condition for microwave-assisted Ge nanocrystal synthesis,[45, 50, 51] There is still a need for the improvement of synthetic protocol and better understanding of the surface of Ge nanocrystals in order to control strain, crystallinity and surface.[25, 52]

In addition to the conventional colloidal synthesis strategies, galvanic replacement reaction provides a simple and versatile route for reducing noble metal precursors and generating nanostructures with controllable pores and compositions. During the past two decades, many elegant and remarkable syntheses have been performed by different groups by cooperative galvanic replacement reactions and have produced a variety of nanoscale structures with complex morphologies.[53-57] However, recent research has mainly focused on the transformation of noble metals such as Au, Pd, and Pt. We recently demonstrated the unconventional transformation of inorganic germanium precursors (e.g., GeI_2) to hollow Ge NPs through galvanic replacement with Ag NPs.[58] In this reaction, Ge^{2+} oxidizes Ag to Ag^+, which causes the hollowing-out of the sacrificial Ag NP templates.

Galvanic replacement is a redox process depending on the direct contact of one metal (which is often referred to as a sacrificial template) with the ions of a second metal having a higher reduction potential in a solution phase. This process involves the initial oxidization of the sacrificial template, and the released electrons will quickly migrate to the outer surface and be captured by the ions of the second metal. As a result, the metal ions in the solution phase will get reduced and sequentially depositing on the same site. Since the newly formed atoms are deposited directly on the surface of the template, the final product typically possesses a shape closely resembling that of the original template with a slight increase in dimensions and leaves an internal void space in the final structure.[59] A galvanic replacement reaction can be broken down into two half reactions: the oxidation or corrosion of the first metal and the reduction of the ions of the second metal. The driving force for this reaction comes from the difference in reduction potentials of the two metals involved, with the potential of the second metal necessarily being higher than that of the first metal.

The overall reaction driving force can be calculated according to the Nernst equation:

Equation 1.1

$$E_{red} = E_{red}^{o} - \frac{RT}{zF} ln \frac{a_{red}}{a_{OX}}$$

Where E_{red} is the half-cell reduction potential at the temperature of interest, E^{o}_{red} is the standard half-cell reduction potential, R is the universal gas constant: $R = 8.314 \text{ J K}^{-1} \text{ mol}^{-1}$, T is the temperature in kelvins, F is the Faraday constant, $F = 9.6485\times10^{4} \text{ C mol}^{-1}$, z is the number of moles of electrons transferred in the cell reaction or half-reaction, a is the chemical activity for the relevant species, where a_{Red} is the activity of the reduced form and a_{Ox} is the activity of the oxidized form. (Because activity coefficients tend to unite at low concentrations, activities in the Nernst equation are frequently replaced by simple concentrations.)

Notice that the overall cell reduction potential will be roughly determined by the difference of the standard half-cell reduction potential, but the concentrations of relevant ions and the temperature can also change the net reduction potential. It should also be pointed out that the available reduction potential data are for aqueous solution only. The involvement of other non-standard conditions (e.g., non-aqueous solution) can all affect the actual value of reduction potential. These changes may reverse the direction of a replacement reaction and result in the termination or prevention of galvanic replacement. This increases the difficulty to calculate the accurate cell potential of the reaction, but it can still provide some general guidelines to help us optimize the reaction conditions.

In the synthesis of hollow Ge NPs, the galvanic replacement reaction occurs between Ag and GeI_2. By applying the standard reduction potentials at 298 K:

Left electrode: $2AgI(s) + 2e^- \rightarrow 2Ag(s) + 2I^-(aq)$ $E_-^0 = -0.152\ V$

Right electrode: $Ge^{2+} + 2e^- \rightarrow Ge(s)$ $E_+^0 = 0.245\ V$

$$E_{Cell}^0 = E_+^0 - E_-^0 = 0.245\ \text{V} - (-0.152\ \text{V}) = 0.397\ \text{V}$$

The positive cell voltage indicates that the net reaction is spontaneous for the reduction of Ge^{2+}. The Ge precursor was carefully chosen, as GeI_2 will effectively introduce the I^- ions to facilitate the reaction. In this case, the reduction potential of Ag was greatly reduced from +0.8 (for Ag^+/Ag) to −0.15 V (for AgI/Ag), thereby creating a significant difference in reduction potential between the Ag template and GeI_2, which makes this reaction possible.

Despite the continuously improving understanding of the mechanism of galvanic replacement during the last two decades,[60-62] most of the research work was based on the transformation of noble metals such as Au, Pd, and Pt. For example, the reaction mechanism between single crystal silver nanocubes and chloroauric acid in both aqueous medium and organic solvent have been studied by many groups.[59, 61, 63-66] The major steps include (1) initiation of replacement reaction at a specific site with the highest surface energy; when an aqueous $HAuCl_4$ solution is added into an aqueous suspension of Ag nanoparticles, galvanic replacement will be initiated immediately at the site with the highest surface energy (e.g., defect, stacking fault);[67] (2) continuation of the replacement reaction between Ag and $HAuCl_4$ and the formation of a partially hollow nanostructure; (3) formation of nanoboxes with a uniform, smooth, homogeneous wall composed of Au/Ag alloy; (4) initiation of dealloying and corner reconstruction of the Au/Ag nanoboxes; and (5,6) continuation of dealloying and formation of an Au nanocage–nanoboxes with pores in the walls. A photograph of galvanic replacement reaction between $AgNO_3$ solution and Cu wire and a scheme of the mechanism discussed above is shown in Figure 1.2.[59] However, the formation mechanism of semiconductor materials via galvanic replacement has remained largely unknown. This is mainly due to the limited number of successful syntheses of such semiconductor nanostructures through galvanic replacement reaction. Our research represents an example to study the mechanism of galvanic replacement reaction in a non-aqueous solution. The reaction between GeI_2 and Ag NPs were conducted in a water and oxygen-free environment and the relatively high reaction temperature enable an immediate quench of the reaction thus a variety of intermediates can be separated and characterized. Our results suggest a different reaction mechanism compared to the aqueous solution-based reactions and provide valuable information regarding to the morphological and compositional transformation during the galvanic replacement reactions.

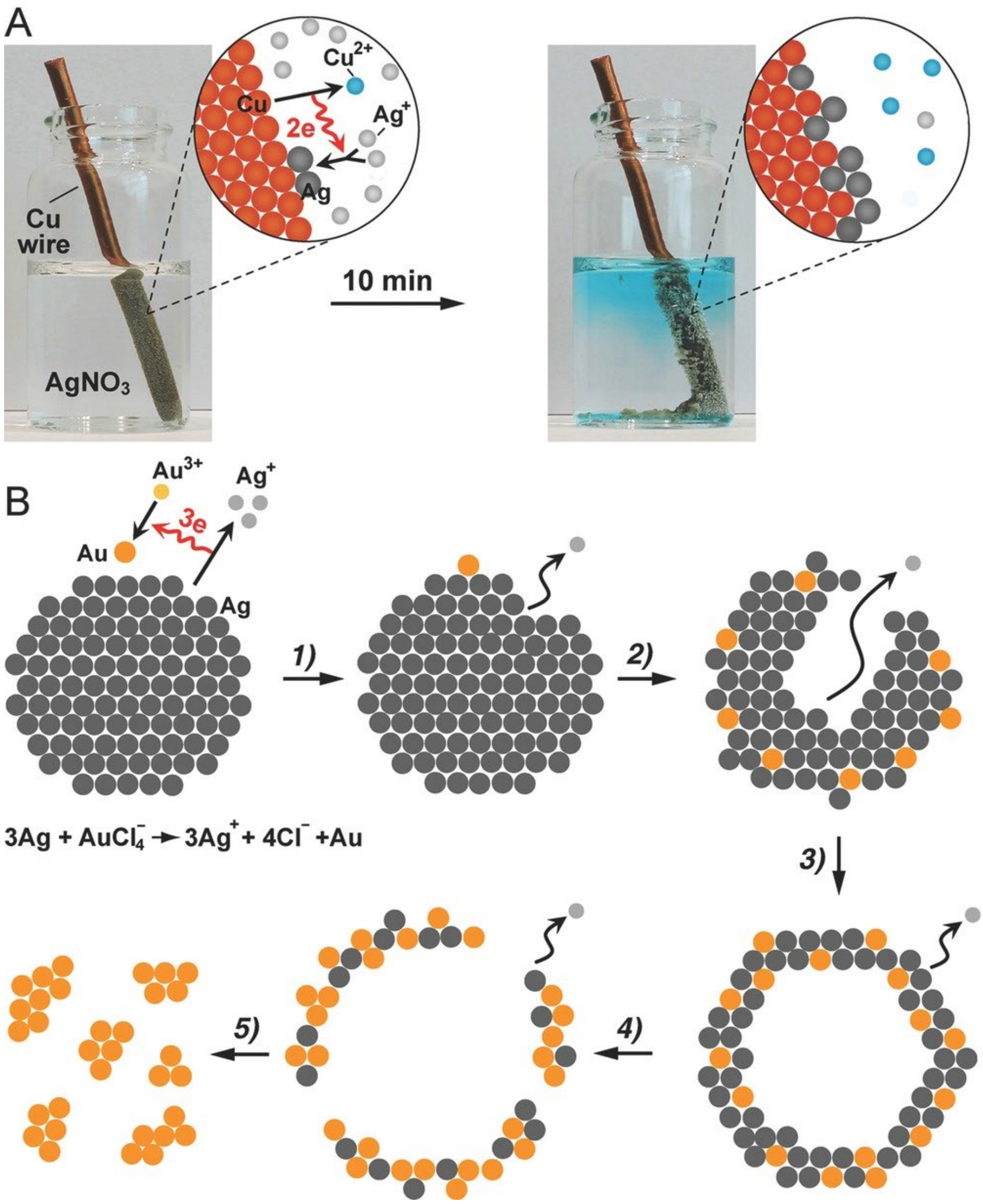

Figure 1.2. (A) Photographs of a glass vial containing $AgNO_3$ solution (left) immediately after the insertion of a Cu wire and (right) after the galvanic replacement reaction had proceeded for 10 min. The insets show atomic models used to illustrate the mechanism involved in the galvanic replacement reaction between Cu and $AgNO_3$. (B) Schematic illustration of the morphological and structural changes at different stages of the galvanic replacement reaction between a Ag nanoparticle and $HAuCl_4$ in an aqueous solution.[56] Reprinted from ref (56) with permission.

1.4 Dissertation Outline

In Chapter 3, we reveal the specific roles of each reagent in the galvanic replacement between GeI_2 and Ag nanoparticles through a comprehensive study. This significantly refined understanding allows us to develop an efficient and highly reproducible process for producing hollow Ge NPs with high yield and desirable quality (e.g., narrow size distribution, well-defined morphology, etc.). Specifically, we find tri-n-octylphosphine (TOP) which previously thought as only a transferring agent of Ag^+ were also serving as a stabilizing agent of the GeI_2 through a Ge-TOP complex and thus control the deposition rate of Ge atoms. In addition, dodecanethiol (DDT), which served as the binding ligand, was found to be critical to the geometry evolution of the hollow Ge NPs. With a higher concentration of DDT, more vacancies will be generated on the surface of the particles, leading to the formation of hollow Ge nanocages. The molar ratio between silver NPs and Ge precursors dominate the diffusion rate and thus determine the final shape of the products. By varying the molar ratio, monodisperse hollow Ge NPs and solid Ge NPs could form with high yield.

In Chapter 4, the influence of temperature and reaction time on the galvanic replacement reaction was further explored. By controlling the temperature and the reaction time, a well-defined Ag@Ge core-shell structure can be isolated with a controllable thickness of the germanium shell. This finding is also very interesting due to the large lattice parameter mismatch (38.7%) between Ag and Ge. A real-time observation of the dynamic process of thermally induced structural evolution of the Ag/Ge binary system was also present. By combining real-time structural imaging with elemental analysis, we can follow the transformation process which occurs through crystallization of the amorphous Ge shell and is accompanied by surface segregation of Ag. All these findings will help us to identify the appropriate synthetic parameters and understand their interaction and contributions to the structure evolution.

1.5 References

1. Bardeen, J.; Brattain, W. H., The Transistor, A Semi-Conductor Triode. *Physical Review* **1948,** *74* (2), 230-231.

2. Germanium – Events, Trends, and Issues. 2018.

3. Barbagiovanni, E. G.; Lockwood, D. J.; Simpson, P. J.; Goncharova, L. V., Quantum confinement in Si and Ge nanostructures: Theory and experiment. *Applied Physics Reviews* **2014,** *1* (1), 011302.

4. Li, C.; Wang, F.; Yu, J. C., Semiconductor/biomolecular composites for solar energy applications. *Energy & Environmental Science* **2011,** *4* (1), 100-113.

5. Hoffman, M.; Veinot, J. G. C., Understanding the Formation of Elemental Germanium by Thermolysis of Sol-Gel Derived Organogermanium Oxide Polymers. *Chemistry of Materials* **2012,** *24* (7), 1283-1291.

6. Baldassarre, L.; Sakat, E.; Frigerio, J.; Samarelli, A.; Gallacher, K.; Calandrini, E.; Isella, G.; Paul, D. J.; Ortolani, M.; Biagioni, P., Midinfrared Plasmon-Enhanced Spectroscopy with Germanium Antennas on Silicon Substrates. *Nano Letters* **2015,** *15* (11), 7225-7231.

7. Tang, L.; Kocabas, S. E.; Latif, S.; Okyay, A. K.; Ly-Gagnon, D.-S.; Saraswat, K.

C.; Miller, D. A. B., Nanometre-scale germanium photodetector enhanced by a near-infrared dipole antenna. *Nature Photonics* **2008,** *2* (4), 226-229.

8. Assefa, S.; Xia, F.; Vlasov, Y. A., Reinventing germanium avalanche photodetector for nanophotonic on-chip optical interconnects. *Nature* **2010,** *464* (7285), 80-84.

9. Michel, J.; Liu, J.; Kimerling, L. C., High-performance Ge-on-Si photodetectors. *Nature Photonics* **2010,** *4* (8), 527-534.

10. King, R. R.; Law, D. C.; Edmondson, K. M.; Fetzer, C. M.; Kinsey, G. S.; Yoon, H.; Sherif, R. A.; Karam, N. H., 40% efficient metamorphic GaInP⁄GaInAs⁄Ge multijunction solar cells. *Applied Physics Letters* **2007,** *90* (18), 183516.

11. Guter, W.; Schöne, J.; Philipps, S. P.; Steiner, M.; Siefer, G.; Wekkeli, A.; Welser, E.; Oliva, E.; Bett, A. W.; Dimroth, F., Current-matched triple-junction solar cell reaching 41.1% conversion efficiency under concentrated sunlight. *Applied Physics Letters* **2009,** *94* (22), 223504.

12. Cánovas, E.; Fuertes Marrón, D.; Martí, A.; Luque, A.; Bett, A. W.; Dimroth, F.; Philipps, S. P., Photoreflectance analysis of a GaInP/GaInAs/Ge multijunction solar cell. *Applied Physics Letters* **2010,** *97* (20), 203504.

13. Beard, M. C.; Luther, J. M.; Nozik, A. J., The promise and challenge of nanostructured solar cells. *Nature Nanotechnology* **2014,** *9* (12), 951-954.

14. Choi, S.; Kim, J.; Choi, N.-S.; Kim, M. G.; Park, S., Cost-Effective Scalable Synthesis of Mesoporous Germanium Particles via a Redox-Transmetalation Reaction for High-Performance Energy Storage Devices. *ACS Nano* **2015,** *9* (2), 2203-2212.

15. Park, M.-H.; Cho, Y.; Kim, K.; Kim, J.; Liu, M.; Cho, J., Germanium Nanotubes

Prepared by Using the Kirkendall Effect as Anodes for High-Rate Lithium Batteries. *Angewandte Chemie International Edition* **2011,** *50* (41), 9647-9650.

16. Li, W.; Li, M.; Yang, Z.; Xu, J.; Zhong, X.; Wang, J.; Zeng, L.; Liu, X.; Jiang, Y.; Wei, X.; Gu, L.; Yu, Y., Carbon-Coated Germanium Nanowires on Carbon Nanofibers as Self-Supported Electrodes for Flexible Lithium-Ion Batteries. *Small* **2015,** *11* (23), 2762-2767.

17. Li, D.; Wang, H.; Liu, H. K.; Guo, Z., A New Strategy for Achieving a High Performance Anode for Lithium Ion Batteries—Encapsulating Germanium Nanoparticles in Carbon Nanoboxes. *Advanced Energy Materials* **2016,** *6* (5), 1501666.

18. Yuan, F.-W.; Yang, H.-J.; Tuan, H.-Y., Alkanethiol-Passivated Ge Nanowires as High-Performance Anode Materials for Lithium-Ion Batteries: The Role of Chemical Surface Functionalization. *ACS Nano* **2012,** *6* (11), 9932-9942.

19. Stokes, K.; Geaney, H.; Flynn, G.; Sheehan, M.; Kennedy, T.; Ryan, K. M., Direct Synthesis of Alloyed Si1–xGex Nanowires for Performance-Tunable Lithium Ion Battery Anodes. *ACS Nano* **2017,** *11* (10), 10088-10096.

20. Park, M.-H.; Kim, K.; Kim, J.; Cho, J., Flexible Dimensional Control of High-Capacity Li-Ion-Battery Anodes: From 0D Hollow to 3D Porous Germanium Nanoparticle Assemblies. *Advanced Materials* **2010,** *22* (3), 415-418.

21. Liu, J.; Song, K.; Zhu, C.; Chen, C.-C.; van Aken, P. A.; Maier, J.; Yu, Y., Ge/C Nanowires as High-Capacity and Long-Life Anode Materials for Li-Ion Batteries. *ACS Nano* **2014,** *8* (7), 7051-7059.

22. Wu, S.; Han, C.; Iocozzia, J.; Lu, M.; Ge, R.; Xu, R.; Lin, Z., Germanium-Based

Nanomaterials for Rechargeable Batteries. *Angewandte Chemie International Edition* **2016,** *55* (28), 7898-7922.

23. Li, D.; Wang, H.; Zhou, T.; Zhang, W.; Liu, H. K.; Guo, Z., Unique Structural Design and Strategies for Germanium-Based Anode Materials Toward Enhanced Lithium Storage. *Advanced Energy Materials* **2017,** *7* (23), 1700488.

24. Vaughn Ii, D. D.; Schaak, R. E., Synthesis, properties and applications of colloidal germanium and germanium-based nanomaterials. *Chemical Society Reviews* **2013,** *42* (7), 2861-2879.

25. Lee, D. C.; Pietryga, J. M.; Robel, I.; Werder, D. J.; Schaller, R. D.; Klimov, V. I., Colloidal Synthesis of Infrared-Emitting Germanium Nanocrystals. *Journal of the American Chemical Society* **2009,** *131* (10), 3436-3437.

26. He, R.; Sazio, P. J. A.; Peacock, A. C.; Healy, N.; Sparks, J. R.; Krishnamurthi, M.; Gopalan, V.; Badding, J. V., Integration of gigahertz-bandwidth semiconductor devices inside microstructured optical fibres. *Nature Photonics* **2012,** *6* (3), 174-179.

27. Gärtner, K.; Jöhrens, J.; Steinbach, T.; Schnohr, C. S.; Ridgway, M. C.; Wesch, W., Void formation in amorphous germanium due to high electronic energy deposition. *Physical Review B* **2011,** *83* (22), 224106.

28. Chou, N. H.; Oyler, K. D.; Motl, N. E.; Schaak, R. E., Colloidal Synthesis of Germanium Nanocrystals Using Room-Temperature Benchtop Chemistry. *Chemistry of Materials* **2009,** *21* (18), 4105-4107.

29. Lu, X.; Korgel, B. A.; Johnston, K. P., High Yield of Germanium Nanocrystals Synthesized from Germanium Diiodide in Solution. *Chemistry of Materials* **2005,** *17* (25),

6479-6485.

30. Zaitseva, N.; Dai, Z. R.; Grant, C. D.; Harper, J.; Saw, C., Germanium Nanocrystals Synthesized in High-Boiling-Point Organic Solvents. *Chemistry of Materials* **2007,** *19* (21), 5174-5178.

31. Kwon, S. G.; Hyeon, T., Formation Mechanisms of Uniform Nanocrystals via Hot-Injection and Heat-Up Methods. *Small* **2011,** *7* (19), 2685-2702.

32. Bawendi, M. G.; Steigerwald, M. L.; Brus, L. E., The Quantum Mechanics of Larger Semiconductor Clusters ("Quantum Dots"). *Annual Review of Physical Chemistry* **1990,** *41* (1), 477-496.

33. Mulvaney, P., Surface Plasmon Spectroscopy of Nanosized Metal Particles. *Langmuir* **1996,** *12* (3), 788-800.

34. Schanche, J.-S., Microwave synthesis solutions from personal chemistry. *Molecular Diversity* **2003,** *7* (2), 291-298.

35. Vargas-Hernandez, C.; Mariscal, M. M.; Esparza, R.; Yacaman, M. J., A synthesis route of gold nanoparticles without using a reducing agent. *Applied Physics Letters* **2010,** *96* (21), 213115.

36. Kou, J.; Varma, R. S., Beet juice utilization: Expeditious green synthesis of noble metal nanoparticles (Ag, Au, Pt, and Pd) using microwaves. *RSC Advances* **2012,** *2* (27), 10283-10290.

37. He, Y.; Zhong, Y.; Peng, F.; Wei, X.; Su, Y.; Lu, Y.; Su, S.; Gu, W.; Liao, L.; Lee, S.-T., One-Pot Microwave Synthesis of Water-Dispersible, Ultraphoto- and pH-Stable, and Highly Fluorescent Silicon Quantum Dots. *Journal of the American Chemical Society* **2011,**

133 (36), 14192-14195.

38. Mohamed, M. B.; AbouZeid, K. M.; Abdelsayed, V.; Aljarash, A. A.; El-Shall, M. S., Growth Mechanism of Anisotropic Gold Nanocrystals via Microwave Synthesis: Formation of Dioleamide by Gold Nanocatalysis. *ACS Nano* **2010,** *4* (5), 2766-2772.

39. Gao, F.; Lu, Q.; Komarneni, S., Interface Reaction for the Self-Assembly of Silver Nanocrystals under Microwave-Assisted Solvothermal Conditions. *Chemistry of Materials* **2005,** *17* (4), 856-860.

40. Ziegler, J.; Merkulov, A.; Grabolle, M.; Resch-Genger, U.; Nann, T., High-Quality ZnS Shells for CdSe Nanoparticles: Rapid Microwave Synthesis. *Langmuir* **2007,** *23* (14), 7751-7759.

41. *CRC Handbook of Chemistry and Physics: A Ready-Reference Book of Chemical and Physical Data*. Special Student Edition 72nd ed ed.; CRC Press: 1993.

42. Prabakar, S.; Shiohara, A.; Hanada, S.; Fujioka, K.; Yamamoto, K.; Tilley, R. D., Size Controlled Synthesis of Germanium Nanocrystals by Hydride Reducing Agents and Their Biological Applications. *Chemistry of Materials* **2010,** *22* (2), 482-486.

43. Ge, S.; Jiang, K.; Lu, X.; Chen, Y.; Wang, R.; Fan, S., Orientation-Controlled Growth of Single-Crystal Silicon-Nanowire Arrays. *Advanced Materials* **2005,** *17* (1), 56-61.

44. Heath, J. R.; Shiang, J. J.; Alivisatos, A. P., Germanium quantum dots: Optical properties and synthesis. *The Journal of Chemical Physics* **1994,** *101* (2), 1607-1615.

45. Bernard, A.; Zhang, K.; Larson, D.; Tabatabaei, K.; Kauzlarich, S. M., Solvent Effects on Growth, Crystallinity, and Surface Bonding of Ge Nanoparticles. *Inorganic Chemistry* **2018,** *57* (9), 5299-5306.

46. Gerion, D.; Zaitseva, N.; Saw, C.; Casula, M. F.; Fakra, S.; Van Buuren, T.; Galli, G., Solution Synthesis of Germanium Nanocrystals: Success and Open Challenges. *Nano Letters* **2004,** *4* (4), 597-602.

47. Lu, X.; Ziegler, K. J.; Ghezelbash, A.; Johnston, K. P.; Korgel, B. A., Synthesis of Germanium Nanocrystals in High Temperature Supercritical Fluid Solvents. *Nano Letters* **2004,** *4* (5), 969-974.

48. Myung, N.; Lu, X.; Johnston, K. P.; Bard, A. J., Electrogenerated Chemiluminescence of Ge Nanocrystals. *Nano Letters* **2004,** *4* (1), 183-185.

49. Gerung, H.; Bunge, S. D.; Boyle, T. J.; Brinker, C. J.; Han, S. M., Anhydrous solution synthesis of germanium nanocrystals from the germanium(ii) precursor Ge[N(SiMe3)2]2. *Chemical Communications* **2005,** (14), 1914-1916.

50. Newton, K. A.; Ju, Z.; Tabatabaei, K.; Kauzlarich, S. M., Diorganyl Dichalcogenides as Surface Capping Ligands for Germanium Nanocrystals. *Organometallics* **2020,** *39* (7), 995-1005.

51. Tabatabaei, K.; Holmes, A. L.; Newton, K. A.; Muthuswamy, E.; Sfadia, R.; Carter, S. A.; Kauzlarich, S. M., Halogen-Induced Crystallinity and Size Tuning of Microwave Synthesized Germanium Nanocrystals. *Chemistry of Materials* **2019,** *31* (18), 7510-7521.

52. Vaughn, D. D.; Bondi, J. F.; Schaak, R. E., Colloidal Synthesis of Air-Stable Crystalline Germanium Nanoparticles with Tunable Sizes and Shapes. *Chemistry of Materials* **2010,** *22* (22), 6103-6108.

53. Sayed, S. Y.; Buriak, J. M., Epitaxial Growth of Nanostructured Gold Films on Germanium via Galvanic Displacement. *ACS Applied Materials & Interfaces* **2010,** *2* (12), 3515-3524.

54. Oh Myoung, H.; Yu, T.; Yu, S.-H.; Lim, B.; Ko, K.-T.; Willinger, M.-G.; Seo, D.-H.; Kim Byung, H.; Cho Min, G.; Park, J.-H.; Kang, K.; Sung, Y.-E.; Pinna, N.; Hyeon, T., Galvanic Replacement Reactions in Metal Oxide Nanocrystals. *Science* **2013,** *340* (6135), 964-968.

55. El Mel, A.-A.; Chettab, M.; Gautron, E.; Chauvin, A.; Humbert, B.; Mevellec, J.-Y.; Delacote, C.; Thiry, D.; Stephant, N.; Ding, J.; Du, K.; Choi, C.-H.; Tessier, P.-Y., Galvanic Replacement Reaction: A Route to Highly Ordered Bimetallic Nanotubes. *The Journal of Physical Chemistry C* **2016,** *120* (31), 17652-17659.

56. Xia, X.; Wang, Y.; Ruditskiy, A.; Xia, Y., 25th Anniversary Article: Galvanic Replacement: A Simple and Versatile Route to Hollow Nanostructures with Tunable and Well-Controlled Properties. *Advanced Materials* **2013,** *25* (44), 6313-6333.

57. González, E.; Arbiol, J.; Puntes Víctor, F., Carving at the Nanoscale: Sequential Galvanic Exchange and Kirkendall Growth at Room Temperature. *Science* **2011,** *334* (6061), 1377-1380.

58. Nolan, B. M.; Chan, E. K.; Zhang, X.; Muthuswamy, E.; van Benthem, K.; Kauzlarich, S. M., Sacrificial Silver Nanoparticles: Reducing GeI2 To Form Hollow Germanium Nanoparticles by Electroless Deposition. *ACS Nano* **2016,** *10* (5), 5391-5397.

59. Sun, Y.; Xia, Y., Shape-Controlled Synthesis of Gold and Silver Nanoparticles. *Science* **2002,** *298* (5601), 2176-2179.

60. Chen, A. N.; McClain, S. M.; House, S. D.; Yang, J. C.; Skrabalak, S. E., Mechanistic Study of Galvanic Replacement of Chemically Heterogeneous Templates. *Chemistry of Materials* **2019,** *31* (4), 1344-1351.

61. Sun, Y.; Xia, Y., Mechanistic Study on the Replacement Reaction between Silver

Nanostructures and Chloroauric Acid in Aqueous Medium. *Journal of the American Chemical Society* **2004,** *126* (12), 3892-3901.

62. Sun, X.; Yang, Y.; Zhang, Z.; Qin, D., Mechanistic Roles of Hydroxide in Controlling the Deposition of Gold on Colloidal Silver Nanocrystals. *Chemistry of Materials* **2017,** *29* (9), 4014-4021.

63. Lin, Z.-W.; Tsao, Y.-C.; Yang, M.-Y.; Huang, M. H., Seed-Mediated Growth of Silver Nanocubes in Aqueous Solution with Tunable Size and Their Conversion to Au Nanocages with Efficient Photothermal Property. *Chemistry – A European Journal* **2016,** *22* (7), 2326-2332.

64. Wu, Y.; Sun, X.; Yang, Y.; Li, J.; Zhang, Y.; Qin, D., Enriching Silver Nanocrystals with a Second Noble Metal. *Accounts of Chemical Research* **2017,** *50* (7), 1774-1784.

65. Yang, J.; Lee, J. Y.; Ying, J. Y., Phase transfer and its applications in nanotechnology. *Chemical Society Reviews* **2011,** *40* (3), 1672-1696.

66. Yang, J.; Lee, J. Y.; Too, H.-P., Core−Shell Ag−Au Nanoparticles from Replacement Reaction in Organic Medium. *The Journal of Physical Chemistry B* **2005,** *109* (41), 19208-19212.

67. Hong, X.; Wang, D.; Cai, S.; Rong, H.; Li, Y., Single-Crystalline Octahedral Au–Ag Nanoframes. *Journal of the American Chemical Society* **2012,** *134* (44), 18165-18168.

Chapter 2

Synthesis and Characterization Techniques

2.1 Overview

Experimental design for nanoparticle synthesis is presented in this chapter. Variety of material characterization techniques are also discussed. To characterize the samples, UV-Vis is used to analyze the optical absorption properties and TEM, XRD, and EDS are used to analyze the morphology, structure, and chemical composition of the nanoparticles.

2.2 Synthesis Technique

2.2.1 Schlenk Line

Wet chemical synthesis is usually performed on a vacuum/inert gas manifold system, commonly called Schlenk line, which is an essential equipment for handling air and moisture sensitive materials and allow for the performance of reactions under the protection of inert atmosphere (typically argon or nitrogen) without the use of a glovebox. A Schlenk line consists of a dual manifold with several ports. The manifold is connected to a vacuum pump and an inert gas source. The inert gas is purified by passing through several columns of desiccants including molecular sieves and calcium sulfate to remove water content and a column containing a heated Cu catalyst for deoxygenation before connected to the inert-gas line and vented through an oil bubbler. The oil bubbler helps to monitor the overall gas flow rate and prevent any pressure build-up in the system. A liquid-nitrogen or dry-ice/acetone cold trap needs to be set between the vacuum manifold and the pump to prevent solvent vapors and gaseous reaction products entering the pump and degrading the pump oil.

Nanoparticle syntheses are most performed on a Schlenk line when air-free environments are required. Pre-dissolved reaction precursors and solvents are loaded into a three-neck round-bottom flask and degassed under vacuum at an elevated temperature to remove water and oxygen and refluxed with inert gas several times before starting the reaction. For more air-sensitive materials, the chemicals can be loaded inside a glovebox and sealed using glass stoppers and/or rubber septa before connected to the Schlenk line. Reactions were heated using either an oil bath or a heating mantle controlled by a PID temperature controller and thermocouple.

2.2.2 Microwave

The microwave technology is emerging as a powerful alternative heating method for chemical reactions and materials synthesis. Over the past two decades, microwave chemistry has rapidly developed into a well-established synthetic technique used in many academic and industrial laboratories. The microwave-assisted colloidal synthesis of inorganic nanostructured materials is currently a fast-growing area of research.

Microwaves are broadly regarded as electromagnetic waves which are situated between infrared and radio wavelengths in the electromagnetic spectrum, with wavelengths between

0.01 and 1 m, corresponding to frequencies between 0.3 and 300 GHz. In 1945, the heating effect of a high-power microwave beam was accidentally discovered by Percy Spencer for the first time.[1] But it was not until 1971 that the use of microwave heating in chemical research was first reported.[2] Since then, microwave heating has become a widely accepted non-conventional energy source for performing solution-phase chemical synthesis.[3-5] Use of radiation within the microwave region is regulated at national and international levels to avoid interference with telecommunications. While large industrial/commercial microwave ovens use 915 MHz, almost all domestic microwave ovens and laboratory-scale synthesis systems operate at the frequency of 2.45 GHz.

Microwave irradiation induces heating by two main mechanisms— dipolar polarization for polar molecules (e.g., polar solvent, reagents) and ionic conduction for charged particles (e.g., cations and anions). When irradiated at microwave frequencies, polar molecules such as water molecules try to align in the applied electric field and heat is produced through collision, rotation, and friction of the molecules.[6] In the case of ions, any ions present in solution will move constantly in align with the fluctuation of the applied electric field, causing a local temperature to rise due to friction and collision. For semiconducting and conducting samples, heat is generated by the ions or electrons within them form an electric current and energy is lost due to the electrical resistance of the material.[7]

The ability of a specific material or solvent to convert microwave energy into heat at a given frequency and temperature is quantified by the so-called loss tangent.[8] The electric loss tangent can be expressed as the quotient $\tan \delta e = \varepsilon''/\varepsilon'$, where ε'' is the dielectric loss, which quantifies a dielectric material's inherent dissipation of electromagnetic energy (e.g. heat)., and ε' is the dielectric constant describing the polarizability of molecules in the electric field.[8-10] In general, a reaction medium with a high loss tangent is required for good absorption and efficient heating while solvents without a permanent dipole moment are microwave transparent. The loss tangent value at room temperature for common solvents used in microwave chemistry is listed in Table 2.1.[8-11]

Table 2.1 Loss Tangents (tan δ) of Selected Solvents and Materials (2.45 GHz, 20 °C) Reprinted from ref (11) with permission.

Solvent	**Loss Tangent (tan *δ*)**	**Solvent / Materials**	**Loss Tangent (tan *δ*)**
Ethylene glycol	1.35	Chloroform	0.091
Ethanol	0.941	Acetonitrile	0.062
DMSO	0.825	Tetrahydrofuran	0.047
Methanol	0.659	Toluene	0.04
1,2-Dichlorobenzene	0.28	Hexane	0.02
Acetic acid	0.174		
DMF	0.161	Borosilicate glass	10×10^{-4}
1,2-Dichloroethane	0.127	Teflon	1.5×10^{-4}
Water	0.123	Quartz	0.6×10^{-4}

It is important to note that the dielectric properties can vary significantly as a function of the temperature, and this is since most solvents are heated primarily via the dipolar polarization mechanism. At higher temperature, the bulk viscosity of the solvents decreases which leads to a reduced molecular friction thus the heat induced under microwave irradiation also decreased.[11] In contrast, ionic liquids are heated by an ionic conduction mechanism which its loss tangent could dramatically increase at higher temperature. For example, the loss tangent of 1-butyl-3-methylimidazolium hexafluorophosphate increases near 20-folds as temperature increased from 20 °C to 200 °C.[12]

Compared to conventional heating methods, in which the reaction vessel wall is heated first, the microwave energy has a negligible effect on the reaction vessels which are usually made by materials with very small loss tangent such as borosilicate glass, Teflon, or quartz (Table 2.1). The microwave radiation directly couples with the molecules in the reaction mixture and raises the temperature of the whole reaction volume simultaneously, results in a more uniform temperature distribution in the reaction mixture and thus have a completely different temperature profile than conventional heating methods.[11]

In general, the organic solvents used for nanoparticle synthesis are non-polar (e.g., oleylamine, dioctyl ether) and thus are not good microwave absorbers. For that reason, the two microwave absorbing mechanisms described above must be carefully balanced to achieve the best results. The volume of the solvents and the concentration of the ionic precursors must be fine-tuned to increase the absorbance efficiency and make the desired reaction temperature achievable at the maximum power of the microwave synthesizer but also avoid uncontrollable nucleation which lead to agglomeration of the particles. In this dissertation, the synthesis of Ge NPs was primarily performed within a quartz reaction vessel with rubber cap and PTFE liner in a CEM microwave reactor with a built-in infrared temperature sensor and pressure sensor. The power output is controlled dynamically by the computer to maintain the reaction temperature. The CEM microwave reactor is shown in Figure 2.1.

Figure 2.1 Photograph of the CEM microwave reactor.

2.3 Characterization

2.3.1 UV-Vis Spectrophotometry

Ultraviolet-visible (UV-Vis) Spectrophotometry is a widely used analytical technique in many areas of science which measures the amount of discrete wavelengths of UV or visible light that are absorbed by or transmitted through a sample in comparison to a reference or blank sample. Typically, the light source for an UV-vis spectrophotometer employs two lamps, a tungsten or halogen lamp is commonly used for visible light while a deuterium lamp is the common source of UV light. The light source in the instrument is switched during the measurement to fully cover both the UV and visible wavelengths. To precisely measure the excitation wavelength that is absorbed, a monochromator based on diffraction gratings that can be rotated to choose incoming and reflected angles to select the desired wavelength of light is used and select a narrow band of wavelength to pass through the sample. If the molar absorptivity, ε, of a material is known the concentration can be calculated using Beer's law.

Equation 2.1: $A = \log (P_0/P) = \varepsilon lc$

Here, ε is a proportionality constant called the molar absorptivity which has the units of $L\ mol^{-1}\ cm^{-1}$. The terms P_0 and P refer to the power of a beam that has passed through cells containing the blank (solvent) and the analyte, respectively. According to Beer's law, absorbance is directly proportional to the concentration of the absorbing species c in moles per liter and to the path length l of the cuvette of the absorbing medium in centimeters. While the molar absorptivity is largely unknown for most of the nanoparticles, which makes quantitatively characterizing the concentration of nanoparticle dispersion very challenging, it can still serve as a powerful tool to provide information about composition, morphology, and relative concentration of the sample.

UV-Vis spectrophotometry can also provide useful insights into band gap energies of the semiconductor nanoparticles through the determination of the absorbance onset and locate the surface plasmon resonance for metal nanoparticles.

When a metal nanoparticle experiences an electric field, polarization of a loosely bound electron cloud occurs upon stimulation by the incident light beam. This results in a charge separation. Hence, a linear restoring force is exerted by the positively charged nuclei. Therefore, collective, in-phase oscillations of the valence electrons occur on the solid material surface, which is called the surface plasmon phenomenon. When the frequency of the photon matches the natural frequency of the metallic electron oscillation against the restoring force of the positive nuclei, the resonance condition is established provided the metal possesses a negative real and small positive imaginary dielectric constant. Under this condition, surface plasmon resonance (SPR) is observed.[13, 14]

2.3.2 X-ray Diffraction (XRD)

X-ray diffraction crystallography for powder samples is well-established and widely used in the field of materials characterization to obtain compositional and structural information. The diffraction beam of sufficient intensity is detected only when the scattered X-rays from atoms and the incident X-rays are completely in phase and reinforce each other to produce a detectable diffraction beam, or when the “Bragg law” is satisfied:

Equation 2.2: $$n\lambda = 2d\ sin\theta$$

Where n is called the order of reflection and is equal to the number of wavelengths in the path difference between diffracted X-rays from adjacent crystal planes, λ is the wavelength of the incident X-rays and d is the interplanar spacing of the crystal. θ represents the angle between the detector and the diffraction plane.

Powder X-ray diffraction patterns were collected on a Bruker D8 Advance diffractometer using Cu radiation (Cu-Kα: $\lambda = 1.541$ Å). The X-ray diffraction patterns were collected for 2θ values ranging between 20° and 75° with a step size of 0.02°. Nanoparticle samples were first dispersed in a solvent and then dropped onto a zero-background quartz holder and dried under a gentle air flow. The drop casting was repeated several times to create a uniform film on the quartz holder.

2.3.3 Transmission Electron Microscopy (TEM)

2.3.3.1 Working Principles of TEM

TEM is a microscope technique that uses a particle beam of electrons to visualize specimens and generate a highly magnified image. In a TEM, high energy electrons are produced and pass through a series of condenser lenses to focus the beam onto the object and through an image-producing system, consisting of objective lens, intermediate and projector lenses, which focus the electrons passing through the specimen, to form a real, highly magnified image.

Like an optical microscope, the resolution of an electron microscope is limited by the classic Rayleigh criterion:

Equation 2.3:
$$\delta = \frac{0.61\,\lambda}{\mu \sin \beta}$$

Where λ is wavelength, μ the refractive index, and β is the semi-angle of collection of the lens. The product $\mu\sin\beta$ is known as the numerical aperture (NA) of the lens.

For an electron lens in a vacuum, μ can be assumed to be unity and $\sin\beta \approx \beta$ (when β, the semi-angle collected by the lens, is less than a few degrees). Hence:

Equation 2.4:
$$\delta \approx \frac{0.61\,\lambda}{\beta}$$

From the equation, better resolution can be achieved when using a smaller wavelength and the wavelength of electrons is related to their energy eV and can be shown as de Broglie's equation, if the relativistic effects is ignored:

Equation 2.5: $$\lambda = \frac{h}{mv} = \frac{h}{\sqrt{2m_0eV)}}$$

Where h is Plank's constant, m_0 is the electron mass. However, when the velocities of electrons reach about 70% the speed of light with the energy of electron is more than 200 keV, relativistic effects must be considered:

Equation 2.6: $$\lambda = \frac{h}{[2m_0eV(1+\frac{eV}{2m_0c^2})]^{\frac{1}{2}}}$$

As such, a 300 keV electron has a wavelength of ~ 1.96 pm, which is much smaller than the diameter of an atom. Such a high energy electron beam used in a TEM enables unprecedented resolution and allows for detailed characterization of nanomaterials.

The operating conditions of the TEM can vary significantly depending on the nature of the sample and the information needs to be extracted. For example, in TEM mode, the specimen is illuminated with a parallel beam of electrons whereas a convergent beam is required for STEM. The different imaging conditions with parallel beam in TEM mode and convergent beam in STEM mode are illustrated in Figure 2.2.[15]

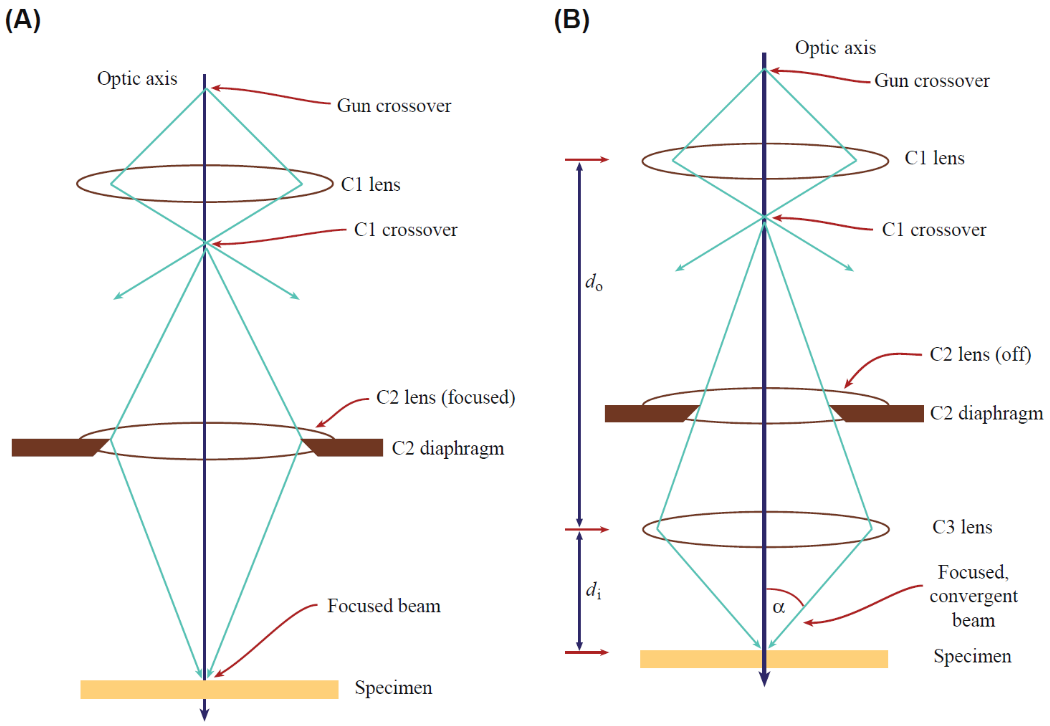

Figure 2.2. A simplified scheme of parallel beam (a) and convergent beam (b) condition in the TEM. Reprinted from ref (15) with permission.

2.3.3.2 Imaging Mechanisms

To recognize a sample object on a TEM image, sufficient contrast is needed, which is defined by:

Equation 2.7:

$$C = \frac{(I_2 - I_1)}{I_1} = \frac{\Delta I}{I_1}$$

where ΔI is the intensity difference of I_1 and I_2 from two adjacent areas.

TEM image contrast may be classified as scattering contrast (or amplitude contrast), and phase contrast. The scattering contrast in the TEM mode can be further categorized by two different types: mass-thickness contrast and diffraction contrast.

Mass-thickness contrast is largely due to elastic scattering from individual atoms, where the incident electrons are deflected by Coulomb interactions as they pass through the atom. As shown in Figure 2.3,[15] a high mass region scatters electrons at larger angles than the low mass region. After deflection by the objective lens, the electrons at larger angles are thus excluded by the objective aperture, and fewer electrons from the high mass area contribute to the imaging and form a darker imaging on the image plane. Whereas the low mass area forms a brighter area in the BF image. Thickness makes similar effect as the mass. A thick area scatters electrons at larger angles than a thin area, and thus it appears as a darker area in the image. It's worthy to point out that, the accelerating voltage also affects the mass-thickness contrast. While a decrease the accelerating voltage will deteriorate the imaging resolution, a lower accelerating voltage will increase the scattering angle and cross section, resulting in an increase in contrast of the imaging.[16]

In comparison, diffraction contrast depends on coherent elastic scattering (Bragg diffraction) and is caused by the disturbance of the Bragg reflected beam by local defects or dislocations in the materials.[17] This contrast emphasizes the effect of defects on the amplitude of the transmitted wave, thus also called amplitude contrast.[18] For amorphous material, due to the lack of long-range periodicity in the structure, the sample does not diffract electrons to form the Bragg diffraction, thus their image contrast in TEM is only from the mass-thickness effect.

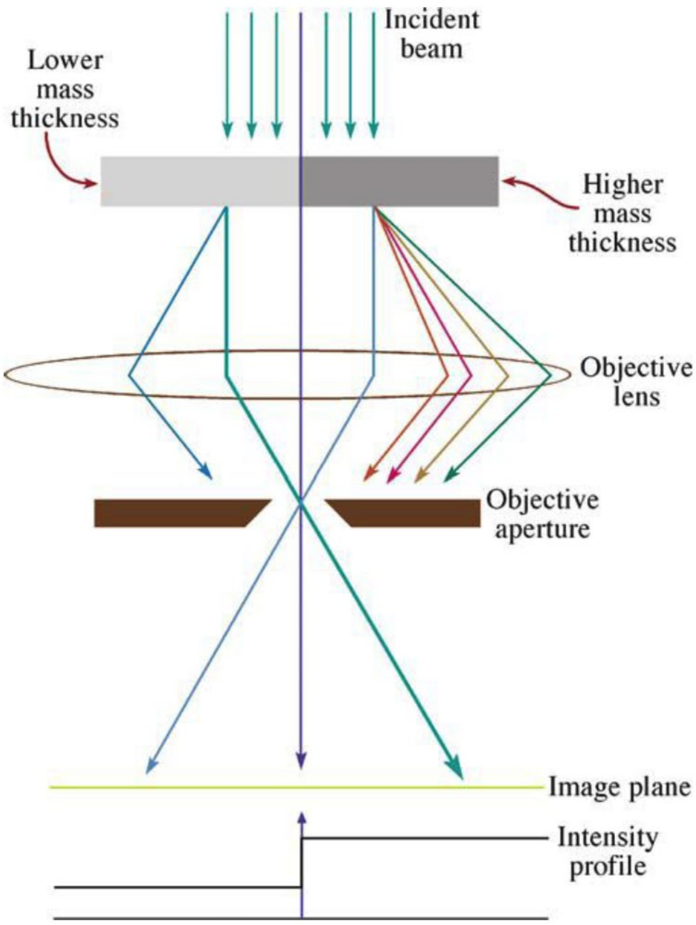

Figure 2.3. Mechanism of mass-thickness contrast in a BF image. Reprinted from ref (15) with permission.

On the other hand, for high resolution TEM (HRTEM), where required resolution is comparable with the coherence width, the scattering contrast is no longer adequate and phase contrast becomes the dominant contrast mechanism. Phase contrast is produced by the phase differences of the incident electrons which are scattered elastically and coherently through a thin specimen. The kinetic energy of the electrons is disturbed by the change of the crystal's potential field, which cause a phase shift relative to the electron wave propagating in the potential field-free space.[19] Fresnel fringes, lattice fringes, and atomic-resolution imaging are three examples of phase contrast.

2.3.3.3 High-angle Annular Dark-field Scanning Transmission Electron Microscopy (HAADF-STEM)

In contrast to bright field TEM, which is using a parallel beam to illuminate the whole image area simultaneously, scanning transmission mode uses a focused small electron probe to scan the specimen in a raster point-by-point. To minimize the contribution of Bragg scattering, an annular DF detector with a very large central aperture is used and HAADF-STEM images are formed from incoherent electrons elastically scattered at a high semi-angle, > 50 mrad (~3°).[20-24] The contrast in HAADF-STEM images is also called Z-contrast because the scattering intensity at such high angles is proportional to the square of the atomic number, Z^2, according to the Rutherford scattering formula. A schematic image of the HAADF detector setup for Z-contrast imaging in a STEM is shown in Figure 2.4.[15]

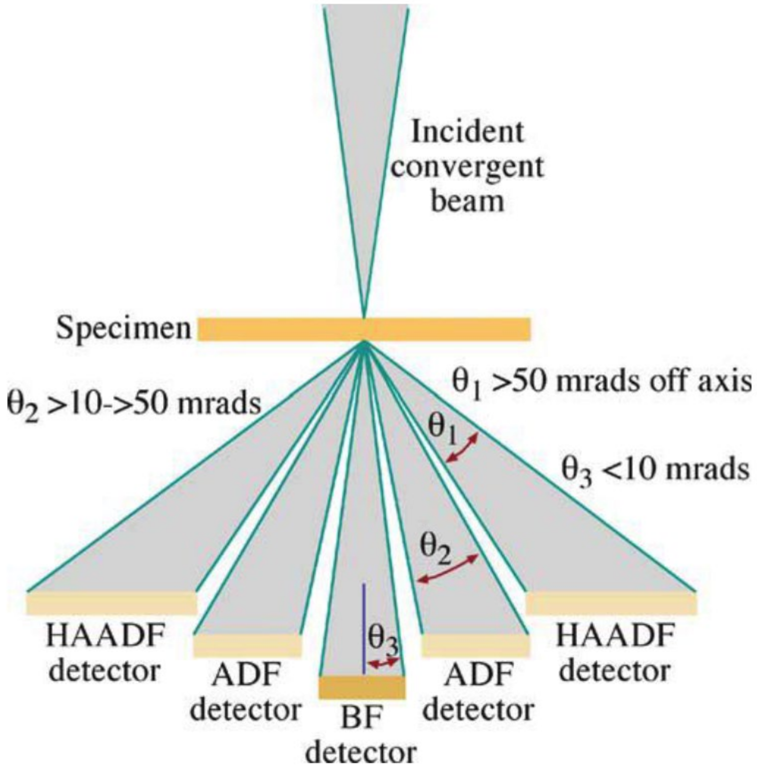

Figure 2.4. Schematic of the HAADF detector. Z-contrast images are formed using incoherent electrons elastically scattered at a high angle (> 50 mrad). Reprinted from ref (15) with permission.

2.3.3.4 Energy Dispersive Spectroscopy (EDS)

Energy dispersive spectroscopy is used to both qualitatively and quantitatively identify elemental composition and distribution within a sample by collecting emitted characteristic X-rays, which is produced when a high-energy beam electron ionized the sample atoms. The EDS is usually used as an add-on component to the electron microscopes such as scanning electron microscope (SEM) and STEM. When an inner shell electron is ejected from the atom by a high-energy electron and leaves a hole, an outer shell electron will fill the hole and emit a quantity of energy in the form of an X-ray whose energy is the difference between the two energy levels. A schematic diagram of the process of characteristic X-ray emission is shown in Figure 2.5.[15] The emitted X-ray is characteristic of the element due to its unique atomic energy levels and thus can be used as a fingerprint of the element. The small size of the scanning electron probe enables the feasibility of acquiring EDS data from individual nanocrystals. By collecting EDS signal at each scanning position of the beam, a high spatial resolution map can be generated to reflect the elemental distribution throughout the nanostructures. While EDS is an important tool for material analysis, it is more sensitive to heavy elements due to the fluorescence effect arising from Auger emission for light element.[25, 26]

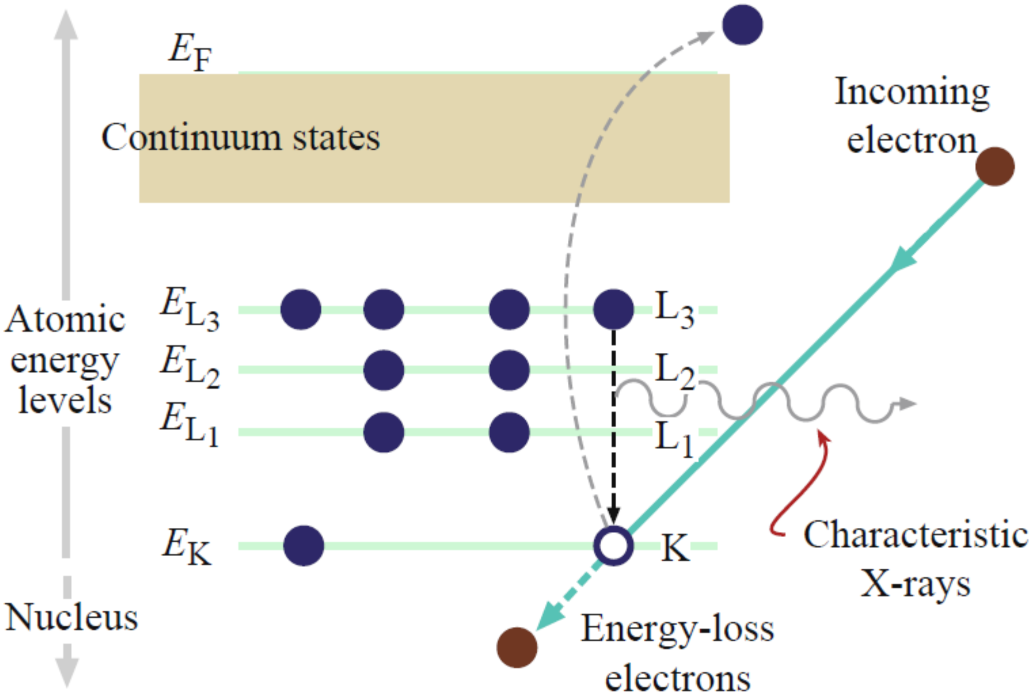

Figure 2.5. Schematic diagram of the ionization process. A high-energy electron kicks out an inner (K) shell electron and leaves a hole, which is filled by an electron from the outer (L) shell electron and characteristic (Kα) X-ray emission occurs due to the energy difference between the two shells. Reprinted from ref (15) with permission.

2.3.3.5 Limitations

Electron microscopy is a powerful characterization technique, however, there are certain limitations. First, the information is two-dimensional (2D), which means most of the spatial information in the direction of the electron beam is lost, and consequently, interpretation of the TEM image must be very careful as some of the information cannot be discerned directly from the image.[27] For example, a tetrahedral nanoparticle may look like a triangle nanoplate in a TEM image. To correctly reveal the structural information, supplementary methods such as electron tomography need to be used. Second, due to the nature of TEM study, which can only analyze a limited number of particles at a time, there are always concerns about whether the observations were representative of the rest of the sample or even the bulk materials. Thus, the structural and electronic observation by TEM can sometimes be biased. Complementary bulk measurement techniques (e.g., synchrotron X-ray techniques, XRD, and UV-vis) which can probe an enormous number of particles at a time and are ensemble averaged, can be added as characterization tools to correctly reveal the property of the sample. Third, the effects of beam damage should always take into consideration, the high energy electron beam can damage sample due to knock-on or ionization mechanisms.[28] Plus, the electron beams can add extra energy to increase the mobility of the atoms in the sample, change local temperature or pressure, induce physical or chemical reactions, etc., therefore, special care is needed to minimize the artifacts arising from the electron beam.

2.3.3.6 Experimental Techniques

In this dissertation, a variety of different TEM based techniques are used as the primary characterization tool to study the size, morphology, chemical composition, elementary distribution as well as thermal stability of the as synthesized Ge based nanoparticles. In Chapter 3, Ag NPs are characterized by both TEM and HAADF-STEM to reveal the polycrystalline nature as well as the size distribution. The size and shapes of solid and hollow Ge nanoparticles are mainly studied by HAADF-STEM because of the low image contrast in the TEM mode arise from their completely amorphous nature. In Chapter 4, HAADF-STEM is used to investigate the structure of the Ag@Ge core-shell nanoparticles due to the large difference in Z between Ge and Ag. Even though HAADF-STEM produces high quality images of these particles, it requires a much longer recording time than a TEM image which use a parallel beam to obtain sufficient contrast and signal-to-noise ratio. The in-situ heating experiments are primarily conducted in BF-TEM mode by using a high-speed scintillator-based CMOS camera (FEI Ceta2) to study the crystallization of the amorphous Ge NPs with high image resolution and fast-recording capability. EDS maps are used to reveal the chemical distribution in Ag@Ge core-shell NPs.

TEM samples are prepared by putting one droplet of toluene dispersion of the as-synthesized NPs on copper grids coated with ultrathin amorphous carbon films and heating under vacuum overnight to minimize the carbon contamination. TEM data were acquired using a FEI ThemIS 60–300 STEM/TEM (Thermo Fisher Scientific, US) operated at 300 kV at the National Center for Electron Microscopy within the Molecular Foundry in Lawrence Berkeley National Laboratory. The ThemIS is equipped with image aberration corrector optics, a Ceta2 camera (4k × 4k pixels, and 14-bit dynamic range) for the TEM image and a Bruker Super-X Quad windowless detector with a solid angle of 0.7 steradian for the acquiring of EDS maps.

2.4 References

1. Spencer, P. L. Method of treating foodstuffs. 2495429, 1950.
2. Liu, S. W.; Wightman, J. P., Decomposition of simple alcohols, ethers and ketones in a microwave discharge. *Journal of Applied Chemistry and Biotechnology* **1971,** *21* (6), 168-172.
3. Adam, D., Out of the kitchen. *Nature* **2003,** *421* (6923), 571-572.
4. Galema, S. A., Microwave chemistry. *Chemical Society Reviews* **1997,** *26* (3), 233-238.

5. Bykov, Y. V.; Rybakov, K. I.; Semenov, V. E., High-temperature microwave processing of materials. *Journal of Physics D: Applied Physics* **2001,** *34* (13), R55-R75.

6. Mingos, D. M. P.; Baghurst, D. R., Tilden Lecture. Applications of microwave dielectric heating effects to synthetic problems in chemistry. *Chemical Society Reviews* **1991,** *20* (1), 1-47.

7. Zhu, Y.-J.; Chen, F., Microwave-Assisted Preparation of Inorganic Nanostructures in Liquid Phase. *Chemical Reviews* **2014,** *114* (12), 6462-6555.

8. Gabriel, C.; Gabriel, S.; H. Grant, E.; H. Grant, E.; S. J. Halstead, B.; Michael P. Mingos, D., Dielectric parameters relevant to microwave dielectric heating. *Chemical Society Reviews* **1998,** *27* (3), 213-224.

9. L. F. Chen, C. K. O., C. P. Neo, V. V. Varadan, V. K. Varadan, *Microwave Electronics: Measurement and Materials Characterization*. John Wiley & Sons, Ltd: 2004.

10. Baghbanzadeh, M.; Carbone, L.; Cozzoli, P. D.; Kappe, C. O., Microwave-Assisted Synthesis of Colloidal Inorganic Nanocrystals. *Angewandte Chemie International Edition* **2011,** *50* (48), 11312-11359.

11. Kappe, C. O., How to measure reaction temperature in microwave-heated transformations. *Chemical Society Reviews* **2013,** *42* (12), 4977-4990.

12. Robinson, J.; Kingman, S.; Irvine, D.; Licence, P.; Smith, A.; Dimitrakis, G.; Obermayer, D.; Kappe, C. O., Understanding microwave heating effects in single mode type cavities—theory and experiment. *Physical Chemistry Chemical Physics* **2010,** *12* (18), 4750-4758.

13. Ghosh, S. K.; Pal, T., Interparticle Coupling Effect on the Surface Plasmon Resonance of

Gold Nanoparticles: From Theory to Applications. *Chemical Reviews* **2007,** *107* (11), 4797-4862.

14. Jana, J.; Ganguly, M.; Pal, T., Enlightening surface plasmon resonance effect of metal nanoparticles for practical spectroscopic application. *RSC Advances* **2016,** *6* (89), 86174-86211.

15. Williams, D. B.; Carter, C. B., *Transmission Electron Microscopy - A Textbook for Materials Science*. 2 ed.; Springer, Boston, MA: 2009; p LXII, 775.

16. Luo, Z., *A practical guide to transmission electron microscopy : fundamentals / Zhiping Luo*. First edition. ed.; Momentum Press: New York, [New York] (222 East 46th Street, New York, NY 10017), 2016.

17. Hirsch, P. B., *Electron microscopy of thin crystals by P.B. Hirsh ... [et al.]*. Butterworths: London, 1969.

18. Wang, Z. L., Transmission Electron Microscopy of Shape-Controlled Nanocrystals and Their Assemblies. *The Journal of Physical Chemistry B* **2000,** *104* (6), 1153-1175.

19. Kohli, R.; Mittal, K. L., *Developments in Surface Contamination and Cleaning, Vol. 1: Fundamentals and Applied Aspects*. Elsevier Science & Technology Books: Norwich, 2015.

20. Zhang, J. Y.; Hwang, J.; Isaac, B. J.; Stemmer, S., Variable-angle high-angle annular dark-field imaging: application to three-dimensional dopant atom profiling. *Scientific Reports* **2015,** *5* (1), 12419.

21. Krivanek, O. L.; Chisholm, M. F.; Nicolosi, V.; Pennycook, T. J.; Corbin, G. J.; Dellby, N.; Murfitt, M. F.; Own, C. S.; Szilagyi, Z. S.; Oxley, M. P.; Pantelides, S. T.; Pennycook, S. J., Atom-by-atom structural and chemical analysis by annular dark-field electron microscopy. *Nature* **2010,** *464* (7288), 571-574.

22. Couillard, M.; Radtke, G.; Knights, A. P.; Botton, G. A., Three-Dimensional Atomic Structure of Metastable Nanoclusters in Doped Semiconductors. *Physical Review Letters* **2011,** *107* (18), 186104.

23. van Benthem, K.; Lupini, A. R.; Oxley, M. P.; Findlay, S. D.; Allen, L. J.; Pennycook, S. J., Three-dimensional ADF imaging of individual atoms by through-focal series scanning transmission electron microscopy. *Ultramicroscopy* **2006,** *106* (11), 1062-1068.

24. Utsunomiya, S.; Ewing, R. C., Application of High-Angle Annular Dark Field Scanning Transmission Electron Microscopy, Scanning Transmission Electron Microscopy-Energy Dispersive X-ray Spectrometry, and Energy-Filtered Transmission Electron Microscopy to the Characterization of Nanoparticles in the Environment. *Environmental Science & Technology* **2003,** *37* (4), 786-791.

25. Tawara, H.; Harrison, K. G.; De Heer, F. J., X-ray emission cross sections and fluorescence yields for light atoms and molecules by electron impact. *Physica* **1973,** *63* (2), 351-367.

26. Dick, C. E.; Lucas, A. C., K-Shell Fluorescence Yields for Light Elements. *Physical Review A* **1970,** *2* (3), 580-586.

27. Robertson, I. M.; Schuh, C. A.; Vetrano, J. S.; Browning, N. D.; Field, D. P.; Jensen, D. J.; Miller, M. K.; Baker, I.; Dunand, D. C.; Dunin-Borkowski, R.; Kabius, B.; Kelly, T.; Lozano-Perez, S.; Misra, A.; Rohrer, G. S.; Rollett, A. D.; Taheri, M. L.; Thompson, G. B.; Uchic, M.; Wang, X.-L.; Was, G., Towards an integrated materials characterization toolbox. *Journal of Materials Research* **2011,** *26* (11), 1341-1383.

28. Frenkel, A. I.; Cason, M. W.; Elsen, A.; Jung, U.; Small, M. W.; Nuzzo, R. G.;

Vila, F. D.; Rehr, J. J.; Stach, E. A.; Yang, J. C., Critical review: Effects of complex interactions on structure and dynamics of supported metal catalysts. *Journal of Vacuum Science & Technology A* **2013,** *32* (2), 020801.

Chapter 3

Ge Nanocages and Nanoparticles via Microwave-Assisted Galvanic Replacement for Energy Storage Applications

Chapter 3, in full, is a reprint of the material as it appears in ACS Appl. Nano Mater. 2020, 3, 6, 5509–5520, Xiao Qi and Susan M. Kauzlarich, American Chemical Society Press, 2020. The dissertation author was the primary investigator and author of this paper.

3.1 Abstract

We report a systematic study on the synthesis of highly monodisperse hollow germanium (Ge) nanoparticles (NPs) via galvanic replacement reactions between GeI_2 and Ag NPs. By fine-tuning the synthetic parameters such as temperature, precursor molar ratio, ligand concentration, and so forth, the morphology and surface structure of the Ge NPs can be precisely controlled. We also report a method to synthesize solid Ge NPs and Ag@Ge core–shell metal–semiconductor NPs with a controllable uniform shell thickness. An inward diffusion mechanism for galvanic replacement is proposed and supported by imaging the different stages of the reaction and analysis of the products. This mechanism allows the reaction to be self-terminated and achieves nanometer-sized accuracy. The galvanic reaction may be

applied to other semiconductors and could serve as a powerful alternative to the classical nucleation-growth mechanism and subsequently advance the scale-up and further energy storage applications.

3.2 Introduction

The search for high-energy-density electrode materials is prompted by the large market demand for new energy-storage devices and electric vehicles worldwide.[1-5] The substantial increase in charge capacity of battery particularly relies on the improvement of the anode materials.[6] Nanostructured germanium (Ge) is one of the most promising candidates for the next-generation anode materials for lithium-ion battery applications owing to its high Li storage densities and high lithium-ion diffusivity and conductivity.[7-9] Because of the low cost and flexibility of solution-based processing techniques such as spin-coating, spray-coating, inkjet and screen printing, many efforts have been made aiming to develop colloidal synthetic methods for the preparation of Ge nanoparticles (NPs). Although progress has been made over the last decade,[10] less successes on morphology and size control of colloidal Ge NPs has been achieved. Compared to the ubiquitous II–VI, III–V, IV–VI semiconductor and noble metal nanocrystals, well-defined shapes are more difficult to achieve for Ge nanomaterial synthesis because of the strong covalent nature of Ge–Ge bonds. Thus, common strategies such as thermal decomposition or reduction of organogermane precursors usually lead to unstable products.[11-12] Therefore, a facile and versatile synthesis route to shape directed Ge nanostructures is highly desirable and a thorough understanding of the reaction mechanism is vital for further scale-up and energy storage applications. In addition to the conventional synthetic strategies, a galvanic replacement reaction provides a simple and versatile route for reducing noble metal precursors and generating nanostructures with controllable pores and compositions. During the past 2 decades, many elegant and remarkable syntheses have been performed by cooperative galvanic replacement reactions and have produced a variety of nanoscale structures with complex morphologies.[13-17] Most of the research work was based on the transformation of noble metals such as Au, Pd, and Pt because of their robustness. For example, the reaction mechanism between single-crystal silver nanocubes and chloroauric acid has been studied by many groups.[18-23] However, synthesis of a semiconductor nanostructure via galvanic replacement reaction has been rarely reported and not well studied. Most of the successful galvanic replacement reactions were performed in aqueous solution, typically possess a very low energy barrier, and can be easily triggered at room or lower temperatures. This is not the case for semiconductor materials because of their strong covalent bonding nature, plus they can be air- and water-sensitive, which means that the reaction can only be performed under a nonaqueous and air-free environment. In addition, because of the lack of understanding of such a mechanism, it is hard to find a suitable binding ligand to not only stabilize the template particles and products but also to facilitate the replacement reaction under moderate synthesis conditions. We demonstrated the unconventional transformation of inorganic germanium precursors (e.g., GeI_2) to hollow Ge NPs through galvanic replacement with Ag NPs.[24] In this reaction, Ge^{2+} oxidizes Ag to Ag^+, which causes the hollowing-out of the sacrificial Ag NP templates. However, the details of the mechanism have remained largely unknown because of the complexity of the reaction system. For example, unlike the conventional galvanic replacement reaction between noble metals, the large lattice mismatch between Ag and Ge (38.7%) would prevent the formation of alloy nanostructures, which is a common intermediate product for such replacement reaction; thus, a new reaction mechanism needs to be proposed. What is more, the specific roles of each reagent in the galvanic replacement between GeI_2 and Ag NPs need to be understood to help develop an efficient and highly reproducible process for producing hollow Ge NPs with high yield and desirable qualities (e.g., narrow size distribution, well-defined morphology, etc.). Scheme 3.1 provides a diagram of the synthetic route and impact of the parameters investigated. A better understanding of the reaction mechanism and the interaction of the various components to the structural evolution provides vital information for scale-up and industrial applications.

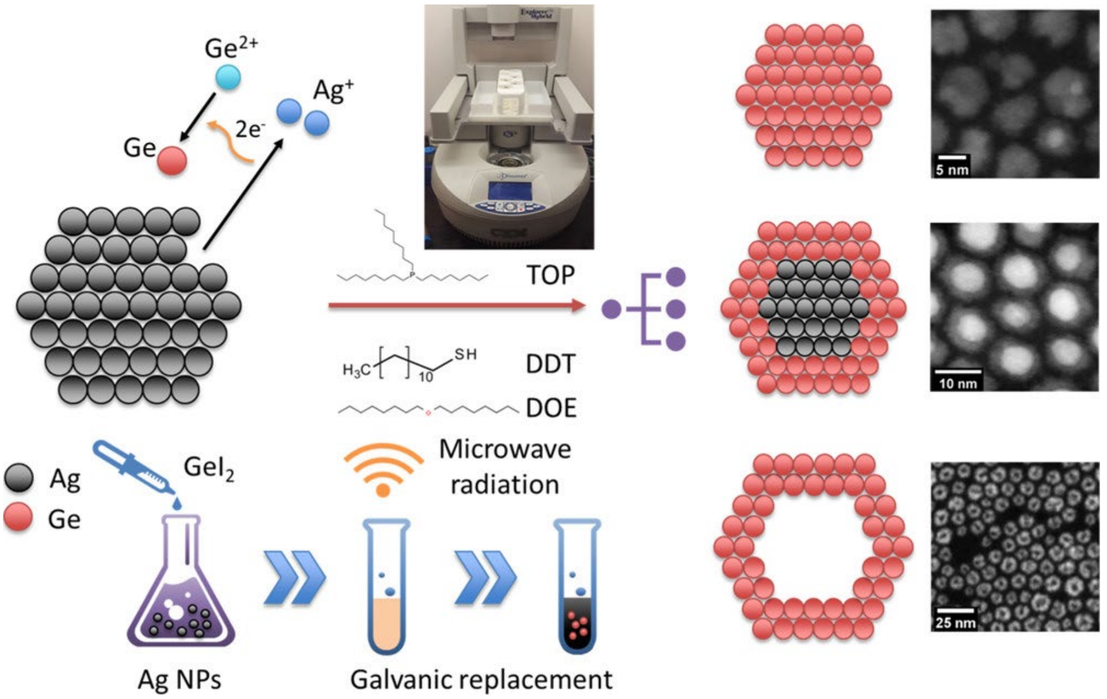

Scheme 3.1. Microwave Reaction of GeI_2 with Ag NPs and the Impact of Various Organic Reagents on the Shape and Composition of the Final Product

3.3 Results and Discussion

In this work, spherical Ag NPs is used as the sacrificial template for the synthesis of Ge NPs through a galvanic replacement reaction, in which GeI_2 is directly reduced by Ag and deposited onto the surface of the Ag NPs. To explore the mechanism of this unconventional galvanic replacement reaction between metal NPs and semiconductor precursors, a systematic study was performed by varying the synthesis conditions including the concentration of ligands, temperature, reaction time, etc., and then characterize the products by HAADF-STEM.

3.3.1 Synthesis of Ag NPs

A one-step synthesis of Ag NPs in an organic solvent was performed by optimizing a previously reported procedure.[25-27] The Ag NPs (shown in Figure 3.1) were stabilized by OAm ligands and remain stable in air for several days. Characterization by TEM showed that the Ag NPs are spherical and have a narrow size-distribution (9.51 ± 0.62 nm). Lattice fringes indicate that the Ag NPs are polycrystalline. The UV–vis spectrum displayed the expected surface plasmon resonance band with an absorbance maximum at 421 nm.[25-26]

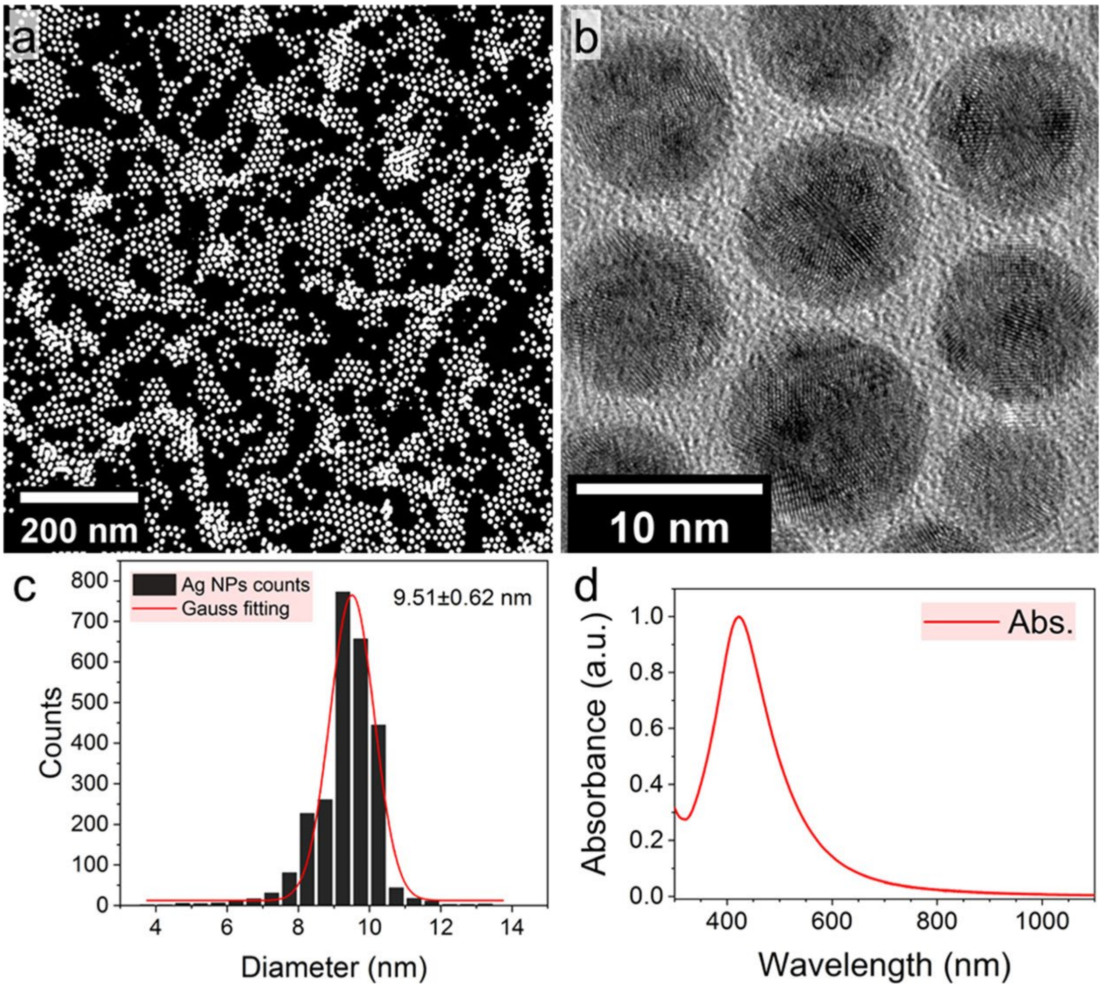

Figure 3.1. (a) Dark-field STEM image of as-synthesized spherical, oleylamine-stabilized Ag NPs. (b) Bright-field HRTEM image of the Ag NPs. (c) Histogram data of the size distribution from (a). An average size of 9.51 nm and a standard deviation about 0.62 nm were calculated from Gaussian fitting to the histogram. (d) UV–vis spectrum of Ag NPs in toluene. The surface plasmon resonance shows a maximum at 421 nm.

3.3.2 Synthesis of Ge NPs

Ge NPs are synthesized under an elevated temperature via galvanic replacement by employing Ag NPs as the sacrificial template with DOE as an aprotic solvent and TOP and DDT as the cosurfactants. The anisotropic growth and structural evolution during galvanic replacement are systematically investigated by using ex situ methods after systematically adjusting the synthetic parameters. The results provide insight into the mechanism and the roles of each component on the final products.

3.3.3 Role of TOP

To investigate the role of TOP, the amount of TOP was gradually increased while keeping all other reaction parameters the same. The Ag/Ge molar ratio was kept as 2:1, which is the exact stoichiometric relationship according to the galvanic replacement reaction: $2Ag + GeI_2 \rightarrow Ge + 2AgI$. In this synthesis, GeI_2 is first added to TOP and sonicated for 10 min. A clear yellowish solution appears, which indicates that GeI_2 is completely dissolved. When the molar ratio between TOP and Ge is increased from 8:1 to 16:1 and finally to 32:1, hollow Ge NPs were produced exclusively in all cases as seen in the HAADF-STEM images in Figure 3.2 a–f. The hollow Ge NPs are totally Ag-free, indicating complete galvanic replacement. The high magnification images in Figure 3.2 show that hollow Ge NPs synthesized with lower TOP content result in a bumpy and rough surface, whereas a higher TOP content results in hollow Ge NPs that are smoother on the surface. This result could be explained by the influence of TOP concentration on the mobility of Ge^{2+} and AgI in the solution. We propose that the higher concentration of TOP decreases the affinity of Ge^{2+} to the Ag NPs surface, thus lowering the deposition rate of Ge atoms, which allows the Ge atoms sufficient time to migrate to the particle surface. The slower rate of deposition and atom/ion mobility would eventually reduce the dangling bonds, lower the overall surface energy, and thus increase the smoothness of the hollow Ge NPs. On the other hand, TOP also served as an important solvent to dissolve GeI_2. As GeI_2 does not dissolve in DOE, our attempt to synthesize the Ge NPs without TOP failed because of the solubility issue. By adding GeI_2 directly into the microwave vessel which was preloaded with Ag NPs, DOE, and DDT and heating at 200 °C for 30 min, no Ge NPs are obtained and GeI_2 powder is still present as a sediment at the bottom of the microwave tube.

Although this surface shape-directing effect of TOP is rarely found in the literature, similar results were reported by Xia and co-workers when they compared the galvanic replacement between Ag nanocubes and Pd^{2+} or Pt^{2+} ions in aqueous solution.[28] Whereas the reaction of Ag nanocubes with Na_2PdCl_4 resulted in the formation of smooth Pd–Ag nanoboxes, Pt nanoboxes with bumpy surfaces were formed if Na_2PdCl_4 was replaced by Na_2PtCl_4. It is well known that alloying is the basis for retaining the morphology of the original template during a galvanic replacement reaction.[16] In their case, the Pt and Ag cannot form a homogenous alloy at the synthesis temperature (100 °C) because of the high bonding energy of Pt–Pt, which leads to the continuous nucleation and growth of Pt on the Ag nanocube surface and forms an amorphous rough layer on the Ag nanocubes.

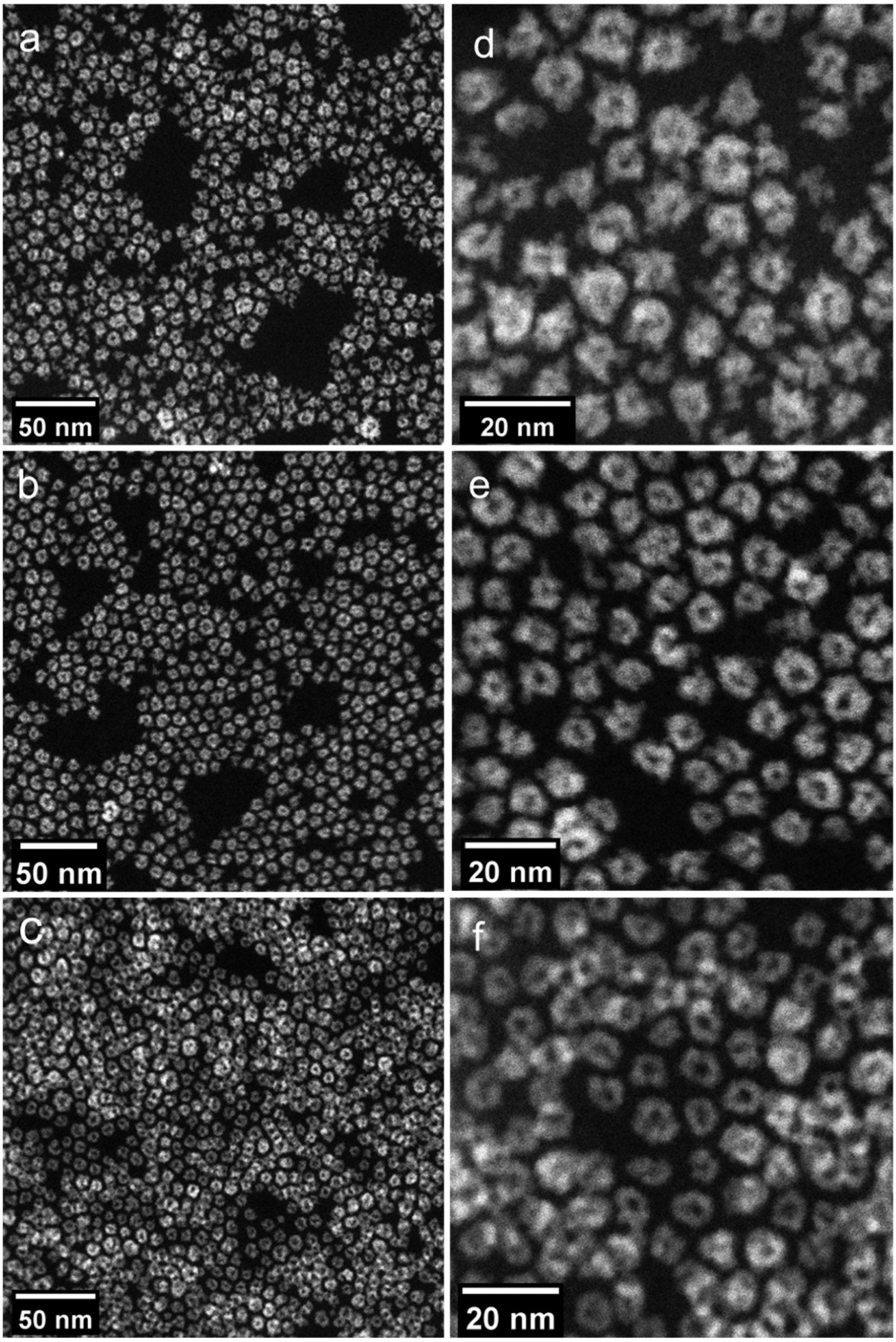

Figure 3.2. (a–c) HAADF-STEM images of hollow Ge NPs synthesized from the same batch of Ag NPs via galvanic replacement reaction. The TOP/Ge molar ratios are (a) 8:1, (b) 16:1, (c) 32:1. Scale bars are all 50 nm. (d) High-magnification image from (a), the surface of the

hollow Ge NPs is bumpy and rough. (e) High-magnification image from (b), the Ge NPs are smoother than in (d). (f) High-magnification image from (c), the as-synthesized Ge NPs have a very smooth surface with a well-defined interior.

3.3.4 Role of DDT

DDT is a common L-type capping ligand which contains an electron-rich thiol group and behaves as a Lewis base which coordinates to the electron-poor Lewis acid-like metal or semiconductor NPs. This coordination passivates the dangling bonds at the surface, and the long alkane chain helps to prevent further growth or agglomeration through van der Waals forces.[29] This strategy usually benefits from having the capping molecule in large excess, which helps to efficiently protect the particle surface without changing the particle shape. However, our study shows that the excess amount of DDT can also change the morphology of the final products and generate porous Ge nanocages. By simply increasing the concentration of the capping ligand, DDT, while keeping the Ge^{2+} ion concentration constant, more vacancies are generated on the surface of the particles, which leads to the formation of more complex Ge nanocages and nanoframes. To understand the role of DDT in the synthesis, the molar ratio of DDT/Ag was changed from 4 to 20 while keeping all other parameters constant. As the HAADF-STEM images show in Figure 3.3, when the molar ratio of DDT/Ag is equal to 4, uniform hollow Ge NPs were synthesized with a small number of larger particles, which are present as the brighter particles in the HAADF-STEM image. However, when the molar ratio between DDT and Ag NPs was increased to 8, the amount of larger and thicker hollow Ge NPs was significantly increased. Figure 3.3 e clearly shows the nanoframe morphology and multiple porous walls. This trend continues with DDT and Ag NP molar ratio of 12, as Figure 3.3 f shows that the nanocages became a dominant morphology of the overall particles. However, when the molar ratio between DDT and Ag NPs was further increased to 16 and even 20, the yield of hollow Ge NPs dramatically decreased, resulting in an amber/orange color solution, which may be due to dissolving and the collapse of the nanocage structure. These results indicate the important role of DDT in the geometry evolution of the nanocage formation process. Similar to the discussion on the role of TOP, regardless of the DDT/Ag molar ratio, the resulting hollow Ge NPs are all Ag content free, which suggests that all the Ag NPs are completely oxidized to Ag^+ and removed with the isolation process.

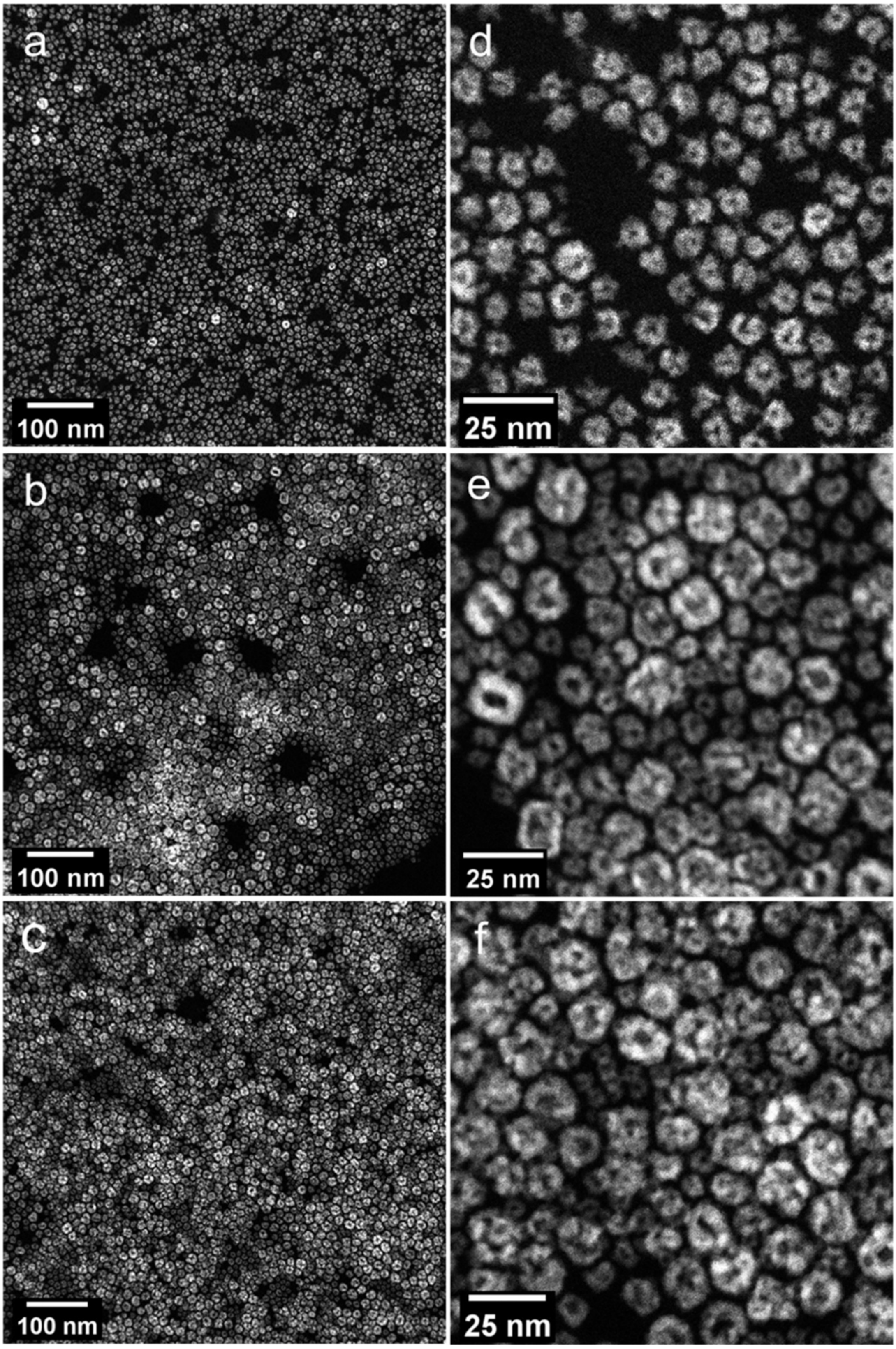

Figure 3.3. (a) HAADF-STEM images of hollow Ge NPs synthesized from the same batch of Ag NPs via galvanic replacement reaction with the variation of DDT/Ag molar ratio of (a) 4:1, (b) 8:1, (c) 12:1. Scale bars are all 100 nm. (d) High-magnification image from (a), the as-

synthesized hollow Ge NPs have uniform size and thickness. (e) High-magnification image from (b), the Ge NPs are polydisperse in terms of both size and thickness. Some of the particles are apparently larger and show a nanocage structure (f) high-magnification image from (c), the image shows a majority of more complex nanocage structures with a larger size.

Previous studies show that the formation of nanocages with multiple porous walls is involved with the dealloying process of a bimetallic system.[16,19,30,31] The dealloying can be achieved either by increasing the metal ion concentration or by utilizing a selective etchant to remove the metal template.[19,30] In the galvanic replacement reaction between Ag NPs and GeI_2, DDT can act as a selective etchant which facilitates the extracting of Ag atoms through a S–Ag coordination bond. When the concentration of DDT is lower, the direct contact between Ag atoms and Ge^{2+} ions is limited to the surface of the Ag NPs because of the immobility of the inner Ag atoms. The formation of a thin and incomplete layer of Ge on the surface can prevent the inner Ag atoms from reacting with Ge^{2+}. As a result, the small hole serves as the primary site for continuous diffusion of Ge^{2+}, which leads to the formation of small Ge NPs with a single pinhole. Whereas, under a higher concentration, DDT can facilitate the fast removal of Ag atoms, which can subsequently increase the pore size and expansion rate of the Ge NPs and result in the formation of larger porous Ge nanocages.

3.3.5 Ge/Ag Ratio Influence

The GeI_2/Ag NPs molar ratio was gradually decreased from 0.8 to 0.1, while keeping all other parameters the same. Although increasing the GeI_2/Ag ratio higher than the stoichiometric ratio does not affect the quality of hollow Ge NPs, as shown in Figure 3.4 a (GeI_2/Ag ratio = 0.8) and 3.4b (GeI_2/Ag ratio = 0.6), decreasing the GeI_2 content below the stoichiometric ratio does significantly change the final products. When the molar ratio of GeI_2/Ag was further lowered to 0.4, as shown in Figure 3.4 c, a mixture of hollow Ge NPs and solid Ge NPs co-exist. When the molar ratio was further decreased to 0.3, as indicated in Figure 3.4 d, the products were mainly composed of highly monodisperse amorphous Ge NPs with no holes. A low-magnification image shown in Figure 3.4 e indicates the uniform size distribution of the solid Ge NP sample synthesized from a GeI_2/Ag ratio of 0.3. A small amount of unreacted Ag contents is also shown with a brighter intensity in the HAADF-STEM image because of the much higher atomic number of Ag (Z-contrast images). The accompanying EDS spectrum and elemental mapping shown in Figure 3.4 g–i confirmed the existence of a small amount of unreacted Ag, because of the slight excess of Ag content. This indicates that the reaction did not follow the fast hollowing-out pathway described above even at a high temperature (T = 200 °C). Therefore, the formation of solid Ge NPs must be through some other mechanism which is controlled by the molar ratio between the GeI_2 precursor and Ag NPs. On the other hand, further lowering of the GeI_2/Ag ratio leads to the formation of irregular Ge NPs (GeI_2/Ag ratio = 0.2) and Ge nanorods (GeI_2/Ag ratio = 0.1); in those cases, agglomeration of excess Ag NPs were also found.

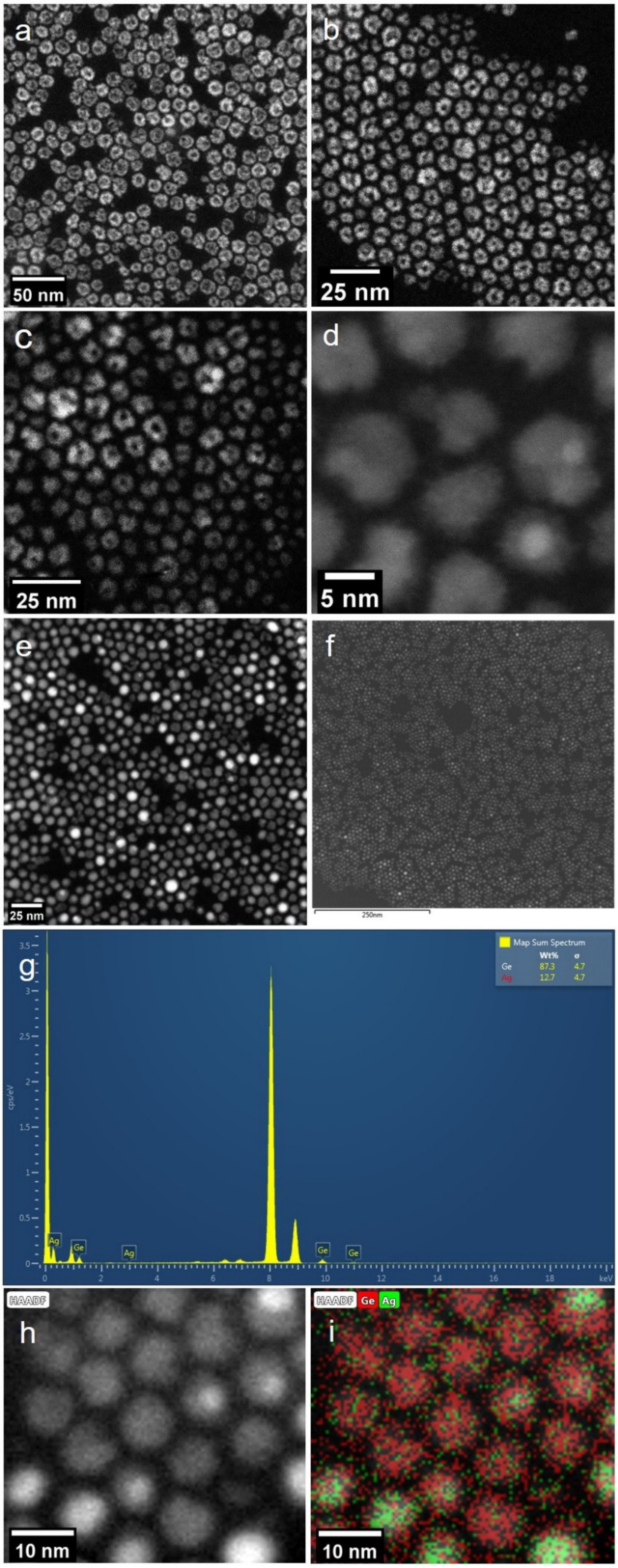
a
50 nm
b
25 nm
c
25 nm
d
5 nm
e
25 nm
f
250nm
g
Map Sum Spectrum
Wt% σ
Ge 87.3 4.7
Ag 12.7 4.7
cps/eV
Ag
Ge
Ag
Ge
Ge
keV
HAADF
h
10 nm
HAADF Ge Ag
i
10 nm

Figure 3.4. (a–d) HAADF-STEM images of Ge NPs synthesized from the same batch of Ag NPs via galvanic replacement reaction with the variation of GeI_2/Ag molar ratio of (a) 0.8, (b) 0.6, (c) 0.4, (d) 0.3. (e) Low-magnification image from the sample in 3.4d. (f) EDS survey image from the sample in 3.4e. (g) EDS spectrum taken from the whole area in Figure 3.4 f. (h–i) HAADF-STEM images from Figure 3.4 e and EDS mapping confirmed that the bright spots are attributed to unreacted Ag.

To further understand the reaction mechanism, the molar ratio of GeI_2/Ag was held constant at 0.3 while decreasing the reaction time to 10 min and quenching the reaction in an ice-water bath. Figure 3.5 a, b represents the resulting bright field (BF) and dark field (DF) STEM images, which show the expected Ag@Ge core–shell intermediate structure. From the BF-STEM image, we can clearly see the lattice fringes from the Ag core, which indicates the original polycrystallinity feature of the Ag NPs. From the HAADF-STEM image, the different stages of the galvanic replacement reaction can be easily identified by marking a single particle with a red dashed circle. Site #1 shows the unreacted Ag NP and site #2 shows an Ag–Ge dimer which indicates that the Ag NP was partially reduced by the Ge precursor which deposits the Ge atoms onto the adjacent domain. Site #3 indicates an Ag@Ge core–shell structure at a later stage of the replacement reaction. The Ag core shrinks to a very small size, indicating that the Ag NP is almost fully reduced by the Ge precursor. Notice that there is no obvious void space formed between the Ag core and Ge shell. Site #4 represents a pure Ge NP without any Ag content. The corresponding EDS spectrum shown in Figure 3.5 c reveals a much lower Ge/Ag ratio in the sample compared to Figure 3.4 g, which indicates that an intermediate product is formed by shortening the reaction time.

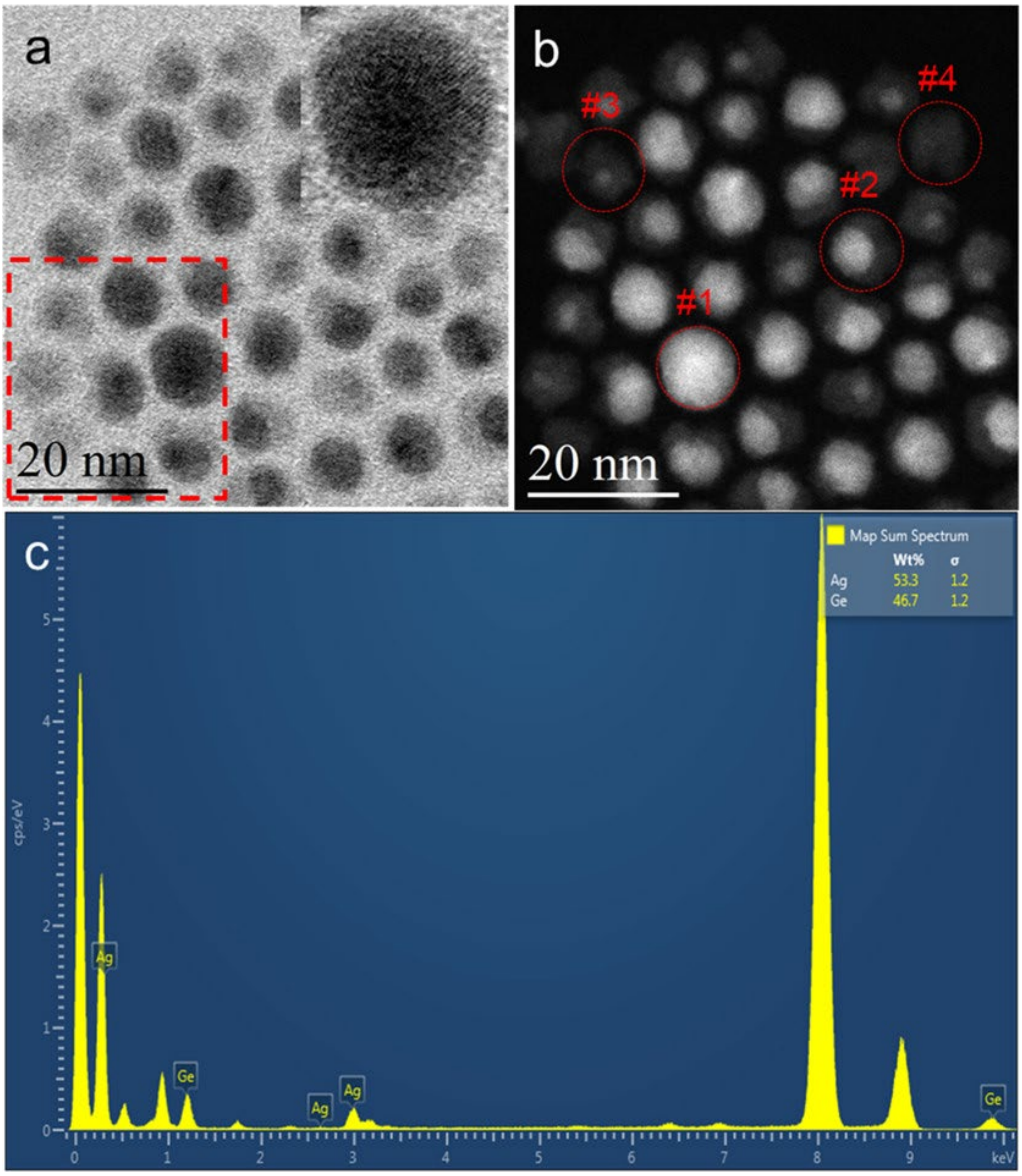

Figure 3.5. (a) BF-STEM image of the as-synthesized Ge NPs according to a GeI_2/Ag molar ratio equal to 0.3. The reaction was quenched after 10 min with an ice-water bath and washed three times. The image shows a mixture of Ag NPs, solid Ge NPs, and Ag@Ge core–shell NPs with different Ge thickness. The top-right corner insert shows a HR-STEM image of (a), the unreacted silver is highly polycrystalline. (b) Corresponding HAADF-STEM image of (a), elemental composition can easily be distinguished by the brightness because of the difference in Z-contrast. The darker spot consists of Ge and much brighter spots are Ag. Particles at different stages of formation are marked with red dashed circles. Site #1 shows unreacted Ag NP and site #2 shows an Ag/Ge dimer structure. Site #3 shows an Ag@Ge core–shell structure with a small Ag core and site #4 shows a pure solid Ge NP. (c) EDS spectrum taken from the whole area in Figure 3.5 b.

With all the above information, we can propose a reaction mechanism to form completely amorphous solid Ge NPs. At an early stage, with significantly lower concentration of Ag NPs (0.3 vs 0.5, which is the stoichiometric molar ratio between GeI_2 and Ag), a thin layer of amorphous Ge is first deposited on the surface of the Ag NP without formation of any pinholes. So, the further galvanic replacement is happening under interdiffusion through the thin Ge atomic layer. Because of the high lattice mismatch between the Ag and Ge and the larger size of Ag^+ compared to Ge^{2+}, along with the low concentration of Ag content, the inward diffusion rate of Ge^{2+} is faster than the outward diffusion rate of Ag^+. Thus, the reduced Ge atoms will occupy mainly the inner space of the particle. However, because of the stoichiometric relationship between the Ag and Ge^{2+}, more Ag atoms are oxidized than Ge atoms reduced, and the overall size of the particle will continue to shrink until all the Ag core has been oxidized, leaving a solid Ge NP as the final product. This hypothesis also explains the average size of the solid Ge NPs being smaller than the original Ag template.

In a typical galvanic replacement reaction, an internal void space will be generated in the final products. This can be explained from both stoichiometric and geometric arguments. First, as the metal ions in the solution phase have been reduced at the surface of the sacrificial template and are growing outward, the metal will be oxidized and extracted from the inner core. This process generates small holes and vacancies in the resulting nanostructures. In addition, the void size also depends on the stoichiometric ratio between the metal ions and the sacrificial template. For example, Xia et al.[32] did a comparative study of galvanic replacement reactions involving Ag nanocubes and $(AuCl_2)^-$ or $(AuCl_4)^-$. By substituting the gold precursor from $(AuCl_4)^-$ to $(AuCl_2)^-$, the stoichiometry between Ag and gold is changed owing to the difference in the oxidation state of the gold. The author reported that both Au precursors can form hollow nanostructures. However, the vacancy space formed at a different rate and only in case of $(AuCl_4)^-$ does the pinhole last throughout the reaction. In the example of $(AuCl_2)^-$, every Ag exchanges one Au atom. However, in the case of $(AuCl_4)^-$, every 3 Ag atoms need to be oxidized to generate enough electrons to reduce the Au ion. This difference in electrochemical reaction impacts the alloying/dealloying processes. Generally, with a higher oxidation state, a larger void space will be generated because of the faster extraction of the metal template. In our reaction, the deposition of each Ge atom would need to consume two Ag atoms inside, which helps the formation of an inner void space. Thus, it is reasonable to assume that the hollowing-out process is dominated by the nanoscale Kirkendall effect, which arises from the difference of the interdiffusion rate between two materials.[33]

Tang and Ouyang reported the formation of Ag_2Se hollow nanocrystals through the reaction of selenium with both single crystalline and multiply twinned (MT) Ag NPs.[34] By contacting with selenium on the surface, the single-crystal Ag NPs transform to Ag_2Se hollow nanocrystals through the Kirkendall effect, whereas the MT Ag NPs give solid, homogeneous Ag_2Se nanocrystals. The author reasoned that, the diffusion of silver atoms is faster than that of selenium atoms, which leads to the void space formation and further condensed into a single hole. However, the multiple twinned structure can provide another fast atom diffusion path through the twining boundaries for both silver and selenium atoms, thus creating solid, homogeneous Ag_2Se nanocrystals. A similar explanation concerning the formation of solid amorphous Ge NPs is highly likely. As the Ag template was an unambiguously MT structure, it could provide an extra diffusion path through the defects, thus counter-balancing the stoichiometric relationship between the Ag and Ge^{2+}, which implies a lower diffusion rate of Ag^+ and a higher diffusion rate of Ge^{2+}. The overall reaction would deposit Ge inward toward the core instead of outward, leading to the formation of solid Ge NPs. The systematic study of the GeI_2/Ag ratio influence also indicates that there is a threshold at around 0.3 where exclusively solid Ge NPs are formed.

The resulting solid Ge NPs are monodisperse owing to the uniform Ag NPs template and the unique reaction pathway. As shown in Figure 3.6, repeating the synthesis under similar conditions but with a longer reaction time results in a monodisperse Ge NP sample, which shows that the reaction is highly reproducible. By counting a total number of 1958 Ge NPs, the particle's mean diameter is around 5.17 nm with less than 0.2% discrepancy between the two different fields of view and a standard deviation of around 10%. The stoichiometric ratio between Ag and Ge precisely controls the inward diffusion pathway, which means regardless of its heterogeneous deposition rate, if the Ag template is completely oxidized, the galvanic replacement reaction would stop immediately because of the lack of any reducing agent present in the solution. This mechanism bypasses the classic nucleation—growth synthesis route but employs Ag NPs as both reducing agents and nucleation sites. Thus, the reaction can be confined within the single NP range, which shows a great potential in future scale-up and industrial applications. The size of the resulting NPs is solely dependent on the initial size of the single metal NP and the reaction stoichiometric relationship.

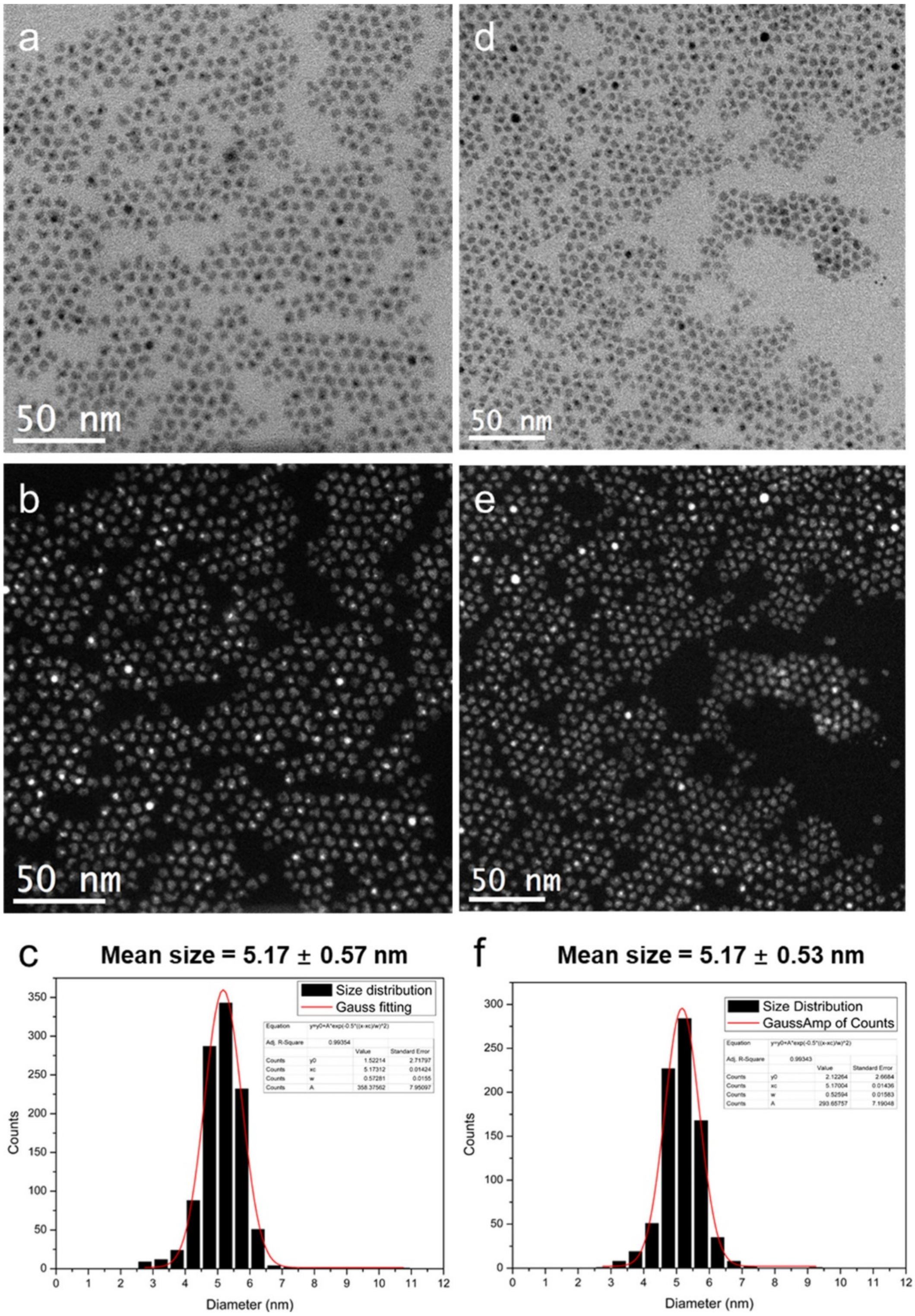

Equation	y=y0+A*exp(-0.5*((x-xc)/w)^2)		
Adj. R-Square	0.99354		
		Value	Standard Error
Counts	y0	1.52214	2.71797
Counts	xc	5.17312	0.01424
Counts	w	0.57281	0.0155
Counts	A	358.37562	7.95097

Equation	y=y0+A*exp(-0.5*((x-xc)/w)^2)		
Adj. R-Square	0.99343		
		Value	Standard Error
Counts	y0	2.12264	2.6684
Counts	xc	5.17004	0.01436
Counts	w	0.52594	0.01583
Counts	A	293.65757	7.19048

Figure 3.6. (a–c) BF-STEM and DF-STEM images of the sample prepared from Ag/GeI_2 = 0.3, the histogram shows a mean size of 5.17 ± 0.57 nm. (d–f) BF-STEM and DF-STEM images of the same sample but from different observing areas. The histogram shows a mean size of 5.17 ± 0.53 nm.

Whereas the galvanic replacement reaction between the noble metals such as Au, Ag, Pt has been studied extensively, there is a contradictory observation of the reaction dynamic via galvanic replacement reaction from different groups. For example, most of the studies agreed with the alloying and dealloying process, and the resulting NPs possess a hollow interior with a smooth surface.[16,19,35–37] However, some groups report a number of different observations suggesting different mechanisms, especially when the galvanic replacement was performed under an organic environment.[22,23] For example, Yang et al.[38] pointed out that they observed a significant shrinkage of the Ag templates during the reaction instead of enlargement in size; they also determined that under certain conditions, the Au or Pt atoms deposited on the surface of the Ag NPs, resulting in a core–shell Ag@Au or Ag@Pt structure without the alloying and dealloying process. Our study suggests that this inconsistency may arise from a slight difference of their synthetic conditions, especially the molar ratio between the starting materials. It shows the importance of understanding the role of each component and their contribution to the structure evolution, which in turn will certainly help to increase the reproducibility and future applications.

3.3.6 Temperature Influence

Whereas our studies were mainly performed at 200 °C employing microwave synthesis to make the reaction's external conditions consistent, the results, however, clearly show that the reaction is both thermodynamically and kinetically controlled. Thus, the study of the heating profile on the reaction is important. Based on the results described above, we can suggest that a lower energy will favor the Ag@Ge core–shell formation pathway, whereas a higher energy will favor the hollowing-out pathway. While keeping all other parameters within an optimal range, a series of studies were performed under different temperature settings. The results are in good agreement with our expectation. As shown in Figure 3.7 a–c, the reaction was barely initiated at a lower temperature. After 30 min of heating at 50 °C, Figure 3.7 a shows mainly unreacted Ag NPs; when the temperature is increased to 70 °C, the products show some etching effect of the Ag template but still no well-defined hollow Ge NPs, as shown in Figure 3.7 b. However, when the temperature is further increased to 100 °C, within 30 min, the STEM image in Figure 3.7 c shows a combination of silver NPs, solid Ge NPs, and hollow Ge NPs. This indicates that the temperature has reached the necessary activation energy to trigger the hollowing-out pathway but not high enough to avoid the Ag@Ge core–shell formation. For comparison purposes, the reaction was performed at 200 °C again to test the robustness of the synthetic conditions. From Figure 3.7 d, the STEM image indicates an exclusively cubic-like hollow Ge NPs, which means under such temperature, the dissolution rate of the Ag core is high enough that the reaction follows only the hollowing-out pathway and results in only hollow Ge NPs.

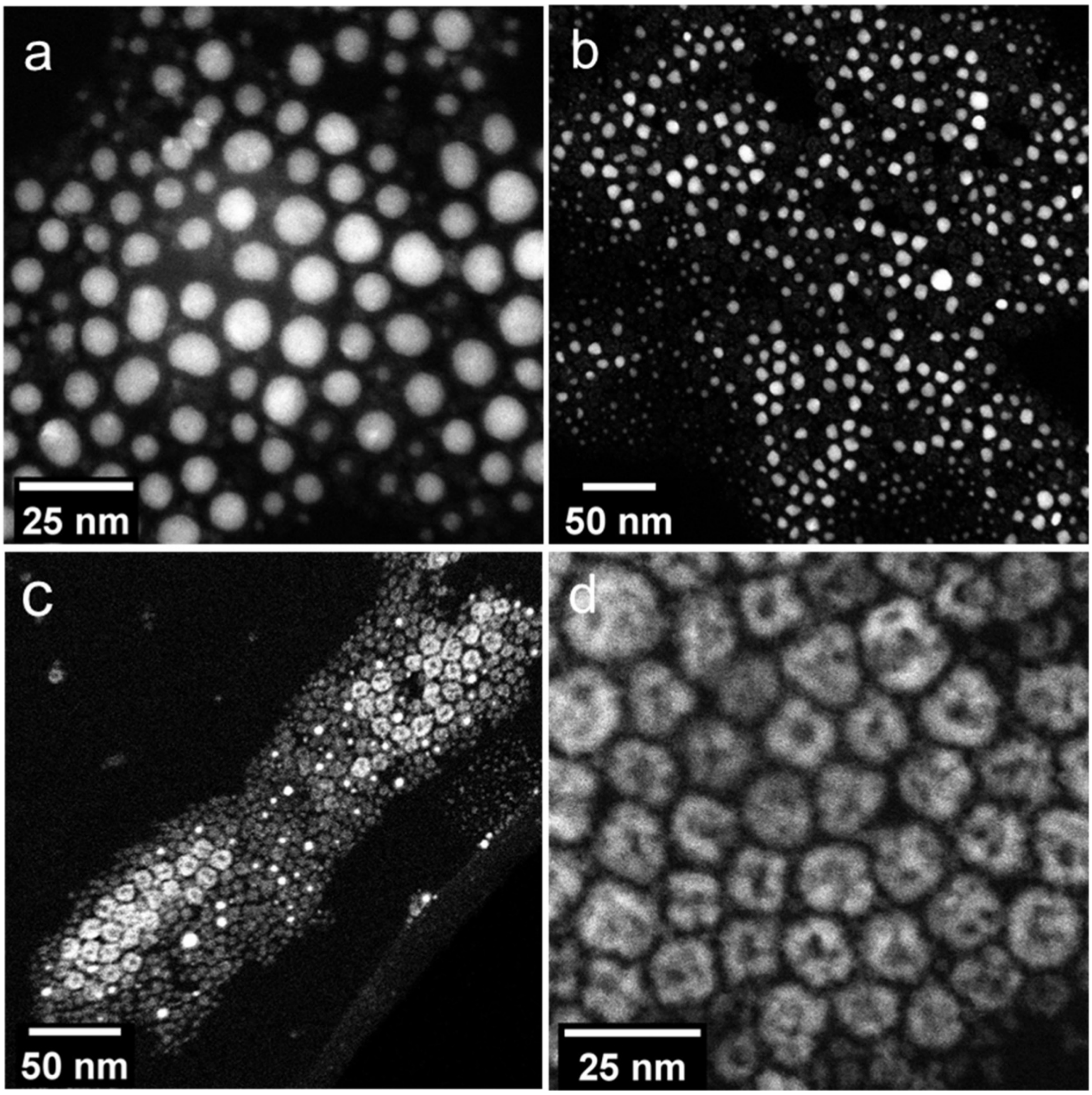

Figure 3.7. (a–c) HAADF-STEM image of the products from galvanic replacement reaction between GeI_2 and Ag NPs under different temperatures: (a) 50, (b) 70, (c) 100, (d) 200 °C. It shows that (a) at 50 °C, the Ag template barely reacted with the Ge precursor and remains intact with a slight change of its original size. (b) When the temperature rises to 70 °C, a combination of Ag@Ge core–shell structure and solid Ge NPs were synthesized. There was no evidence of hollow Ge NPs under this condition. (c) Further increasing the temperature to 100 °C generates both hollow and solid Ge NPs and a small amount of Ag@Ge core–shell structure, which is indicated by the much brighter spot. (d) Exclusively cubic-like hollow Ge structures via galvanic replacement at 200 °C with an optimized synthesis condition.

3.4 Conclusions

We have carried out systematic studies and identified the specific roles of each reagent in the galvanic replacement reaction between GeI_2 and silver NPs. We have also explored the influence of different synthetic parameters such as temperature and reaction time on the reaction. In summary, our results provide new fundamental insights on the reaction mechanism of galvanic replacement reaction between a metal template and non-metal semiconductor ion (e.g., Ge^{2+}) in organic solvent. The results are summarized in Figure 3.8:

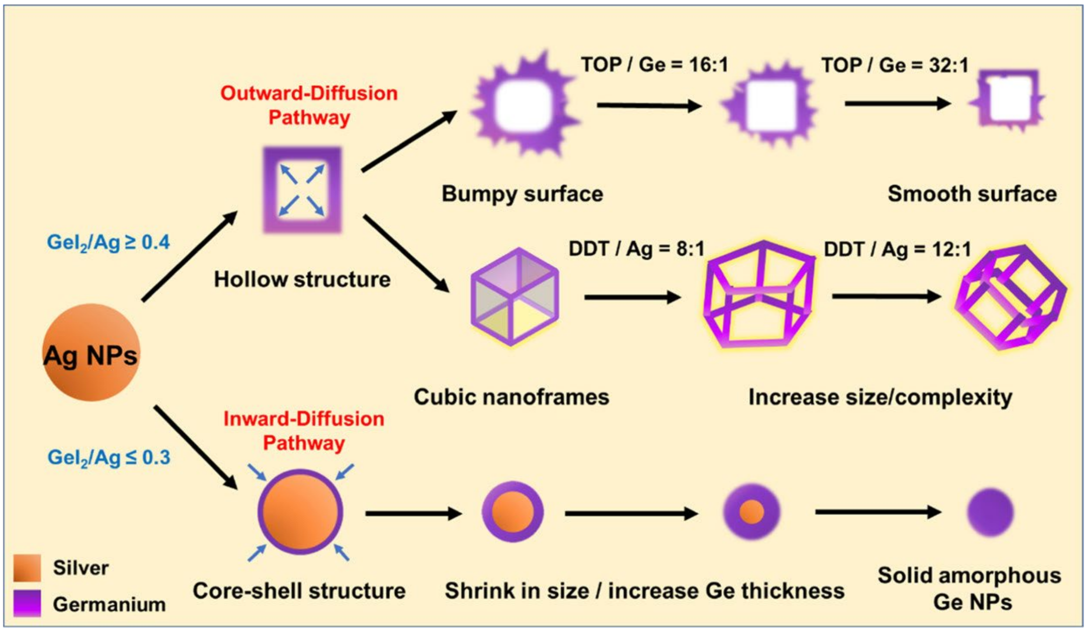

Figure 3.8. Schematic illustration summarizing competitive two different diffusion pathways and structural changes involved in the galvanic replacement reaction between a polycrystalline silver NP and GeI_2. The binding ligand TOP and DDT can also induce a morphological change on the final Ge NPs.

Our systematic study reveals the specific roles of important ligands including TOP and DDT in the galvanic replacement reaction between GeI_2 and Ag NPs. TOP is serving as a stabilizing agent of the inorganic GeI_2 precursor to make it easily dissolve in nonaqueous solutions which ensures the effective contacting between the Ag template and Ge^{2+} ions. A higher concentration of TOP leads to a much smoother surface of the hollow Ge NPs, whereas a lower TOP content results in hollow Ge NPs with more dangling bonds and a bumpy surface. DDT, on the other hand, was found to be critical to the geometry evolution of the hollow Ge NPs. With a higher concentration of DDT, more vacancies will be generated on the surface of the particles, leading to the formation of larger and more complex hollow Ge NPs with multiple porous walls.

In addition, the initial molar ratio between Ag NPs and GeI_2 plays a key role in determining the morphology and composition of the final products. On the Ge-deficient range, the formation of a hollow structure can be prohibited even under a high temperature (e.g., 200 °C). When the concentration of the Ge precursor is efficiently lower than the 0.5 Ge/Ag stoichiometric molar ratio (e.g., Ge/Ag = 0.3), the Ag–Ge diffusion rate is significantly decreased and follows the inward diffusion pathway, which leads to the formation of pure solid Ge NPs with reduced size compared to the Ag templates. On the other hand, only a higher germanium precursor present in the synthesis (e.g., Ge/Ag > 0.4) leads to the formation of a hollow nanostructure. The colloidal Ge NPs are stable under a noble gas condition. When the NPs are suspended in anhydrous toluene and stored in an argon-filled glovebox, the morphology of the hollow Ge NPs and the Ag/Ge domains in the core–shell NPs can be maintained without any changes even after 1 year.

To the best of our knowledge, our study demonstrates the first successful synthesis of a metal–semiconductor core–shell structure with a controllable core and shell thickness via galvanic replacement alone, considering the huge lattice mismatch between Ag and Ge (38.7%). The core/shell thickness ratio could be controlled by selectively quenching the reaction at different stages. With a reasonable temperature range, the galvanic replacement reaction can be controlled to follow only the core–shell growth pathway or fast hollowing-out pathway. This result shows that galvanic replacement reaction can serve as a powerful tool to generate novel nanostructures because of its versatile mechanism and flexibility.

Collectively, our study reveals the multiple aspects of the galvanic replacement reaction between Ag and GeI_2. The reaction can follow the outward fast hollowing-out pathway or inward core–shell pathway depending on the synthesis condition. We also disclose the specific role of each binding ligand in the reaction, which can serve as a guideline to design other galvanic replacement reactions in nonaqueous environments. What is more, we report the successful synthesis of monodisperse solid amorphous Ge NPs that follow the inward growth mechanism, for the first time. The unique mechanism allows the reaction to be self-terminated and achieve nanometer-sized accuracy. The galvanic reaction may be applied to other semiconductors and could serve as a powerful alternative to the classic nucleation-growth mechanism and subsequently advance the scale-up and further applications.

3.5 Materials and Methods

3.5.1 Chemicals and Materials

Silver(I) nitrate, $AgNO_3$ (≥ 99.0%, Sigma-Aldrich), was used as received. Phase pure germanium (II) iodide, GeI_2, was purchased from Prof. Richard Blair’s laboratory (University of South Florida). Oleylamine, OAm (> 40%, TCI America), dioctyl ether, DOE (99%, Sigma-

Aldrich), dodecanethiol DDT (98%, Sigma-Aldrich) were degassed at 100 °C under argon flow for 1 h prior to use. Tri-n-octylphosphine, TOP (min. 97%, Strem Chemicals), was used as received. Methanol and toluene were purchased from Fisher Scientific, purified using a solvent purification system, degassed, and stored under inert atmosphere conditions in an argon-filled glove box.

3.5.2 Synthesis of Silver NPs

In an argon-filled glove box, 5 mmol of $AgNO_3$ (0.850 g) was added to 50 mL of OAm in a two-neck round-bottom flask equipped with a stopcock adapter and rubber septum. The flask was connected to a Schlenk line, and the suspension was then heated up to 60 °C. The temperature was maintained until the granular $AgNO_3$ crystals were completely dissolved. The solution was then quickly heated with a ramp ≥ 10 °C min^{-1} to 200 °C for 40 min while under an argon flow. The reaction was initially colorless, but as the $AgNO_3$ was reduced to form OAm stabilized Ag NPs, the reaction turned dark brown. Upon cooling to room temperature, the Ag NPs were washed using a toluene methanol system under argon protection. The mixture was centrifuged at 8500 rpm for 10 min. The supernatant was discarded, and the precipitates were re-dispersed in toluene for further characterization. To prepare the galvanic replacement reaction between Ag and GeI_2, the Ag NP precipitates were directly pumped in the glovebox and re-dispersed in DOE for further use. Unless otherwise stated, the Ag NPs used for the following galvanic replacement reaction come from the same reaction batch to ensure their uniformity.

3.5.3 Controlled Synthesis of Ge NPs

In a typical synthesis, under inert atmosphere conditions, 0.25 mmol GeI_2 (0.0816 g) was sonicated in 4.2 mmol TOP (1.931 mL) until it became a uniform yellowish solution. About 0.5 mmol Ag NPs dispersed in 20.78 mmol (6.234 mL) of DOE were transferred to a 35 mL microwave vessel followed by addition of the GeI_2/TOP solution and 5 mmol (1.2 mL) of DDT. The microwave vessel was sealed with a silicone cap purchased from CEM, transferred to a CEM microwave reactor (Discover SP), and heated to 200 °C in dynamic mode. After heating for 30 min at 200 °C, the reaction was cooled to 60 °C in the reactor chamber by air-blowing and then completely quenched in an ice-water bath. The microwave vessel was covered by a parafilm and pumped into a glove box. The resulting product was washed three times with methanol and toluene (1.8 : 1 by volume) and centrifuged at 8500 rpm for 10 min. The supernatant was discarded each time, and the Ge NPs were dispersed in toluene and stored in a glass vial within the glovebox.

3.5.4 Characterization

HAADF-STEM images of the sample were obtained by using an aberration-corrected JEOL JEM-2100F/Cs STEM operated at 200 kV. The sample was prepared by putting one droplet of toluene dispersion of the as-synthesized NPs on copper grids coated with ultrathin amorphous carbon films (Ted Pella, Inc.). EDS was collected on an Oxford X-MaxN TSR EDS detector attached to the JEOL JEM-2100F to investigate the chemical composition and structural information. TEM data were acquired using an FEI ThemIS 60–300 STEM/TEM (Thermo Fisher Scientific, US) operated at 300 kV at the National Center for Electron Microscopy within the Molecular Foundry in Lawrence Berkeley National Laboratory. The ThemIS is equipped with image aberration corrector optics, and a Ceta2 camera (4k × 4k pixels, and 14-bit dynamic range). EDS mapping was performed using a Bruker Super-X Quad windowless detector with a solid angle of 0.7 sr. The measurement of the optical property was conducted on the toluene dispersion with a Shimadzu UV-3600.

3.6 References

1. Aricò, A. S.; Bruce, P.; Scrosati, B.; Tarascon, J.-M.; van Schalkwijk, W., Nanostructured materials for advanced energy conversion and storage devices. *Nature Materials* **2005,** *4* (5), 366-377.
2. Choi, S.; Kim, J.; Choi, N.-S.; Kim, M. G.; Park, S., Cost-Effective Scalable Synthesis of Mesoporous Germanium Particles via a Redox-Transmetalation Reaction for High-Performance Energy Storage Devices. *ACS Nano* **2015,** *9* (2), 2203-2212.
3. Son, I. H.; Park, J. H.; Park, S.; Park, K.; Han, S.; Shin, J.; Doo, S.-G.; Hwang, Y.; Chang, H.; Choi, J. W., Graphene balls for lithium rechargeable batteries with fast charging and high volumetric energy densities. *Nature Communications* **2017,** *8* (1), 1561.
4. Lu, J.; Wu, T.; Amine, K., State-of-the-art characterization techniques for advanced lithium-ion batteries. *Nature Energy* **2017,** *2* (3), 17011.
5. An, Y.; Fei, H.; Zeng, G.; Xu, X.; Ci, L.; Xi, B.; Xiong, S.; Feng, J.; Qian, Y., Vacuum distillation derived 3D porous current collector for stable lithium–metal batteries. *Nano Energy* **2018,** *47*, 503-511.
6. Tarascon, J. M.; Armand, M., Issues and challenges facing rechargeable lithium batteries.

Nature **2001,** *414* (6861), 359-367.

7. Park, M.-H.; Cho, Y.; Kim, K.; Kim, J.; Liu, M.; Cho, J., Germanium Nanotubes Prepared by Using the Kirkendall Effect as Anodes for High-Rate Lithium Batteries. *Angewandte Chemie International Edition* **2011,** *50* (41), 9647-9650.

8. Li, W.; Li, M.; Yang, Z.; Xu, J.; Zhong, X.; Wang, J.; Zeng, L.; Liu, X.; Jiang, Y.; Wei, X.; Gu, L.; Yu, Y., Carbon-Coated Germanium Nanowires on Carbon Nanofibers as Self-Supported Electrodes for Flexible Lithium-Ion Batteries. *Small* **2015,** *11* (23), 2762-2767.

9. Wu, S.; Han, C.; Iocozzia, J.; Lu, M.; Ge, R.; Xu, R.; Lin, Z., Germanium-Based Nanomaterials for Rechargeable Batteries. *Angew Chem Int Ed Engl* **2016,** *55* (28), 7898-7922.

10. Vaughn Ii, D. D.; Schaak, R. E., Synthesis, properties and applications of colloidal germanium and germanium-based nanomaterials. *Chemical Society Reviews* **2013,** *42* (7), 2861-2879.

11. He, R.; Sazio, P. J. A.; Peacock, A. C.; Healy, N.; Sparks, J. R.; Krishnamurthi, M.; Gopalan, V.; Badding, J. V., Integration of gigahertz-bandwidth semiconductor devices inside microstructured optical fibres. *Nature Photonics* **2012,** *6*, 174.

12. Gärtner, K.; Jöhrens, J.; Steinbach, T.; Schnohr, C. S.; Ridgway, M. C.; Wesch, W., Void formation in amorphous germanium due to high electronic energy deposition. *Physical Review B* **2011,** *83* (22), 224106.

13. Sayed, S. Y.; Buriak, J. M., Epitaxial Growth of Nanostructured Gold Films on Germanium via Galvanic Displacement. *ACS Applied Materials & Interfaces* **2010,** *2* (12), 3515-3524.

14. Oh, M. H.; Yu, T.; Yu, S.-H.; Lim, B.; Ko, K.-T.; Willinger, M.-G.; Seo, D.-H.;

Kim, B. H.; Cho, M. G.; Park, J.-H.; Kang, K.; Sung, Y.-E.; Pinna, N.; Hyeon, T., Galvanic Replacement Reactions in Metal Oxide Nanocrystals. *Science* **2013,** *340* (6135), 964.

15. El Mel, A.-A.; Chettab, M.; Gautron, E.; Chauvin, A.; Humbert, B.; Mevellec, J.-Y.; Delacote, C.; Thiry, D.; Stephant, N.; Ding, J.; Du, K.; Choi, C.-H.; Tessier, P.-Y., Galvanic Replacement Reaction: A Route to Highly Ordered Bimetallic Nanotubes. *The Journal of Physical Chemistry C* **2016,** *120* (31), 17652-17659.

16. Xia, X.; Wang, Y.; Ruditskiy, A.; Xia, Y., 25th Anniversary Article: Galvanic Replacement: A Simple and Versatile Route to Hollow Nanostructures with Tunable and Well-Controlled Properties. *Advanced Materials* **2013,** *25* (44), 6313-6333.

17. González, E.; Arbiol, J.; Puntes, V. F., Carving at the Nanoscale: Sequential Galvanic Exchange and Kirkendall Growth at Room Temperature. *Science* **2011,** *334* (6061), 1377.

18. Sun, Y.; Xia, Y., Shape-Controlled Synthesis of Gold and Silver Nanoparticles. *Science* **2002,** *298* (5601), 2176.

19. Sun, Y.; Xia, Y., Mechanistic Study on the Replacement Reaction between Silver Nanostructures and Chloroauric Acid in Aqueous Medium. *Journal of the American Chemical Society* **2004,** *126* (12), 3892-3901.

20. Lin, Z.-W.; Tsao, Y.-C.; Yang, M.-Y.; Huang, M. H., Seed-Mediated Growth of Silver Nanocubes in Aqueous Solution with Tunable Size and Their Conversion to Au Nanocages with Efficient Photothermal Property. *Chemistry* **2016,** *22* (7), 2326-2332.

21. Wu, Y.; Sun, X.; Yang, Y.; Li, J.; Zhang, Y.; Qin, D., Enriching Silver Nanocrystals with a Second Noble Metal. *Accounts of Chemical Research* **2017,** *50* (7), 1774-1784.

22. Yang, J.; Lee, J. Y.; Ying, J. Y., Phase transfer and its applications in nanotechnology.

Chemical Society Reviews **2011,** *40* (3), 1672-1696.

23. Yang, J.; Lee, J. Y.; Too, H.-P., Core−Shell Ag−Au Nanoparticles from Replacement Reaction in Organic Medium. *The Journal of Physical Chemistry B* **2005,** *109* (41), 19208-19212.

24. Nolan, B. M.; Chan, E. K.; Zhang, X.; Muthuswamy, E.; van Benthem, K.; Kauzlarich, S. M., Sacrificial Silver Nanoparticles: Reducing GeI2 To Form Hollow Germanium Nanoparticles by Electroless Deposition. *ACS Nano* **2016,** *10* (5), 5391-5397.

25. Hiramatsu, H.; Osterloh, F. E., A Simple Large-Scale Synthesis of Nearly Monodisperse Gold and Silver Nanoparticles with Adjustable Sizes and with Exchangeable Surfactants. *Chemistry of Materials* **2004,** *16* (13), 2509-2511.

26. Peng, S.; McMahon, J. M.; Schatz, G. C.; Gray, S. K.; Sun, Y., Reversing the size-dependence of surface plasmon resonances. *Proceedings of the National Academy of Sciences* **2010,** *107* (33), 14530-14534.

27. Sun, Y., Controlled synthesis of colloidal silver nanoparticles in organic solutions: empirical rules for nucleation engineering. *Chemical Society Reviews* **2013,** *42* (7), 2497-2511.

28. Chen, J.; Wiley, B.; McLellan, J.; Xiong, Y.; Li, Z.-Y.; Xia, Y., Optical Properties of Pd−Ag and Pt−Ag Nanoboxes Synthesized via Galvanic Replacement Reactions. *Nano Letters* **2005,** *5* (10), 2058-2062.

29. He, J.; Kanjanaboos, P.; Frazer, N. L.; Weis, A.; Lin, X.-M.; Jaeger Heinrich, M., Fabrication and Mechanical Properties of Large-Scale Freestanding Nanoparticle Membranes. *Small* **2010,** *6* (13), 1449-1456.

30. Lu, X.; Au, L.; McLellan, J.; Li, Z.-Y.; Marquez, M.; Xia, Y., Fabrication of Cubic

Nanocages and Nanoframes by Dealloying Au/Ag Alloy Nanoboxes with an Aqueous Etchant Based on Fe(NO3)3 or NH4OH. *Nano Letters* **2007,** *7* (6), 1764-1769.

31. Zeng, J.; Zhang, Q.; Chen, J.; Xia, Y., A Comparison Study of the Catalytic Properties of Au-Based Nanocages, Nanoboxes, and Nanoparticles. *Nano Letters* **2010,** *10* (1), 30-35.

32. Au, L.; Lu, X.; Xia, Y., A Comparative Study of Galvanic Replacement Reactions Involving Ag Nanocubes and AuCl2− or AuCl4−. *Advanced Materials* **2008,** *20* (13), 2517-2522.

33. Wang, W.; Dahl, M.; Yin, Y., Hollow Nanocrystals through the Nanoscale Kirkendall Effect. *Chemistry of Materials* **2013,** *25* (8), 1179-1189.

34. Tang, Y.; Ouyang, M., Tailoring properties and functionalities of metal nanoparticles through crystallinity engineering. *Nature Materials* **2007,** *6*, 754.

35. Sun, Y.; Mayers, B. T.; Xia, Y., Template-Engaged Replacement Reaction: A One-Step Approach to the Large-Scale Synthesis of Metal Nanostructures with Hollow Interiors. *Nano Letters* **2002,** *2* (5), 481-485.

36. Sun, Y.; Xia, Y., Multiple-Walled Nanotubes Made of Metals. *Advanced Materials* **2004,** *16* (3), 264-268.

37. Tan, S. F.; Lin, G.; Bosman, M.; Mirsaidov, U.; Nijhuis, C. A., Real-Time Dynamics of Galvanic Replacement Reactions of Silver Nanocubes and Au Studied by Liquid-Cell Transmission Electron Microscopy. *ACS Nano* **2016,** *10* (8), 7689-7695.

38. Yang, J.; Yang Lee, J.; Too, H.-P., Phase-Transfer Identification of Core-Shell Structures in Bimetallic Nanoparticles. *Plasmonics* **2006,** *1* (1), 67-78.

Chapter 4

Atomic-Scale *in situ* Observation of Electron Beam and Heat Induced Crystallization of Ge Nanoparticles and Transformation of Ag@Ge Core-Shell Nanocrystals

Chapter 4 is unpublished work. Xiao Qi, Karen C. Bustillo (National Center for Electron Microscopy, Molecular Foundry, Lawrence Berkeley National Laboratory, Berkeley, CA 94720, USA) and Susan M. Kauzlarich. The dissertation author was the primary investigator and author of this material.

4.1 Abstract

Crystallization of amorphous materials by thermal annealing has been studied for many applications in the field of nanotechnology such as thin-film transistors and thermoelectric devices. However, direct visualization of such physical transformation on the nanoscale remains a challenge. Recent studies show that high-energy electron beam irradiation within a Transmission Electron Microscope (TEM) is a powerful tool for the manipulation of nanostructures with precise control due to its high spatial resolution and controllability of the

electron beam. In the present study, the phase transition condition and shape evolution for amorphous solid and hollow Ge NPs and Ag@Ge core-shell nanostructures were investigated. The transition of a single Ge amorphous NP to the crystalline diamond cubic structure at the atomic scale was clearly demonstrated by employing both a 300-kV electron beam and elevated temperature within the TEM. Depending on the heating temperature, the hollow structure can be maintained or transformed into a solid Ge nanocrystal through a diffusive process during the phase transition. Selected area diffraction patterns (SAED) were also obtained associated with the crystallization process. In addition, the thermal stability of Ag@Ge core-shell nanostructures was studied by applying the same beam condition and temperatures. The results show that at a moderate temperature (e.g., 385 °C), the amorphous Ge shell can completely crystallize while maintaining the well-defined core-shell structure, while at a high temperature (e.g., 545 °C), the high thermal energy enables a freely diffusive process of both Ag and Ge atoms on the carbon support film and leads to a transformation into a phase segregated Ag-Ge Janus nanoparticle, with a clear interface between the Ag and Ge domains. The study provides a protocol as well as insight into the thermal stability and strain relief mechanism of complex nanostructures at the single nanoparticle level with atomic resolution and can be further applied to other materials.

4.2 Introduction

The properties of nanocrystals are highly dependent on their composition, structure, and morphology. Tailored synthesis with control of these parameters can be successfully applied to produce nanocrystals with desired properties for specific applications. Ge nanoparticles

(NPs) have excited scientists and engineers because of the unique properties of high carrier mobility and large exciton Bohr radius enabling fabrication of high-performance devices including plasmonic,[1] photodetectors,[2-4] multi-junction solar cells,[5, 6] and lithium-ion batteries.[7-9] Recently, metal-semiconductor heterostructures have drawn significant attention because of their great advantages for fabricating nano-optoelectronic devices.[10] Different metals have been investigated as diffusion sources in Ge such as Ni,[11] Pt,[12] Cu,[13] and Au[14] for high electrical conduction or Co,[15] Fe,[16] and Mn[17] for magnetic applications. However, most studies are focusing on the fabrication of 1D heterostructures based on Ge nanowires because of the lack of synthetic methods for high quality Ge quantum dots structures. Moreover, radial metal-semiconductor heterostructures are typically unstable due to the strain induced by the large lattice mismatch. Such 0D metal-semiconductor heterostructures are rarely reported in the literature.

We recently reported the synthesis of Ag@Ge metal-semiconductor core-shell heterostructures with highly controllable shell thickness via an unconventional galvanic replacement reaction.[18] Considering the different atomic radii and large lattice mismatch (38.7%), strain is significant at the Ag@Ge core-shell interface. Thus, investigating the thermal stability and strain relief mechanism of such 0D metal-semiconductor heterostructure is vital to understand their formation mechanism, optimize the synthesis condition, and prevent mechanical failure in the industrial applications.

Consecutive heating via rapid thermal annealing is a common technique to study the thermal stability of nanomaterials. A traditional approach includes heating the NP powder in a tube furnace or heating mantle followed by characterization using XRD to study the phase transformation condition. However, due to the high surface energy, the phase transition temperature is highly dependent on the size and morphology of the NPs, which makes a precise determination of phase transition temperature for specific nanostructures extremely challenging. For example, crystallization of amorphous Ge NPs was previously investigated by thermal annealing and characterized by in situ X-ray diffraction (XRD),[19] the phase transition was found to occur between 550 and 600 °C. In another example, in situ TEM was used to investigate the effect of heating on an organo-Ge polymer/nanoparticle composite material containing alkyl-terminated Ge nanoparticles.[20] The author found that, when the temperature is above 480 °C, melting of small Ge NPs (2-3 nm) is observed, while NPs greater than 5 nm remain crystalline. Thermal stability of a metal/semiconductor interface was also studied by many groups. For example, platinum (Pt) thermal diffusion into a silicon (Si) nanowire to create a Pt-Si contact has been previously reported.[21] However, such a diffusion process is typically not easy to be reproduced since the diffusive process is highly dependent on the homogeneity and quality of the nanowires.[22]

Compared to the traditional methods discussed above, direct Joule heating, first reported in the work of Mongillo et al.,[23] is a promising technique allows heating while observing the diffusion process in the electron microscope using an in situ TEM sample holder. Since the NPs are permanently fixed on the supporting carbon film of TEM grid, it is possible to observe the phase transition process of a single nanoparticle at high resolution. Moreover, because the Ge NPs are well separated from each other by their surface ligands and the packing density can be easily controlled by the concentration of NP dispersion, mutual diffusion and dispersion between the adjacent nanoparticles can be easily prohibited, thus the all-solid-state interface diffusion process as well as the accompanying morphological changes can be better studied.

Herein, we present real-time observations of the dynamic crystallization process for both hollow and solid amorphous Ge NPs through a combination of joule heating and high-energy electron beam irradiation by in situ TEM. By applying the same approach, the thermal stability and structural evolution of the Ag@Ge core-shell nanostructure were revealed at atomic level. Due to their small size, well-defined structure, and composition, the chosen system is ideally suited for the investigation of atomistic dynamics driven by external stimulus and of processes related to diffusion, reconstruction, and interface modification. By combining real-time structural imaging with elemental analysis, we can follow the transformation process, which occurs through crystallization of the amorphous Ge shell and is accompanied by surface segregation of Ag. The direct observation of atomistic dynamics during thermal-treatment-induced structural modification will help to understand more complex transformations in other metal-semiconductor heterostructures and applications.

4.3 Results and Discussion

4.3.1 Synthesis of Amorphous Ge NPs and Ag@Ge Core-shell NPs

Solid and hollow Ge NPs are synthesized by a previously reported method.[18] Figure 4.1 shows the HAADF-STEM images of the as-synthesized Ge NPs, which are both amorphous. Core-shell nanostructure via electrical displacement was rarely reported in literature due to the low energy barrier.[24-28] The extremely fast reaction rate and the lack of effective methods to quench the reaction leads to the inevitably formation of hollow structure even at temperatures close to 0 °C. While many synthetic strategies have been applied to control the reaction rate, such as introducing a competitive reducing agent or substituting the metal precursor,[29-32], the galvanic replacement reaction between Ag and GeI_2 is proved to be highly controllable because of the relatively high energy barrier compared to the other galvanic replacement reaction in aqueous solution. Since heating is necessary for the reaction to proceed, the fast hollowing-out process can be prevented by just lowering the temperature, and Ag@Ge core-shell structure is successfully synthesized by the galvanic replacement at 150 °C for 15 min followed by directly injecting into an ice-cold methanol solution to immediately quench the reaction.

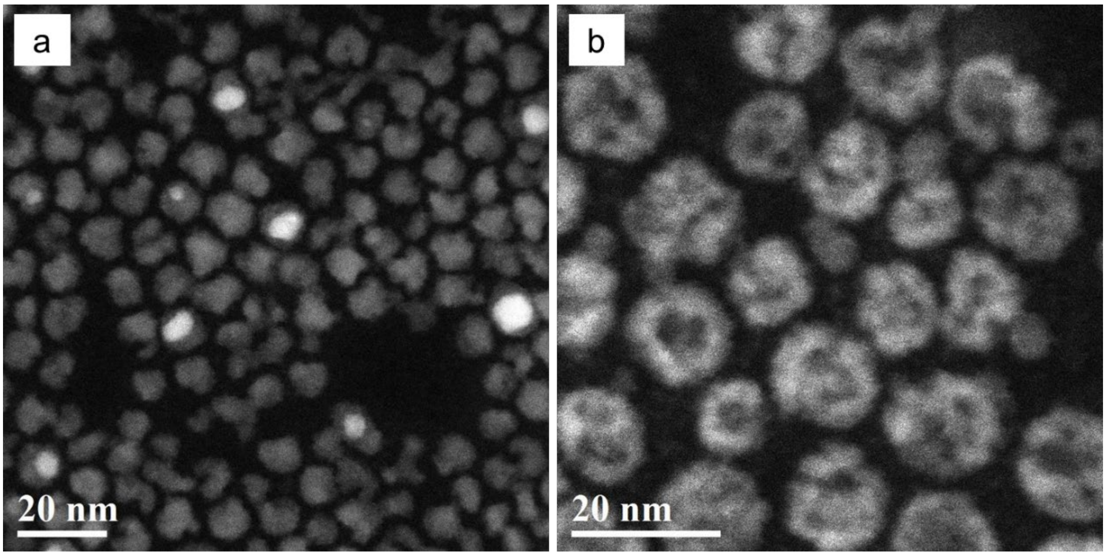

Figure 4.1. HAADF-STEM images of the solid (a) and hollow (b) Ge NPs

4.3.2 Structural and Compositional Characterizations of Ag@Ge Core-shell Nanoparticles.

The TEM image of a typical Ag@Ge core-shell NCs is shown in Figure 4.2a. However, due to the phase contrast nature of TEM mode, the Ge shell is hard to see at higher magnification, as shown in Figure 4.2b. The Ag core is a multi-twined single crystal with 5-fold symmetry. The annular bright-field and simultaneously recorded HAADF-STEM images reveal that the NCs have a well-defined core‒shell configuration with a distinct imaging contrast (Figure 4.3a, b). The high brightness of the core is due to the strong scattering of the crystalline Ag and the Ge shell has a much weaker contrast due to weaker scattering from its amorphous structure. To characterize the composition and elemental distribution of the NCs, we carried out detailed analysis by EDS. As shown from the elemental maps (Figure 4.4), the core area of the NC mainly shows the signal of Ag, in line with the structural analysis. In contrast, the shells are mainly composed from Ge. It is also worth mentioning that, in addition to Ge, the shell is likely to contain traces of C and O, considering its amorphous state and the synthetic conditions.

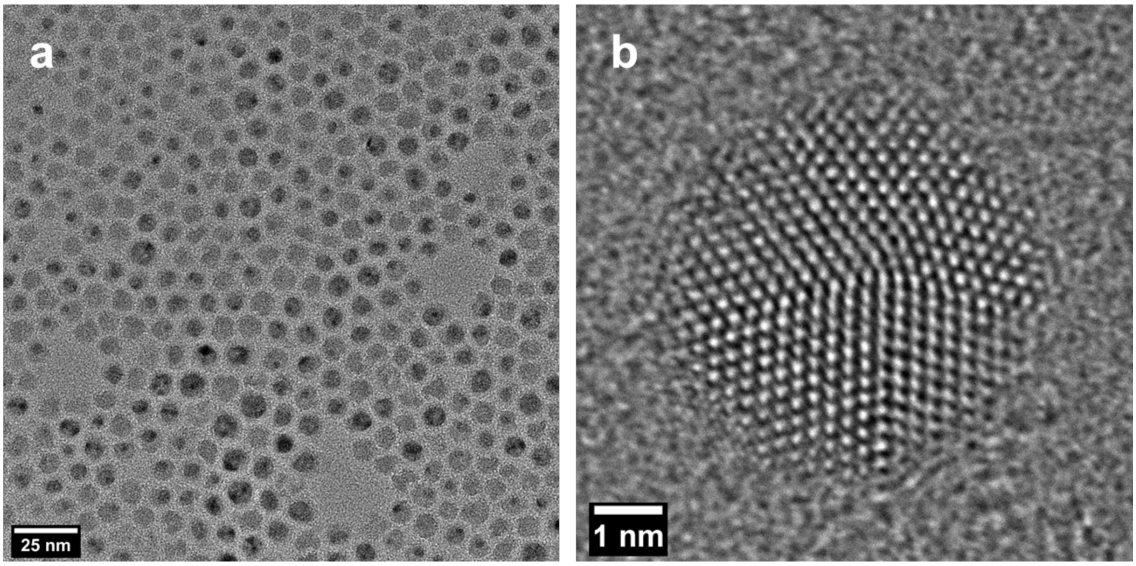

Figure 4.2. (a) TEM image of Ag@Ge core-shell nanocrystals. (b) High-resolution TEM image of a single Ag@Ge core-shell nanostructure. Only the Ag core is clearly imaged with 5-fold symmetry and the amorphous Ge shell is barely visible due to phase contrast.

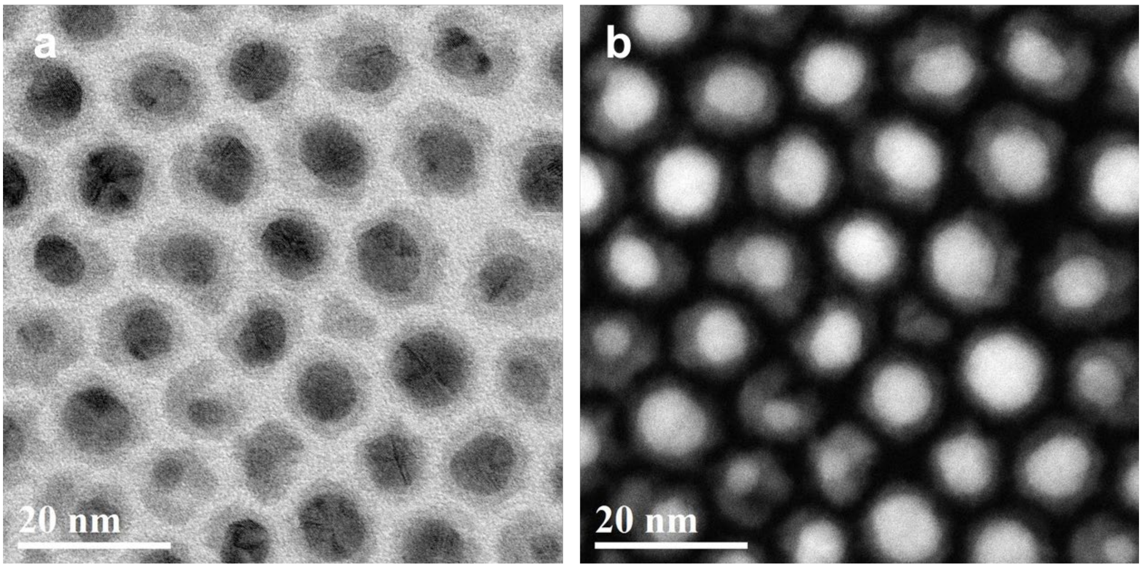

Figure 4.3. ABF-STEM and corresponding HAADF-STEM images of Ag@Ge core−shell nanocrystals.

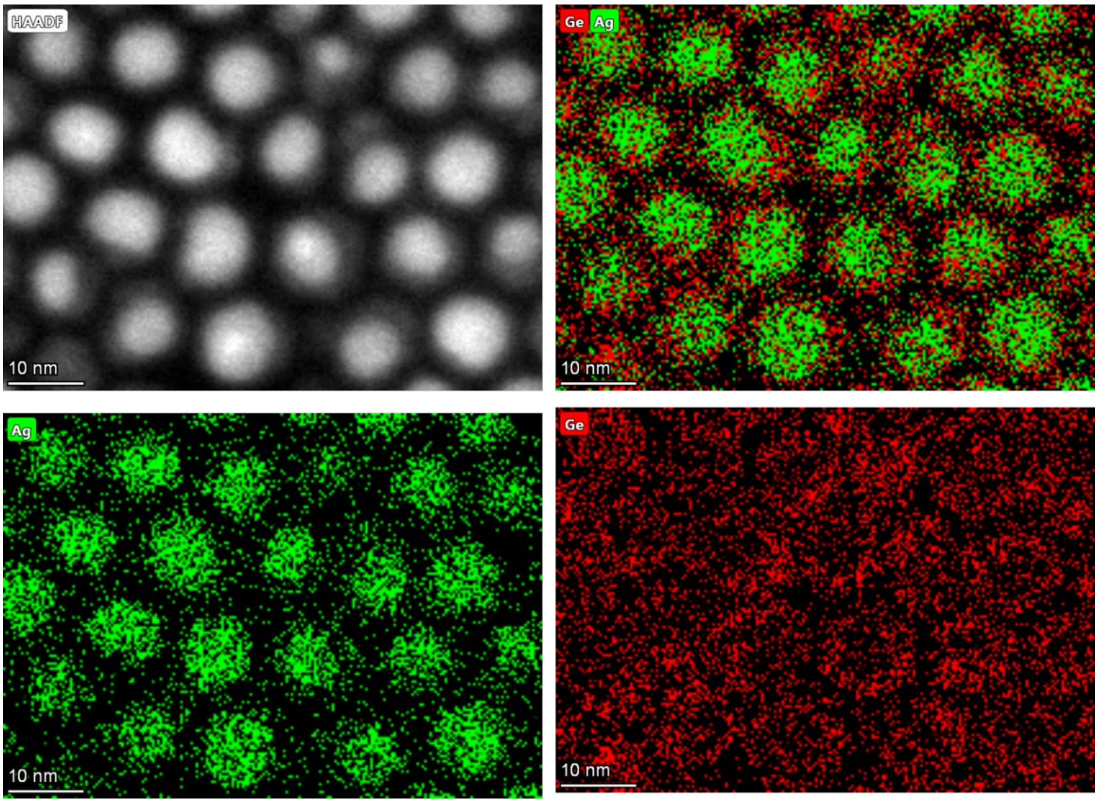

Figure 4.4. HAADF-STEM image and corresponding elemental maps of Ag and Ge.

4.3.3 In situ Observation of the Crystallization of Amorphous Solid Ge NPs

The crystallization of amorphous Ge NPs was observed through in situ TEM experiments with an annealing process, aimed at mapping out the structural evolution in the entire crystallization process and investigating the phase change temperature. Convincing imaging of the Ge NPs using TEM mode is challenging because the focus of the microscope inevitably changes due to the thermal vibration and deflection of the sample grid during the in situ heating process. As a result, resolution is deteriorated due to drifting during the image recording. An ultra-fast CCD camera might be able to capture the dynamics during the crystallization without sacrificing the point resolution but inevitably the information will be significantly lost owing to the fast image recording time. As an alternative approach, the specimen is preheated to a certain temperature and then a focused electron beam will induce the crystallization and restructuring of the Ge NPs. Using this approach of using the 300 kV e-beam to both probe and modify the particle, we directly follow how the single amorphous Ge NP crystallizes and thereby explore in situ and at the atomic scale. At room temperature, the Ge NP is completely amorphous, as shown in Figure 4.5. The specimen was gradually heated to 385 °C until it started to show evidence of crystallization, as shown in the first frame in Figure 4.6. Then the temperature was maintained at 385 °C until no thermal vibration of the specimen could be detected. Then the beam was focused to maintain a screen current at 6.24 nA and the dose rate at 1.38 E5 e/Å^{2}s. The complete crystallization of amorphous Ge occurs within 5 min, as shown in Figure 4.6. The top-left corner of the amorphous Ge NP shows some lattice fringes at time 00:00 due to the thermal energy. Then, crystallization nucleates from the existing crystalline site and after 5 min the Ge NP transfers into a single crystal nanoparticle. The initial morphology of the Ge NP is somewhat oval-shaped and after crystallization, it becomes more spherical to minimize the surface energy. Notice that even with maintaining the whole specimen at 385 °C for about 1 h, the other Ge NPs out of the viewing field remain amorphous. This indicates that the phase transformation temperature might be higher than 385 °C, however, the 300 kV electron beam provides the additional energy to induce the crystallization process. After further increase of the temperature to 545 °C, all the amorphous Ge NPs are transformed to crystalline Ge without the help of the electron beam. In addition, selected area electron diffraction (SAED) data were collected during the crystallization process as shown in Figure 4.7, which further confirms the crystallization temperature is above 385 °C.

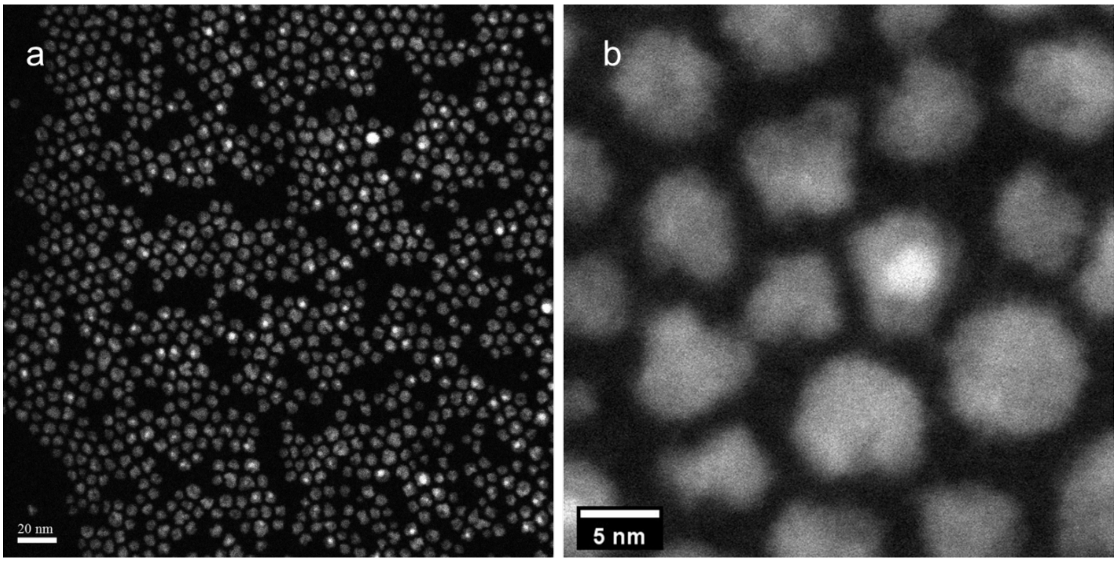

Figure 4.5. HAADF-STEM image of amorphous Ge NPs.

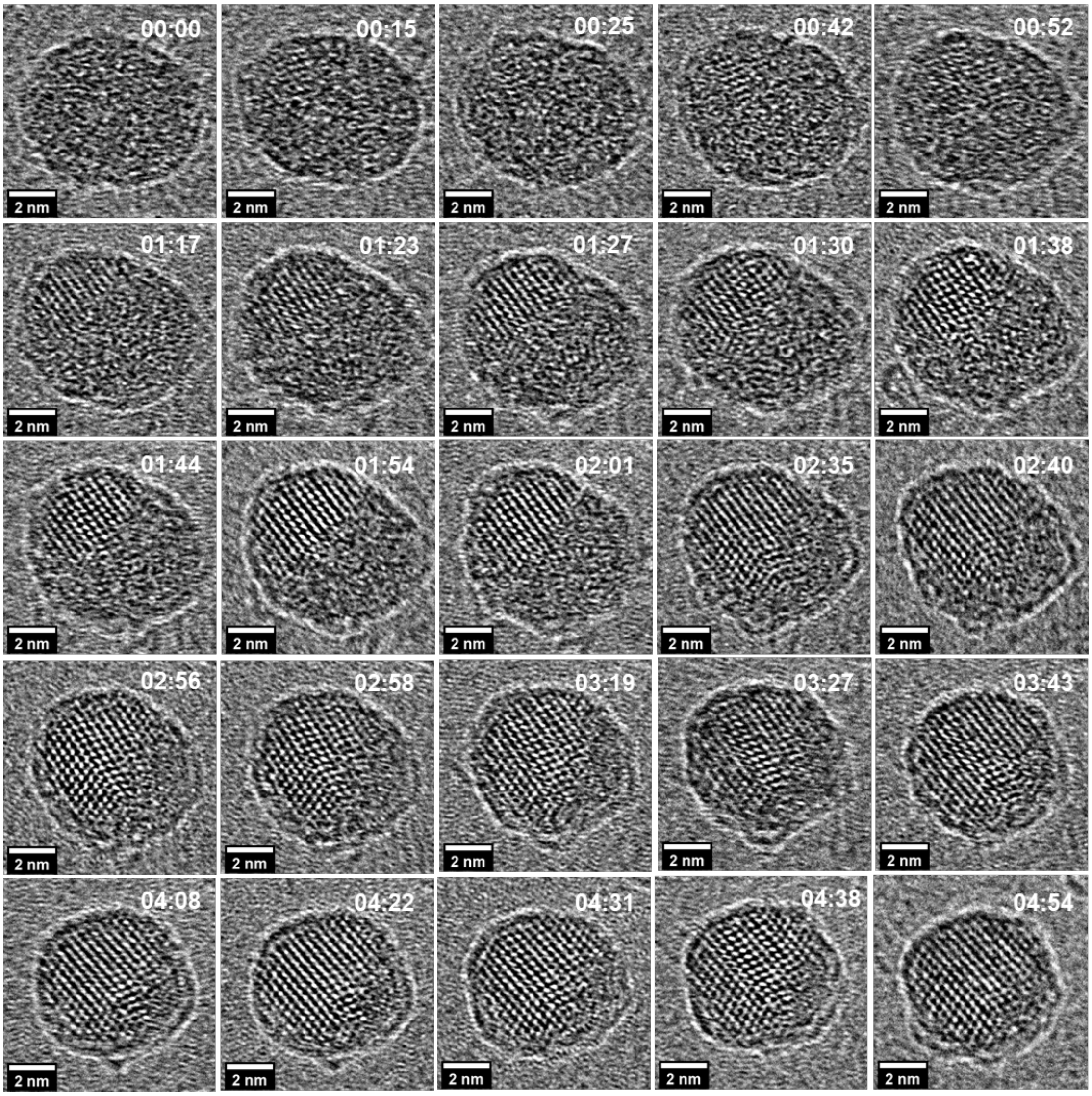

Figure 4.6. In situ observation of crystallization of amorphous solid Ge NP.

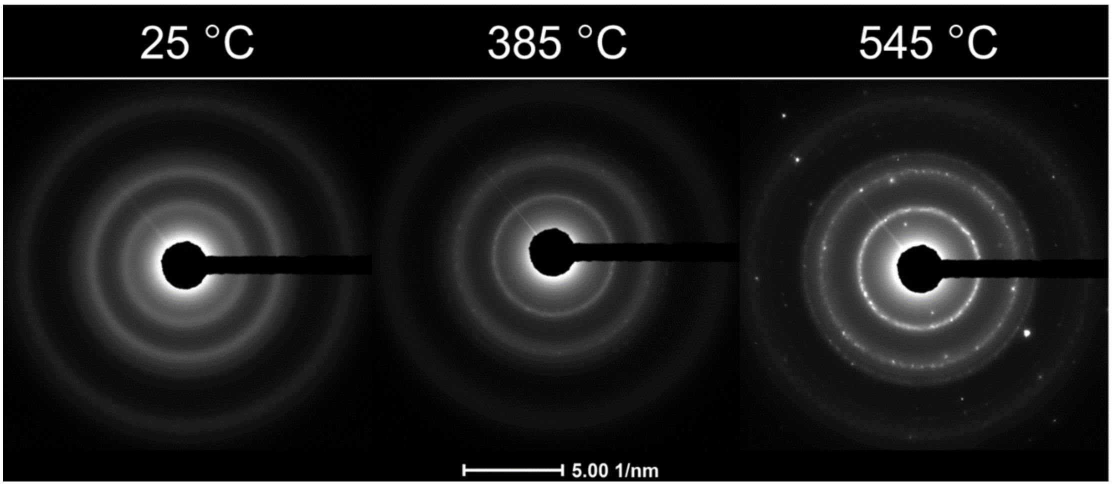

Figure 4.7. Selected area electron diffraction (SAED) pattern of the Ge NPs at (a) 25 °C (b) 385 °C, (c) 545 °C.

4.3.4 In situ Observation of the Crystallization of Amorphous Hollow Ge NPs

The same approach was applied to the amorphous hollow Ge NPs to study the crystallization process. Figure 4.8a shows a typical BF-TEM image of the as synthesized hollow Ge NPs. After the heating starts, the image drifts due to the thermal expansion of the metallic TEM grid in the vacuum chamber, as shown in Figure 4.8b. After the temperature stabilizes at 385 °C for about 1 h, the drift is minimized, and a high-resolution TEM image of the hollow Ge NPs was obtained, as shown in Figure 4.8c. At 385 °C, the hollow Ge NPs start the diffusion process as indicated by the change in morphology of the hollow Ge NPs over time and the Ge NPs attach to each other. However, the hollow Ge NP is still completely amorphous, which further confirms that the temperature is well below the crystallization temperature. As the temperature is increased further to 545 °C, the amorphous Ge NPs completely crystallized, as shown in Figure 4.8d. Clear lattice fringes and atomic columns can be observed in the image. At this temperature, the Ge atoms gain enough energy to diffuse and reorganize to a more thermally stable configuration and the pin hole of the hollow Ge NPs is closed to minimize the surface energy. This results in the conversion of the hollow structure into solid crystalline Ge NPs. As a comparison, Figure 4.9 shows an in situ observation of crystallization of a single amorphous hollow Ge nanoparticle under the 300 kV electron beam at 385 °C. Notice that the hollow shape is maintained through the first 3 min and the crystallized area increases as more high-energy electrons impinge on the NPs. At the same time, the image starts to lose contrast which might be attributed to the initiation of the Ge atom diffusion process under the electron beam.

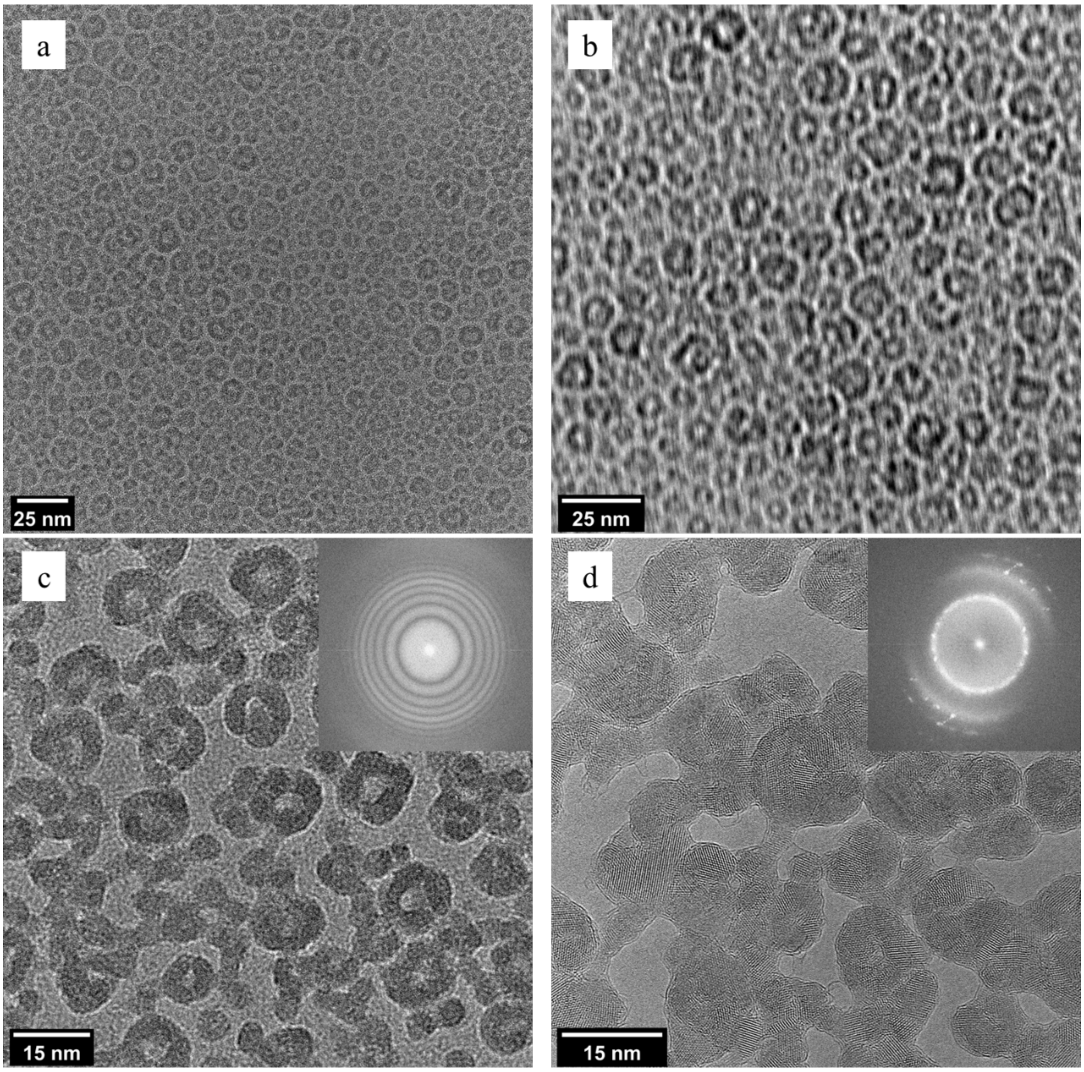

Figure 4.8. (a) BF-TEM image of the as synthesized hollow Ge NPs. (b) BF-TEM recorded during the in situ heating process, the image drifting due to the thermal expansion of the metallic TEM grid holder and thermal vibration, the resolution deteriorated significantly. (c) The amorphous hollow Ge NPs at 385 °C, the insertion is a FFT of the TEM image. (d) The hollow Ge NPs completely crystallized at 545 °C. The insertion is the corresponding FFT image.

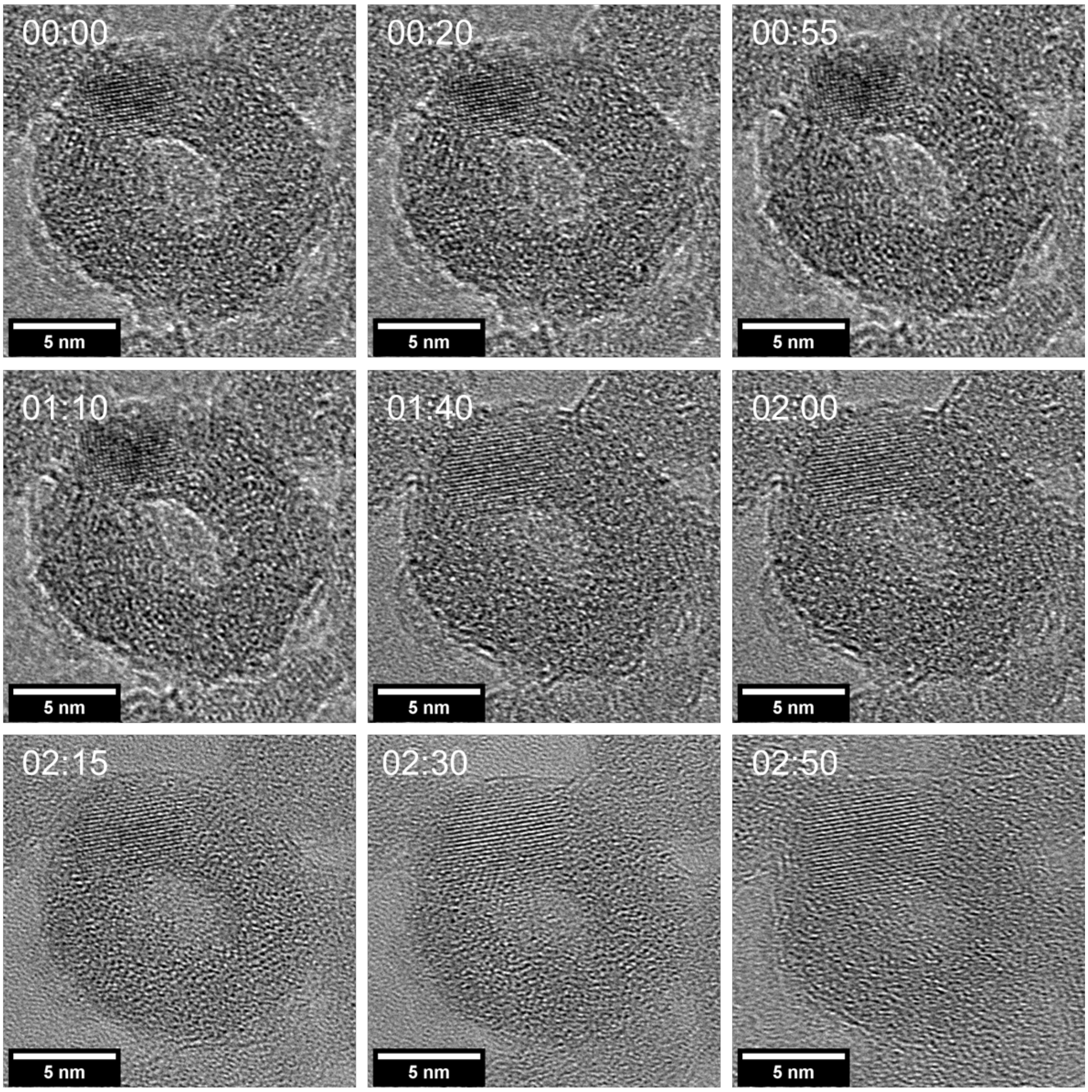

Figure 4.9. In situ observation of crystallization of amorphous hollow Ge NP at 385 °C.

4.3.5 In Situ Observation of the Structural Transformation of Ag@Ge Core−Shell Nanocrystals

To investigate the heat-induced metal-semiconductor redistribution in the anisotropic hetero-nanostructure with a high spatial resolution and chemical sensitivity, a heating experiment was performed inside the column of an aberration-corrected TEM using a MEMS-based in situ heating holder. The Ag@Ge core−shell nanocrystals were loaded on the heating chip serving as both the heat element and the sample support. It is found that the core−shell structure remains stable below 200 °C. No obvious changes are observed except that in the temperature range of 100−150 °C, carbon contamination builds up during the imaging process because of interaction between the surfactant and the electron beam. The carbon contamination becomes negligible when the temperature is beyond 200 °C, due to decomposition of the surfactant. With a heating rate of 5 °C/min, the temperature was increased to 385 °C, as indicated in the previous experiment. The reconstruction of NCs takes place during the observation under e-beam with a screen current at 6.24 nA and the dose rate at 1.38 E5 e/Å^{2}s. It is observed that the two different Ge domains gradually diffuse to the surface of the Ag core and merge and reconstruct on the surface, forming a uniform crystalline Ge layer that completely covers the Ag core with a sharp heterointerface between, as shown in Figure 4.10. It is also noted that, at the first 2 min, the Ge shell remains amorphous. However, during the next 2 min, the strong electron beam gives rise to the formation of crystalline Ge. In addition, both Ag and Ge remain compositionally pure during the reconstruction, and no signs of interdiffusion are detected.

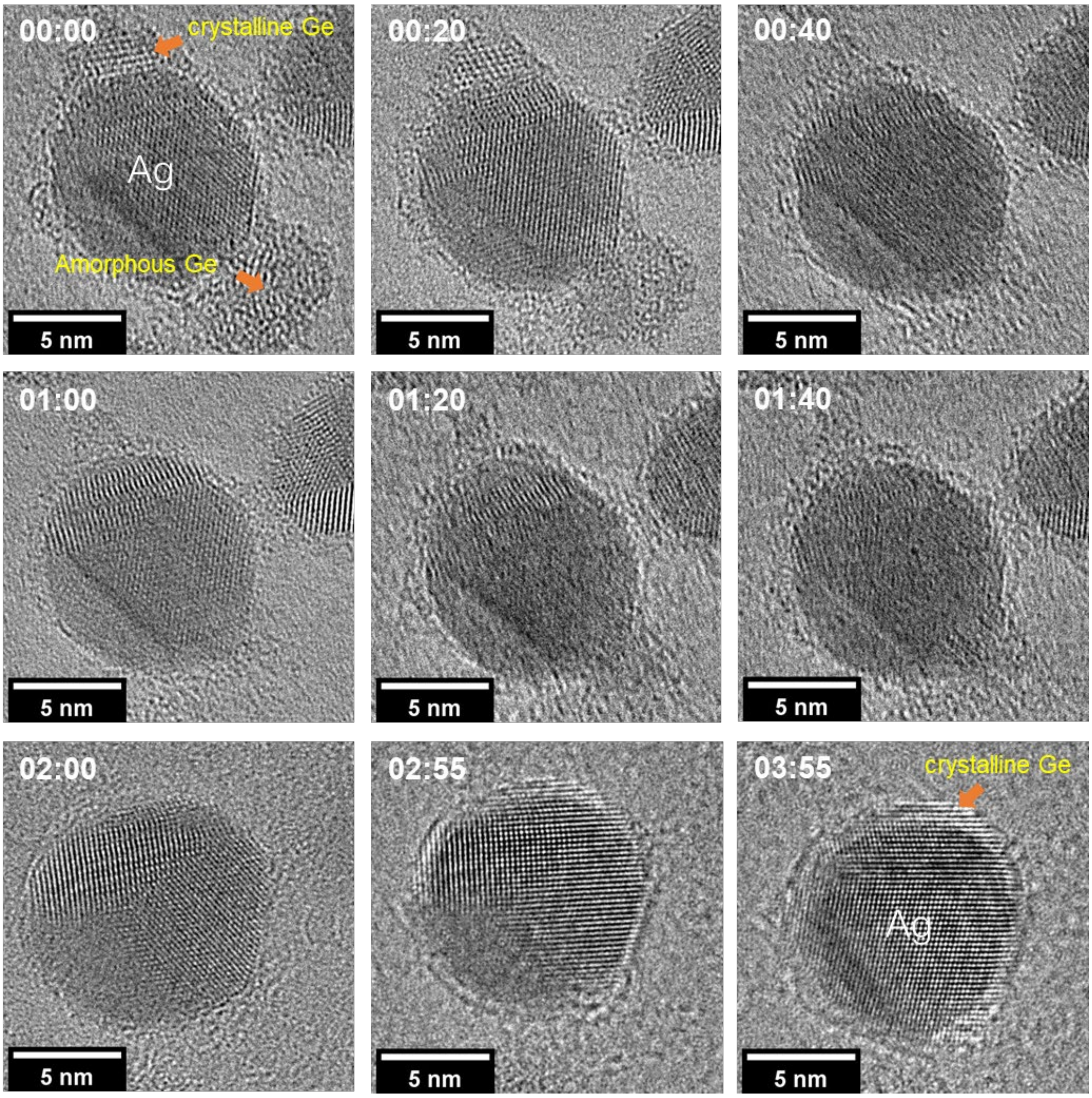

Figure 4.10. Time-series of in situ observation of transformation of Ag@Ge core-shell nanocrystals at 385 °C.

In contrast, when the temperature was further increased to 545 °C, phase segregation of the Ag and Ge was observed. As shown in Figure 4.11 the Ag@Ge core-shell nanoparticles are transformed into Janus Ag-Ge nanoparticles with two distinct phases. This transformation might be due to the high surface tension induced by the large lattice mismatch between the Ag and Ge phase. At 545 °C, the Ag atoms and Ge atoms gain enough energy to diffuse freely on the amorphous carbon support of the TEM grid. Therefore, the core-shell nanostructures are transformed into Janus particles to minimize the interface between the Ag and Ge domains and the overall surface tension is significantly reduced. Typically, core-shell NPs are synthesized based on the atomic size, relative strengths of homonuclear bonds, and surface energies of elements.[33] In most cases, the smaller atoms reside in the core while the larger atoms comprise the shell due to steric constraints. However, once exposed to high annealing temperatures, the surface energy dictates the diffusion of the element either from the core or shell.[34] Core-shell NPs from completely soluble solid systems such as Au-Pd[35] and Co-Pt[36] are well studied and show that homogeneous structures form after thermal annealing, while heterodimers or nanohybrid structures are to be expected in bimetallic systems with immiscible and lattice mismatched elements due to interfacial strain minimization during thermal induction.[37-40] Our study shows that metal-semiconductor core-shell nanostructures with even higher interfacial strain transform from a well-defined core-shell nanostructure into a heterodimer.

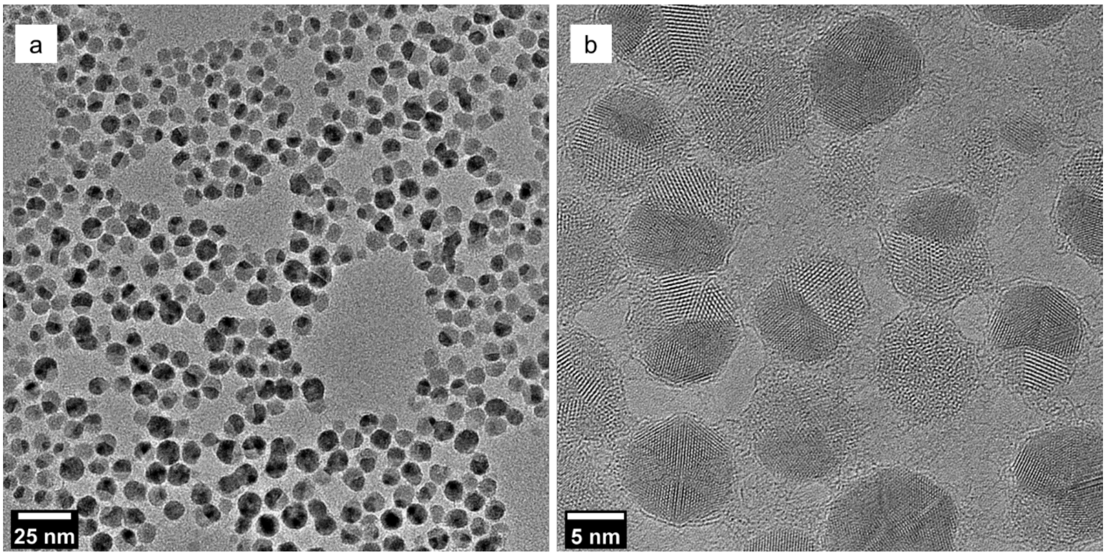

Figure 4.11. BF-TEM images of the Ag-Ge Janus nanoparticles at 545 °C at low (a) and high (b) resolution.

4.4 Conclusion

Overall, we have demonstrated structural and phase transformation of both amorphous Ge NPs and Ag@Ge NPs employing various microscopies. A direct observation is provided for the crystallization process of the amorphous Ge nanostructure at atomic resolution, and it clearly elucidates the phase transition condition and shape evolution of the amorphous Ge NPs under direct Joule heating. The thermal behavior of Ag@Ge core-shell nanostructures is also explored under the same heating and electron beam conditions. The amorphous Ge shell can be completely crystallized while maintaining the core-shell nanostructure at a moderate temperature. Further heating will enable the freely diffusive process of both Ag and Ge atoms leading to a transformation of the core-shell nanostructure into a phase segregated Ag-Ge Janus nanoparticle, with a clear interface between the Ag and Ge domains. The transformation process is summarized in Figure 4.12. The study provides a protocol as well as insight into the thermal stability and strain relief mechanism of complex nanostructures with high surface tension and lattice strains at single nanoparticle level with ultra-high resolution. The protocol can be easily adapted to study other nanostructures such as metal alloys, metal-semiconductor hetero-nanostructures and doped nanomaterials, and can provide valuable information for their further applications.

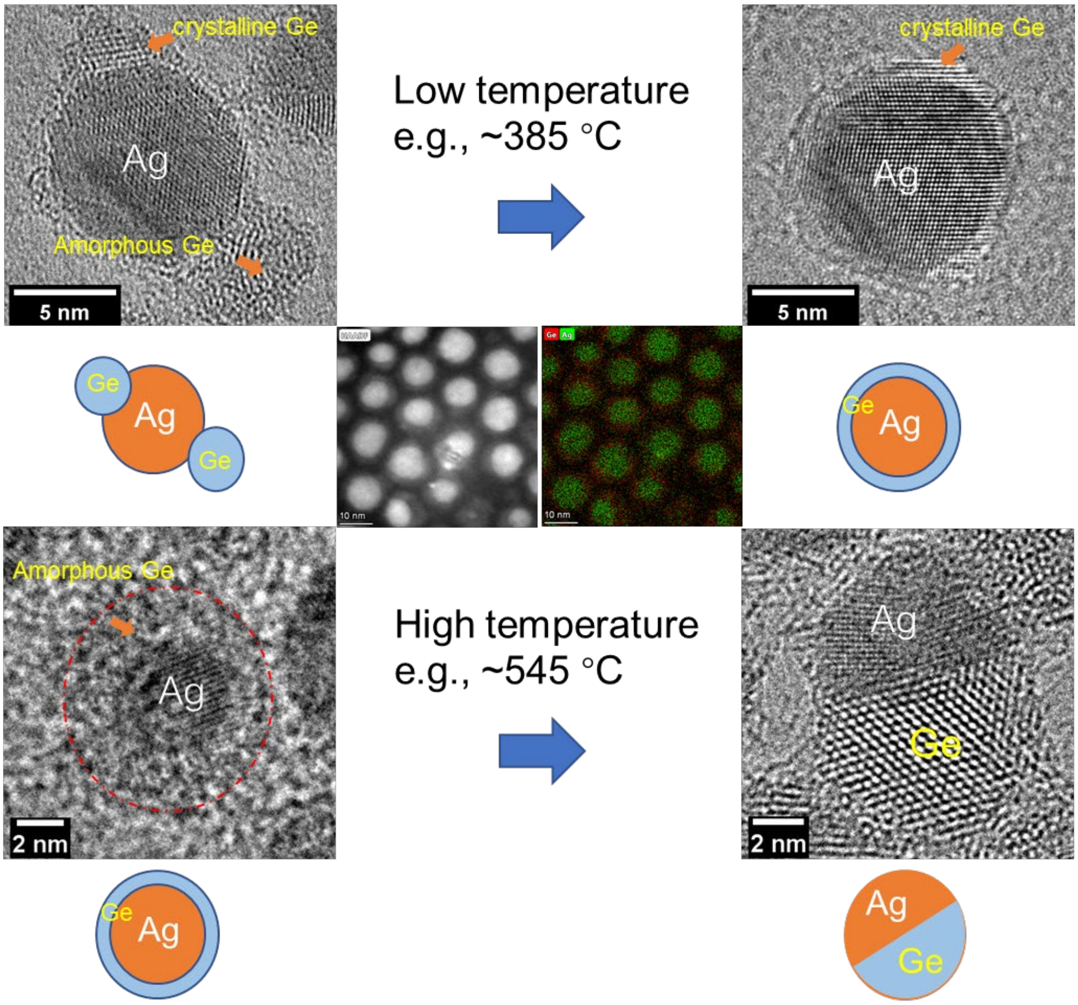

Figure 4.12. Scheme of the morphologic and crystallinity transformation of Ag@Ge core-shell NPs at different temperatures.

4.5 Materials and Methods

4.5.1 Chemicals and Materials.

Silver(I) nitrate, $AgNO_3$ (≥ 99.0%, Sigma-Aldrich), was used as received. Phase pure germanium (II) iodide, GeI_2, was purchased from Prof. Richard Blair's laboratory (University of South Florida). Oleylamine, OAm (> 40%, TCI America), dioctyl ether, DOE (99%, Sigma-Aldrich), dodecanethiol DDT (98%, Sigma-Aldrich) were degassed at 100 °C under argon flow for 1h prior to use. Tri-n-octylphosphine, TOP (min. 97%, Strem Chemicals), was used as received. Methanol and toluene were purchased from Fisher Scientific, purified using a solvent purification system, degassed, and stored under inert atmosphere conditions in an argon-filled glove box.

4.5.2 Synthesis of Silver Nanoparticles.

In an argon-filled glove box, 2 mmol of $AgNO_3$ (0.340 g) was added to 20 mL of OAm in a two-neck round-bottom flask equipped with a stopcock adapter and rubber septum. The flask was connected to a Schlenk line, and the suspension was then heated up to 60 °C. The temperature was maintained until the granular $AgNO_3$ crystals are completely dissolved. The solution was then quickly heated with a ramp $\geq$ 10 °C min^{-1} to 200 °C for 40 min while under an argon flow. The reaction was initially colorless, but as the $AgNO_3$ was reduced to form OAm stabilized Ag NPs, the reaction turned dark brown. Upon cooling to room temperature, the Ag NPs were isolated using a toluene/methanol system under argon protection. The mixture was centrifuged at 8500 rpm for 10 min. The supernatant was discarded, and the precipitates were re-dispersed in toluene for further characterization. To prepare the galvanic replacement reaction between Ag and GeI_2, the Ag NPs precipitates were directly pumped in the glovebox and re-dispersed in 20 mL of DOE for further use.

4.5.3 Synthesis of Ge NPs

In a typical synthesis of hollow Ge NPs, under inert atmosphere conditions, 0.15 mmol (0.049 g) GeI_2 was sonicated in 4.2 mmol TOP (1.931 mL) until it became a uniform yellowish solution. About 0.5 mmol Ag NPs dispersed in 20.78 mmol (6.234 mL) of DOE was transferred to a 35 mL microwave vessel followed by addition of the GeI_2/TOP solution and 5 mmol of DDT (1.2 mL). The microwave vessel was sealed with a silicone cap purchased from CEM, transferred to a CEM microwave reactor (Discover SP), and heated to 200 °C in dynamic mode. After heating 30 min at 200°C, the reaction was cooled to 60 °C in the reactor chamber by air cooling and then quenched in an ice-water bath. The microwave vessel was covered by parafilm and transferred into a glove box. The resulting product was washed with toluene/methanol and centrifuged at 8500 rpm for 10 min three times. The supernatant was discarded each time, and the Ge NPs were dispersed in toluene and stored in a glass vial within the glovebox. For the synthesis of solid Ge NPs, a GeI_2/Ag molar ratio of 0.3 is used instead.

4.5.4 Synthesis of Ag@Ge Core-shell NPs.

The same procedure as described for the synthesis of Ge NPs was followed except that the temperature is lowered to 150 °C and the reaction is quenched after 15 min followed by directly injecting into 20 mL of ice-cold methanol solution.

4.5.5 Characterization – In situ Heating Experiment

In situ TEM data were acquired using a FEI ThemIS 60−300 STEM/TEM (Thermo Fisher Scientific, US) operated at 300 kV at the National Center for Electron Microscopy within the Molecular Foundry in Lawrence Berkeley National Laboratory.

The synthesized nanoparticles were dispersed in toluene and one drop of the dispersion was cast on a copper TEM grid with amorphous carbon coating. After drying under vacuum oven overnight, the TEM grid was loaded onto a Gatan in situ heating holder and connected to a recirculating water system and a Gatan DP460 hot stage power supply, as shown in Figure 4.13. The ThemIS is equipped with image aberration corrector optics, and a scintillator-based camera (FEI Ceta2, 4k × 4k pixels, and 14-bit dynamic range). EDS mapping was performed using a Bruker Super-X Quad windowless detector with a solid angle of 0.7 sr.

Figure 4.13. Gatan in situ heating holder and connected to a recirculating water system and a Gatan DP460 hot stage power supply.

4.6 References

1. Baldassarre, L.; Sakat, E.; Frigerio, J.; Samarelli, A.; Gallacher, K.; Calandrini, E.; Isella, G.; Paul, D. J.; Ortolani, M.; Biagioni, P., Midinfrared Plasmon-Enhanced Spectroscopy with Germanium Antennas on Silicon Substrates. *Nano Letters* **2015,** *15* (11),

7225-7231.

2. Tang, L.; Kocabas, S. E.; Latif, S.; Okyay, A. K.; Ly-Gagnon, D.-S.; Saraswat, K. C.; Miller, D. A. B., Nanometre-scale germanium photodetector enhanced by a near-infrared dipole antenna. *Nature Photonics* **2008,** *2* (4), 226-229.

3. Assefa, S.; Xia, F.; Vlasov, Y. A., Reinventing germanium avalanche photodetector for nanophotonic on-chip optical interconnects. *Nature* **2010,** *464* (7285), 80-84.

4. Michel, J.; Liu, J.; Kimerling, L. C., High-performance Ge-on-Si photodetectors. *Nature Photonics* **2010,** *4* (8), 527-534.

5. Guter, W.; Schöne, J.; Philipps, S. P.; Steiner, M.; Siefer, G.; Wekkeli, A.; Welser, E.; Oliva, E.; Bett, A. W.; Dimroth, F., Current-matched triple-junction solar cell reaching 41.1% conversion efficiency under concentrated sunlight. *Applied Physics Letters* **2009,** *94* (22), 223504.

6. King, R. R.; Law, D. C.; Edmondson, K. M.; Fetzer, C. M.; Kinsey, G. S.; Yoon, H.; Sherif, R. A.; Karam, N. H., 40% efficient metamorphic GaInP⁄GaInAs⁄Ge multijunction solar cells. *Applied Physics Letters* **2007,** *90* (18), 183516.

7. Park, M.-H.; Cho, Y.; Kim, K.; Kim, J.; Liu, M.; Cho, J., Germanium Nanotubes Prepared by Using the Kirkendall Effect as Anodes for High-Rate Lithium Batteries. *Angewandte Chemie International Edition* **2011,** *50* (41), 9647-9650.

8. Li, W.; Li, M.; Yang, Z.; Xu, J.; Zhong, X.; Wang, J.; Zeng, L.; Liu, X.; Jiang, Y.; Wei, X.; Gu, L.; Yu, Y., Carbon-Coated Germanium Nanowires on Carbon Nanofibers as Self-Supported Electrodes for Flexible Lithium-Ion Batteries. *Small* **2015,** *11* (23), 2762-2767.

9. Wu, S.; Han, C.; Iocozzia, J.; Lu, M.; Ge, R.; Xu, R.; Lin, Z., Germanium-Based Nanomaterials for Rechargeable Batteries. *Angewandte Chemie International Edition* **2016,** *55* (28), 7898-7922.

10. Wu, Y.-T.; Huang, C.-W.; Chiu, C.-H.; Chang, C.-F.; Chen, J.-Y.; Lin, T.-Y.; Huang, Y.-T.; Lu, K.-C.; Yeh, P.-H.; Wu, W.-W., Nickel/Platinum Dual Silicide Axial Nanowire Heterostructures with Excellent Photosensor Applications. *Nano Letters* **2016,** *16* (2), 1086-1091.

11. Dellas, N. S.; Minassian, S.; Redwing, J. M.; Mohney, S. E., Formation of nickel germanide contacts to Ge nanowires. *Applied Physics Letters* **2010,** *97* (26), 263116.

12. Liu, B.; Wang, Y.; Dilts, S.; Mayer, T. S.; Mohney, S. E., Silicidation of Silicon Nanowires by Platinum. *Nano Letters* **2007,** *7* (3), 818-824.

13. Burchhart, T.; Lugstein, A.; Hyun, Y. J.; Hochleitner, G.; Bertagnolli, E., Atomic Scale Alignment of Copper-Germanide Contacts for Ge Nanowire Metal Oxide Field Effect Transistors. *Nano Letters* **2009,** *9* (11), 3739-3742.

14. Dayeh, S. A.; Mack, N. H.; Huang, J. Y.; Picraux, S. T., Advanced core/multishell germanium/silicon nanowire heterostructures: The Au-diffusion bottleneck. *Applied Physics Letters* **2011,** *99* (2), 023102.

15. Chou, Y.-C.; Wu, W.-W.; Cheng, S.-L.; Yoo, B.-Y.; Myung, N.; Chen, L. J.; Tu, K. N., In-situ TEM Observation of Repeating Events of Nucleation in Epitaxial Growth of Nano CoSi2 in Nanowires of Si. *Nano Letters* **2008,** *8* (8), 2194-2199.

16. Izumi †, T.; Taniguchi ‡, M.; Kumai §, S.; Sato, A., Ferromagnetic properties of cyclically deformed Fe3Ge and Ni3Ge. *Philosophical Magazine* **2004,** *84* (36), 3883-3895.

17. Jamet, M.; Barski, A.; Devillers, T.; Poydenot, V.; Dujardin, R.; Bayle-Guillemaud, P.; Rothman, J.; Bellet-Amalric, E.; Marty, A.; Cibert, J.; Mattana, R.; Tatarenko, S., High-Curie-temperature ferromagnetism in self-organized Ge1−xMnx nanocolumns. *Nature Materials* **2006,** *5* (8), 653-659.

18. Qi, X.; Kauzlarich, S. M., Ge Nanocages and Nanoparticles via Microwave-Assisted Galvanic Replacement for Energy Storage Applications. *ACS Applied Nano Materials* **2020,** *3* (6), 5509-5520.

19. Chiu, H. W.; Chervin, C. N.; Kauzlarich, S. M., Phase Changes in Ge Nanoparticles. *Chemistry of Materials* **2005,** *17* (19), 4858-4864.

20. Chiu, H. W.; Kauzlarich, S. M.; Sutter, E., Thermal Behavior and Film Formation from an Organogermanium Polymer/Nanoparticle Precursor. *Langmuir* **2006,** *22* (12), 5455-5458.

21. Lin, Y.-C.; Lu, K.-C.; Wu, W.-W.; Bai, J.; Chen, L. J.; Tu, K. N.; Huang, Y., Single Crystalline PtSi Nanowires, PtSi/Si/PtSi Nanowire Heterostructures, and Nanodevices. *Nano Letters* **2008,** *8* (3), 913-918.

22. Yaish, Y. E.; Katsman, A.; Cohen, G. M.; Beregovsky, M., Kinetics of nickel silicide growth in silicon nanowires: From linear to square root growth. *Journal of Applied Physics* **2011,** *109* (9), 094303.

23. Mongillo, M.; Spathis, P.; Katsaros, G.; Gentile, P.; Sanquer, M.; De Franceschi, S., Joule-Assisted Silicidation for Short-Channel Silicon Nanowire Devices. *ACS Nano* **2011,** *5* (9), 7117-7123.

24. Sun, Y.; Mayers, B.; Xia, Y., Metal Nanostructures with Hollow Interiors. *Advanced Materials* **2003,** *15* (7-8), 641-646.

25. Skrabalak, S. E.; Au, L.; Li, X.; Xia, Y., Facile synthesis of Ag nanocubes and Au nanocages. *Nature Protocols* **2007,** *2* (9), 2182-2190.

26. Seo, D.; Song, H., Asymmetric Hollow Nanorod Formation through a Partial Galvanic Replacement Reaction. *Journal of the American Chemical Society* **2009,** *131* (51), 18210-18211.

27. McEachran, M.; Keogh, D.; Pietrobon, B.; Cathcart, N.; Gourevich, I.; Coombs, N.; Kitaev, V., Ultrathin Gold Nanoframes through Surfactant-Free Templating of Faceted Pentagonal Silver Nanoparticles. *Journal of the American Chemical Society* **2011,** *133* (21), 8066-8069.

28. Hong, X.; Wang, D.; Cai, S.; Rong, H.; Li, Y., Single-Crystalline Octahedral Au–Ag Nanoframes. *Journal of the American Chemical Society* **2012,** *134* (44), 18165-18168.

29. Gao , C.; Lu , Z.; Liu , Y.; Zhang, Q.; Chi, M.; Cheng, Q.; Yin, Y., Highly Stable Silver Nanoplates for Surface Plasmon Resonance Biosensing. *Angewandte Chemie International Edition* **2012,** *51* (23), 5629-5633.

30. Yang, Y.; Liu, J.; Fu, Z.-W.; Qin, D., Galvanic Replacement-Free Deposition of Au on Ag for Core–Shell Nanocubes with Enhanced Chemical Stability and SERS Activity. *Journal of the American Chemical Society* **2014,** *136* (23), 8153-8156.

31. Shahjamali, M. M.; Bosman, M.; Cao, S.; Huang, X.; Saadat, S.; Martinsson, E.; Aili, D.; Tay, Y. Y.; Liedberg, B.; Loo, S. C. J.; Zhang, H.; Boey, F.; Xue, C., Gold Coating of Silver Nanoprisms. *Advanced Functional Materials* **2012,** *22* (4), 849-854.

32. Sanedrin, R. G.; Georganopoulou, D. G.; Park, S.; Mirkin, C. A., Seed-Mediated Growth of Bimetallic Prisms. *Advanced Materials* **2005,** *17* (8), 1027-1031.

33. Ferrando, R.; Jellinek, J.; Johnston, R. L., Nanoalloys: From Theory to Applications of Alloy Clusters and Nanoparticles. *Chemical Reviews* **2008,** *108* (3), 845-910.

34. Lu, P.; Chandross, M.; Boyle, T. J.; Clark, B. G.; Vianco, P., Equilibrium Cu-Ag nanoalloy structure formation revealed by in situ scanning transmission electron microscopy heating experiments. *APL Materials* **2014,** *2* (2), 022107.

35. Ding, Y.; Fan, F.; Tian, Z.; Wang, Z. L., Atomic Structure of Au−Pd Bimetallic Alloyed Nanoparticles. *Journal of the American Chemical Society* **2010,** *132* (35), 12480-12486.

36. Bigot, J.-Y.; Kesserwan, H.; Halté, V.; Ersen, O.; Moldovan, M. S.; Kim, T. H.; Jang, J.-t.; Cheon, J., Magnetic Properties of Annealed Core–Shell CoPt Nanoparticles. *Nano Letters* **2012,** *12* (3), 1189-1197.

37. Yalcin, A. O.; de Nijs, B.; Fan, Z.; Tichelaar, F. D.; Vanmaekelbergh, D.; van Blaaderen, A.; Vlugt, T. J. H.; van Huis, M. A.; Zandbergen, H. W., Core–shell reconfiguration through thermal annealing in FexO/CoFe2O4ordered 2D nanocrystal arrays. *Nanotechnology* **2014,** *25* (5), 055601.

38. Liu, W.; Sun, K.; Wang, R., In situ atom-resolved tracing of element diffusion in NiAu nanospindles. *Nanoscale* **2013,** *5* (11), 5067-5072.

39. Yang, J.; Ying, J. Y., Diffusion of Gold from the Inner Core to the Surface of Ag2S Nanocrystals. *Journal of the American Chemical Society* **2010,** *132* (7), 2114-2115.

40. Mokari, T.; Aharoni, A.; Popov, I.; Banin, U., Diffusion of Gold into InAs Nanocrystals. *Angewandte Chemie International Edition* **2006,** *45* (47), 8001-8005.

Chapter 5 Summary and Outlook

Over the last two decades, many methods were reported for the synthesis of nano-germanium with great success, however, there are still many scientific challenges that need to be addressed. For example, some of the synthesis evolve the use of special germanium precursors which are not commercially available and thus need to be synthesized separately, therefore inevitably associated with high-cost, low-reproducibility, and limiting its scale up for further applications. Plus, the harsh reaction condition (high temperature, high pressure, strong reducing agents) also makes the reaction hard to control, not only bringing concerns about safety, but also leads to a broader size distribution and ill-defined shapes.

This dissertation reported a two-step facile synthesis method via galvanic replacement reaction at mild reaction condition with excellent control on the size and morphology of nanoparticles. Prior to our reports, galvanic replacement reactions in nanoscale were mostly conducted in aqueous solution and only the interaction between the metal precursor and the sacrificial templates were considered. The effect of the ligands during the galvanic replacement is usually insignificant thus being ignored. The morphological and compositional control are mostly achieved through fine-tune the addition rate of metal precursor (e.g., by interval injection or a syringe pump), and the reaction mechanism is studied by a traditional titration-like technique, which is owing to the extremely fast reaction rate and the lack of effective methods to quench the reaction.

Our study, on the other hand, has overcome the disadvantages described above and provides complementary information to enrich the chemistry of galvanic replacement reactions at nanoscale. First, the influence of the molar ratio of metal templates and the Ge precursor on the final morphology was discovered and the transformation from Ag NPs to solid Ge NPs was realized. In addition, by precisely controlling the temperature and reaction time, it's possible to obtain Ag@Ge core-shell nanostructures as an intermediate which is thermodynamically unstable due to their small size, large surface area, and high lattice mismatch. Moreover, we successfully achieved fine control on the hollow germanium, including surface roughness and the complexity of nanocages, by just varying the ligands without changing the original Ag NPs template and Ge precursors. These subtle morphological differences in the hollow nanostructure may change their properties, which are manifested in the increase of the surface to volume ratio, and the stiffness of the nanocages. The synergistic effect of this multi-ligands on the morphology and space complexity of the Ge NPs provides new insights and protocols for the synthesis of other nanomaterials, which can be used in many applications such as catalysts and lithium-ion batteries.

Besides, our research demonstrated that the galvanic replacement reaction can be applied to a non-aqueous system. This greatly expands the selection of metal/semiconductor precursors, to include those that are water- and oxygen- sensitive. Plus, the non-aqueous solvent enables the use of a variety of organic ligands containing both long hydrocarbon chains and functional groups to participate in the reaction and selectively control the final products. Depending on the interaction of different functional groups (e.g., thiol, phosphine, and amine) with existing nanoparticles or precursors, the ion diffusive rate can be further controlled, and the reaction can be limited to occur on a specific facet of the existing nanoparticle templates, thereby promoting or inhibiting the occurrence of galvanic replacement. Under this premise, galvanic replacement does not have to be limited between a single source of nano-template and only one type of precursor but can be expanded to three or more template-precursor combinations. Through proper ligand selection and fine control over the reaction temperature and concentration, binary or multi-component nanomaterials can be synthesized, and the chemical composition and morphology can be precisely controlled at the same time.

Our research also reveals that this kind of reaction is not restricted by lattice parameter matching in principle. Part of the reason is that the product is reduced by the metal template through an extremely fast reaction rate thus leading to a completely amorphous phase on the second material. Another reason may be that the reaction is done through a direct contact between ions and metal template, in which free electrons of the metal template transferred to the second metal/semiconductor precursor. This unique reaction mechanism ensures that the reduced substance must first grow on the existing nano-template surface, thus avoiding the self-nucleation process from a supersaturated solution and growing into undesired byproducts, like in traditional colloidal synthesis. This self-regulated and self-terminated feature ensures the ability for scale-up thus greatly expanding their potential applications.

In addition, we provide an in situ method to observe the phase transition process of amorphous nano-germanium through a combination of both joule heating and high-energy electron beams at high resolution in real time. By using the same method, we also study the stability and chemical distribution behavior of Ag@Ge core-shell nanostructures under thermal treatment with or without electron beams. It’s well known that, when the amorphous Ge NPs is heated to its phase transition temperature, crystallization will occur. However, previous work is mostly done in a macro scale, including heating the Ge NPs powder to a specific temperature (e.g., close enough or even exceeding the phase transition temperature), and then using traditional methods such as XRD and other characterization methods to determine the crystallinity of the sample. While it can achieve the crystallization process, this macro-scale method is accompanied by some intrinsic problems. First, when the size of a substance is reduced to the nanoscale, its phase transition temperature will greatly decrease, which is related to its high surface energy and depends on its size and morphology. This makes a precise determination of phase transition temperature for specific nanostructures extremely challenging. Second, when performing such experiments, the sample is usually prepared in the state of powder which means they are closely packed together and there is no physical barrier between individual particles. When the sample is heated above the phase transition temperature, the excessive energy will cause the sample to melt and sintered or aggregate together, thereby permanently destroyed the nano-size domains and original morphology of the samples, which makes it impossible to observe the individual particle behavior in terms of morphology and size changes during the phase transition.

In contrast, our work uses the in situ heating TEM method to characterize the thermal behavior of these nanoparticles. The sample was prepared by drop casting Ge NPs dispersion in solution directly onto a carbon film supported by copper TEM grid. After drying under vacuum, the nanoparticles are permanently fixed on the carbon film, making it possible to observe the phase transition process of a single nanoparticle at high resolution. Moreover, because the Ge NPs are well separated from each other by their surface ligands and the packing density can be easily controlled by the concentration of NPs dispersion, mutual diffusion and dispersion between the adjacent nanoparticles can be easily prohibited. So that the all-solid-state interface diffusion process as well as the accompanying morphological changes can be better observed. This is of great significance for studying the thermal stability of nanomaterials with complex morphology and multiple interfaces. Moreover, our work is based on conventional TEM technique, and does not require complicated instruments. Through the cooperation of high-energy electron beam and Joule heating, we can study the thermal stability characteristics of multi-component nanomaterials and intuitively characterize the process of diffusion and fusion between interfaces on the nanoscale. It provides a simple and powerful research tool for nanomaterials including metal alloys, metal-non-metal hetero-nanostructures and doped nanomaterials.

Although our work has made some solid progress in the synthesis and characterization of Ge-related nanomaterials, there are still many interesting works worthy of in-depth exploration. For example, Ge is a potential anode material for next generation lithium-ion batteries with excellent performance, due to its high theoretical capacity and high lithium-ion diffusion rate. However, lithium-ion intercalation leads to severe volume expansion and pulverization of such anode materials during the charge/discharge cycling, resulting in battery performance degradation, short circuit, and even explosion, which severely restricts their commercial application. It has been demonstrated that nano-structuring can improve the performance of LIBs by enhancing the surface electrochemical reactivity and reducing the electron/ion diffusion length. On the other hand, porous nanostructures can also provide internal space to accommodate the volume expansion, thereby relieving mechanical strain and allow for a stable anode electrolyte interface (AEI) during charge-discharge cycling. Our hollow germanium structure synthesized by galvanic replacement reaction possessed both advantages over the bulk materials, therefore, studying the battery performance of such hollow Ge NPs and nanocages in detail not only can help us better understand the volume expansion and pulverization mechanism, but also provide evidence for its practical applications. In addition, the high cost of the reported galvanic replacement reaction above is associated with the use of Ag NPs, thus exploring other cheaper alternatives such as copper, as the sacrificial template will be worthwhile and further facilitate their practical applications.

In addition, we revealed the mechanism of the galvanic replacement reaction in non-aqueous solvents and characterized the thermal stability of the products by in situ heating TEM. The next step will be to explore the thermal behavior of other hetero-nanostructures such as alloys, doped nanomaterials, and study the mechanism of mutual transformation between the core-shell structure and Janus particles or alloys, which is of great significance for all-solid-state reactions and colloidal synthesis of nanomaterials.